

A new computational approach towards the simulation of concrete structures under impulsive loading

Pereira, Luis

DOI

[10.4233/uuid:53096fa6-80ef-43a8-9fe9-d123b15d9efe](https://doi.org/10.4233/uuid:53096fa6-80ef-43a8-9fe9-d123b15d9efe)

Publication date

2017

Document Version

Final published version

Citation (APA)

Pereira, L. (2017). *A new computational approach towards the simulation of concrete structures under impulsive loading*. [Dissertation (TU Delft), Delft University of Technology].
<https://doi.org/10.4233/uuid:53096fa6-80ef-43a8-9fe9-d123b15d9efe>

Important note

To cite this publication, please use the final published version (if applicable).
Please check the document version above.

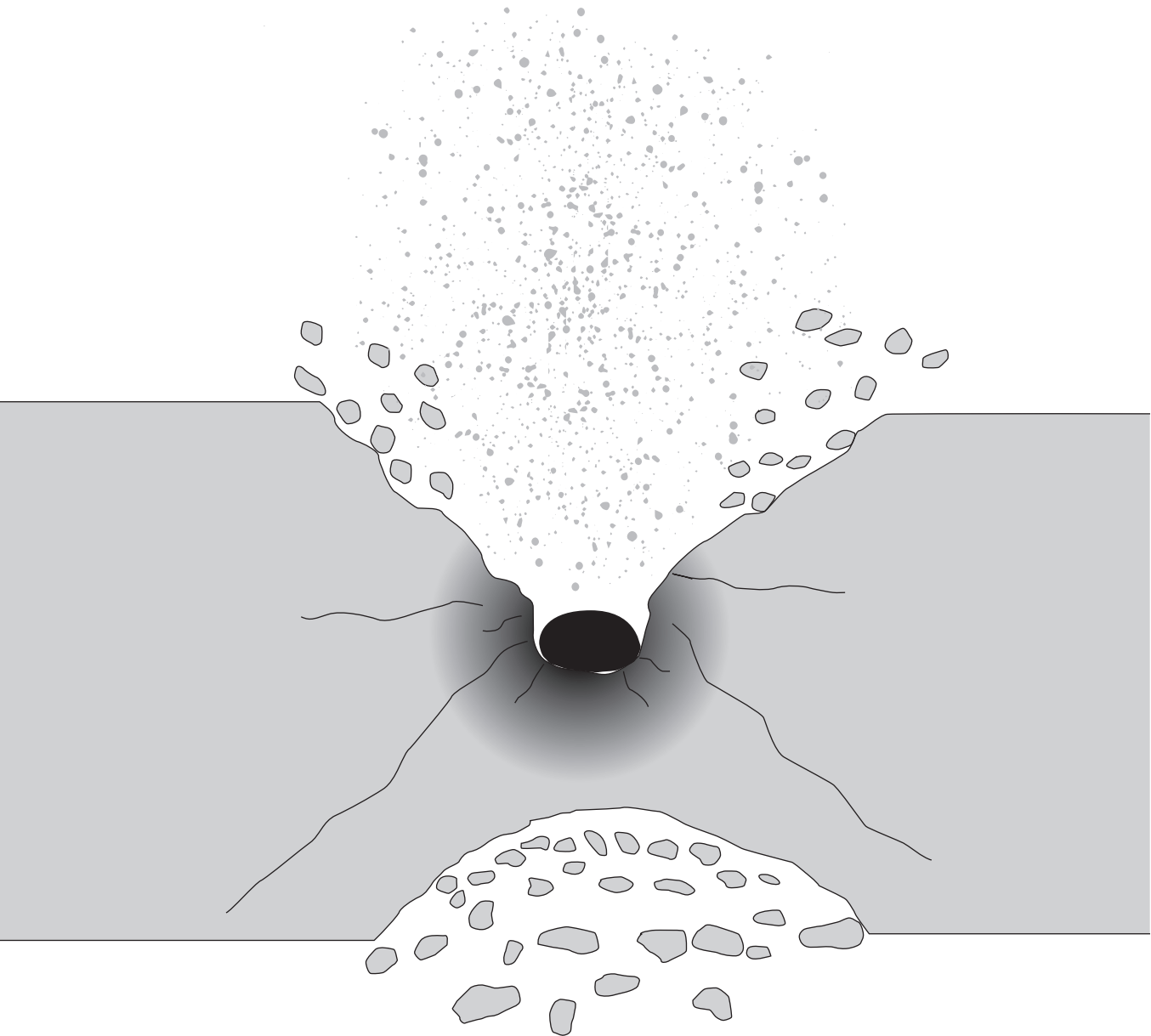
Copyright

Other than for strictly personal use, it is not permitted to download, forward or distribute the text or part of it, without the consent of the author(s) and/or copyright holder(s), unless the work is under an open content license such as Creative Commons.

Takedown policy

Please contact us and provide details if you believe this document breaches copyrights.
We will remove access to the work immediately and investigate your claim.

**A NEW COMPUTATIONAL APPROACH
TOWARDS
THE SIMULATION OF CONCRETE STRUCTURES
UNDER IMPULSIVE LOADING**



Luís Filipe Magalhães Pereira

**A NEW COMPUTATIONAL APPROACH TOWARDS
THE SIMULATION OF CONCRETE STRUCTURES
UNDER IMPULSIVE LOADING**

A NEW COMPUTATIONAL APPROACH TOWARDS THE SIMULATION OF CONCRETE STRUCTURES UNDER IMPULSIVE LOADING

Proefschrift

ter verkrijging van de graad van doctor
aan de Technische Universiteit Delft,
op gezag van de Rector Magnificus prof. ir. K.C.A.M. Luyben,
voorzitter van het College voor Promoties,
in het openbaar te verdedigen op dinsdag 1 december 2017 om 10:00 uur

door

Luís Filipe MAGALHÃES PEREIRA

Master of Science in Civil Engineering,
Portuguese Air Force Academy, Sintra, Portugal
geboren te Vigo, Spain.

Dit proefschrift is goedgekeurd door de

promotor: Prof. dr. ir. L.J. Sluys
copromotor: Dr. ir. J. Weerheijm

Samenstelling promotiecommissie:

Rector Magnificus,	voorzitter
Prof. dr. ir. L.J. Sluys,	Technische Universiteit Delft
Dr. ir. J. Weerheijm,	Technische Universiteit Delft & TNO Defence, Safety and Security

Onafhankelijke leden:

Prof. dr. J. Mazars,	Grenoble Institute of Technology – France
Prof. dr. N. Gebbeken,	University of the Federal Armed Forces – Germany
Prof. dr. ir. D. Hordijk,	Technische Universiteit Delft
Prof. dr. ir. M.A.N. Hendriks,	Norwegian University of Science and Technology – Norway & Technische Universiteit Delft
Dr. P. Grassl,	University of Glasgow – UK



This research was supported by the Portuguese Air Force Academy and the grant SFRH/BD/79451/2011 from the Portuguese *Fundação para a Ciência e Tecnologia* (FCT), Lisbon, Portugal, co-funded by the European Social Fund and by *Programa Operacional Potencial Humano* (POPH).

Keywords: Concrete, Ballistic impact, Hydrostatic damage, Stress-based nonlocal, Effective rate.

Copyright © 2017 by L. Pereira

ISBN 978-94-028-0848-3

An electronic version of this dissertation is available at
<http://repository.tudelft.nl/>.

*It doesn't matter how beautiful your theory is. It doesn't matter how smart you are.
If it doesn't agree with the experiments... It's wrong.*

Richard P. Feynman (1918 – 1988)

*It is a human habit to fix what is wrong.
We should rather focus on what is right...
And improve on it.*

Luís Pereira

CONTENTS

Summary	xi
Samenvatting	xiii
1 Introduction	1
1.1 Motivation	2
1.2 Research scope and aim.	3
1.3 Research methodology and thesis outline.	5
2 Study of dynamic tensile failure of concrete	
Rate-dependent stress-based nonlocal damage model	7
2.1 Introduction	8
2.2 Stress-based nonlocal formulation	10
2.2.1 Isotropic Damage Model (local formulation).	10
2.2.2 Standard nonlocal model	11
2.2.3 Stress-based nonlocal model.	12
2.3 Explicit computation scheme to determine \bar{Z}	13
2.4 One dimensional examples	16
2.4.1 Dynamic failure of a rod in tension (1D example)	16
2.4.2 1D spalling test.	19
2.5 Rate dependent model	21
2.5.1 Experimental validation	23
2.6 Conclusion	30
3 Study of dynamic tensile failure of concrete	
New <i>effective rate dependent</i> damage model	31
3.1 Stress-based nonlocal damage model.	34
3.1.1 Damage model.	34
3.1.2 Regularization model	35
3.2 Rate enhancement	36
3.2.1 Strain rate dependent formulation.	39
3.2.2 Definition of effective rate – R	39
3.2.3 Single element sensitivity study	40
3.3 One dimensional example – spalling	42
3.3.1 Numerical verification	44
3.3.2 Convergence study – determine Δt_{crit}	46
3.3.3 Effect of loading	48
3.4 ‘Experimental’ validation	49
3.4.1 Modified split Hopkinson bar test - notched specimen.	49
3.4.2 Modified split Hopkinson bar test – un-notched specimen.	53

3.5	Conclusions.	54
4	Study of dynamic crack propagation in concrete	
	Balance between tensile and compressive damage	57
4.1	Introduction	58
4.2	Constitutive law.	61
4.2.1	Damage model.	61
4.2.2	Rate enhancement – <i>Effective rate-dependent</i> formulation.	63
4.2.3	Regularization model – Stress based nonlocal	64
4.3	Single-edge notched tension test	65
4.3.1	Sensitivity analysis.	69
4.3.2	Results analysis – What makes cracks rotate and branch?	73
4.4	Compact tension test in concrete	75
4.4.1	Model description and calibration	75
4.4.2	Results and discussion	76
4.4.3	Effect of rate enhancement formulation	78
4.5	Conclusions.	80
4.6	Appendix	82
5	Simulation of ballistic impact on concrete targets	
	A new damage model for crushing and compaction	83
5.1	Introduction	84
5.2	Constitutive law.	87
5.2.1	Tension and compression-shear damage – Cracking	88
5.2.2	Hydrostatic damage (crushing) and compaction.	89
5.2.3	Effective hydrostatic damage (ω_h^*)	91
5.2.4	Rate enhancement.	92
5.2.5	Regularization model – Stress based nonlocal	93
5.3	Single element study - triaxial and hydrostatic tests.	94
5.4	High velocity impact	98
5.4.1	Model description and calibration	99
5.4.2	Mesh sensitivity	101
5.4.3	Evolution of damage	102
5.4.4	Effect of impact velocity and target thickness on fracturing process	103
5.4.5	Effect of ω_h on fracturing process representation	105
5.5	Conclusions.	107
6	Conclusions	109
6.1	Conclusions.	110
6.2	Suggestions for future research	112
	Acknowledgements	115
	Bibliography	117
	Curriculum Vitæ	131
	List of Publications	133

SUMMARY

Extraordinary actions such as blast loadings and high velocity impact are rare, but usually have devastating effects. Thus, making critical infrastructures, such as military and governmental facilities, power-plants, dams, bridges, hospitals, etc., more resilient against these hazards is one of the best ways to protect ourselves and our societies. Since concrete is a very common construction material, the development of realistic numerical tools to efficiently simulate its failure behavior under extreme dynamic loading conditions is of paramount importance, but still a major challenge.

This thesis presents a new stress-based nonlocal *effective rate-dependent* damage model, developed to simulate the dynamic response and failure of concrete during ballistic impact. The proposed isotropic damage formulation combines the effect of three damage modes: (i) tension (mode I), (ii) compressive-shear (mode II and mixed-mode) and (iii) hydrostatic damage to describe crushing of the cement matrix under pressure. The strain-rate dependent update of the constitutive relations to express the dynamic increase of strength and fracture energy in tension and compression is made a function of an *effective rate*, instead of the commonly used *instantaneous* strain rate. An enhanced version of the stress-based nonlocal regularization scheme is used to correct spurious mesh sensitivity. The proposed model was developed solely in the effective strain-space, following an entirely explicit computation scheme.

The development of the model can be divided in two major stages. In the first stage, the study focused on the problem of initiation, propagation and branching of cracks in dynamic mode I and mixed-mode loading conditions. It is demonstrated that common phenomenological models which consider the Dynamic Increase Factor (DIF) depending on an assumed constant strain-rate history are not adequate to describe the dynamic behavior of concrete. A *time* scale or viscosity must be added to the constitutive relations in order to describe inherent micro-dynamic properties of the material. Here, a *time* scale is introduced in the constitutive law through the *effective rate* concept, which restrains the ‘evolution of strain-rate’, to better represent the inherent dynamic properties of concrete. It is shown that this has a weak regularization effect and acts as a localization limiter. However, mesh objectivity is only attained with the addition of a *material length* scale. The enhanced nonlocal formulation used in this study considers a variable *material length* which expands and contracts as a function of the stress-state of neighboring elements. A contraction of the internal length is induced in the direction of the smaller principal stresses, which leads to a desirable localization of the damage profiles upon damage initiation. In addition to correcting spurious mesh sensitivity, it also provides a realistic representation of damage initiation and growth, in particular around discontinuities (notches and free boundaries) and damaged areas, overcoming a known limitation of standard nonlocal formulations.

In a second stage, hydrostatic damage is added to the formulation in order to take

the increasing damage of the material matrix observed during compaction into account. Besides controlling the evolution of the nonlinear volumetric response of the material, this new damage variable contributes to the deterioration of the material stiffness upon confinement. It is demonstrated that the description of the nonlinear volumetric response of concrete by an equation of state (EOS) as a plasticity phenomenon, as it is commonly done in hydrodynamic constitutive modeling, is unrealistic for concrete. Such formulations fail to represent the effect of the loss of cohesion observed during compaction on the deviatoric response of the material. By taking this phenomenon into consideration, the proposed model systematically predicts the relevant failure modes (cratering, tunneling, radial cracking and spalling) observed during ballistic impact on a concrete plate as a function of the projectile velocity and plate thickness.

The proposed phenomenological model is mesh objective and proved to be able to realistically simulate the behavior of concrete in different experiments, namely the modified split Hopkinson bar (spalling) tests, using both notched and un-notched specimens, the dynamic compact tension tests, the high pressure triaxial tests and ballistic impact tests. Based on the results presented in this thesis, it is suggested that a phenomenological model to simulate the dynamic failure of concrete should at least have the following properties: (i) a variable *material length* scale, (ii) a *time* scale and (iii) describe the loss of cohesion of the material under compression.

SAMENVATTING

Extreme belastingen zoals de blast ten gevolge van een explosie of het inslaan van brokstukken met een hoge snelheid, zijn zeldzaam maar kunnen als ze optreden een vernietigende uitwerking en grote gevolgen hebben. Door kritische infrastructuur, zoals energie centrales, militaire installaties, overheidsgebouwen, waterkeringen, bruggen, tunnels, ziekenhuizen etc, voldoende weerstand en incasseringsvermogen te geven om de gevolgen van deze extreme belastingen te beheersen, beschermen wij onszelf en onze samenleving. Omdat beton een van de meest gebruikte constructiematerialen is, is het ontwikkelen van betrouwbare en efficiënte, numerieke methoden om het bezwijkgedrag van beton onder extreem dynamische belastingen te kunnen simuleren van groot belang en tegelijkertijd een grote uitdaging.

In dit proefschrift wordt een nieuw “stress-based nonlocal *effective rate-dependent damage model*” beschreven voor de dynamische respons en het bezwijkgedrag van beton onder ballistische impact condities. De voorgestelde isotrope schade formulering combineert de effecten van drie schade mechanismen: (i) trek (Mode I), (ii) druk en afschuiving (Mode II en “Mixed Mode”) en (iii) hydrostatische druk (het verbrijzelen van de cement/mortel matrix). De reksnelheidsafhankelijkheid van de strekte en de breukenergie in de constitutieve relaties voor druk en trek is afhankelijk gemaakt van een *effectieve snelheid* in plaats van de *instantane snelheid*. Een verbeterde versie van de “stress based non-local” regularisatie methode is gebruikt om mesh onafhankelijkheid te realiseren. Het voorgestelde model is helemaal in de “effective strain space” ontwikkeld gebruikmakend van een expliciet rekschema.

In de modelontwikkeling kunnen twee fasen worden onderscheiden. De eerste fase van de studie richt zich op de initiatie, de propagatie en splitsen van scheuren onder “Mode I” en “mixed Mode” belastingcondities. De studie toont aan dat de gebruikelijke fenomenologische modellen, die uitgaan van de “Dynamic Increase Factor” (DIF) zoals bepaald voor een constante reksnelheid, niet geschikt zijn om de dynamische respons en schade ontwikkeling te beschrijven. Een *tijdschaal* of viscositeit moet opgenomen worden in de constitutieve relaties om de dynamische micro-mechanische respons op de lagere schalen weer te geven. In het huidige model is een *tijdschaal* geïntroduceerd door het “effective rate concept” waarmee de ontwikkeling van de in rekening te brengen reksnelheid wordt beheerst en het dynamisch gedrag van beton realistisch wordt gerepresenteerd. Het heeft ook een regulariserend effect, weliswaar beperkt, maar het beperkt lokalisatie in de numerieke oplossing. Echter, mesh-onafhankelijkheid is alleen gerealiseerd door het toevoegen van een *materiaal lengte schaal*. De “enhanced non-local” formulering zoals die in de huidige studie is toegepast maakt gebruik van een *variabele materiaal lengte schaal* die toe- of afneemt afhankelijk van de spanningstoestand in de omliggende integratiepunten. De lengte neemt af in de richting van de kleinste hoofdspanningen, waardoor de gewenste lokalisatie in de schadeprofielen optreedt nadat scheurvorming is geïnitieerd. Naast het realiseren van

de mesh-onafhankelijkheid wordt ook schade initiatie en propagatie, met name bij discontinuïteiten (zoals kerven en vrije randen) en schadezones, realistisch weergegeven. Hiermee is een beperking van de standaard “non-local models” ondervangen.

In de tweede fase van de studie is “hydrostatic damage” aan de schadeformulering toegevoegd om de toenemende schade in het matrixmateriaal onder compressie in rekening te brengen. Naast het beheersen van de niet-lineaire volumetrische materiaalrespons, heeft de nieuwe schadeparameter ook direct effect op de afname van materiaalstijfheid onder compressie. In de studie is aangetoond dat de beschrijving van de niet-lineaire volumetrische betonrespons doormiddel van een “equation of state” (EOS) gekoppeld aan plastisch gedrag, zoals dat in hydrodynamische constitutieve modellering wordt gedaan, voor beton niet realistisch is. Deze formuleringen zijn niet in staat om de gevolgen van het verlies aan samenhang in de matrix onder compressie op de deviatorische respons te beschrijven. Door dit fenomeen wel in rekening te brengen kan met het model de relevante bezwijkmechanismen (kratervorming, penetratie, radiale scheurvorming en spalling) zoals die optreden bij ballistische impact op betonnen platen beschreven worden afhankelijk van de projectielmassa en snelheid en plaatdikte.

Het ontwikkelde fenomenologische model is mesh-onafhankelijk en blijkt in staat te zijn om het dynamisch gedrag van beton zoals dat in diverse experimenten is waargenomen, realistisch te beschrijven. Voorbeelden hiervan zijn de “modified Split Hopkinson bar” testen (spalling testen) op proefstukken met en zonder kerven, de “dynamic compact tension test”, hoge druk triaxiale testen en ballistische impact testen. Op basis van de resultaten zoals beschreven in dit proefschrift wordt gesteld dat een fenomenologisch model voor het simuleren van het dynamisch faalgedrag van beton tenminste de volgende eigenschappen moet hebben: (i) een *variabele materiaal lengte* schaal, (ii) een *tijdschaal* en (iii) het verlies aan materiaalsamenhang onder compressie.

1

INTRODUCTION

1.1 MOTIVATION

Extraordinary actions such as blast loadings and high velocity impact are rare, but usually have devastating effects. Thus, making critical infrastructures, such as military and governmental facilities, power-plants, dams, bridges, hospitals, etc., more resilient against these hazards is one of the best ways to protect ourselves and our societies. It is of importance to evaluate how the existing structures would perform against such extreme loading scenarios and ensure that the new structures have the desirable level of protection and resilience [1]. Since concrete is a very common construction material, the development of realistic numerical tools to efficiently simulate its failure behavior under extreme dynamic loading conditions is of paramount importance, but still a major challenge.

Military and some defense agencies already have standards (eg. UFC 3-340-01 [2]) to ensure that strategic (infra)structures can sustain and/or contain the effect of explosions or impacts, in case of hostile attacks or accidental explosions due to faulty use and/or storage of explosives and ammunitions (see Krauthammer [3] for a review). These facilities usually consist of hardened structures located inside protected perimeters which guarantee a minimal disruption of normal operations in case of an attack. Although these measures are essential for the military, and other strategic agencies, who are responsible to guarantee our safety and essential services in abnormal time, it is not feasible to follow similar guidelines for structural design in urban environment. For obvious economical and architectural reasons, buildings in cities cannot be constructed like a fortress. Nevertheless, buildings and structures with political, social and economical relevance which should withstand the effects of blasts, ballistic impacts or close-in explosions, preferably without collapsing. Furthermore, it is important to reduce the amount of high velocity flying debris generated during these events due to failure of concrete elements, walls, windows, etc.. Since, these dynamic loads are beyond the scope of the design standards for buildings and other civil engineering structures (e.g. EC2 [4]), new structural design rules are needed to increase survivability and reduce casualties in case of a terrorist attack or accidental explosion.

Unlike other dynamic loads usually considered in structural design (earthquake and wind), close-in explosions and ballistic impacts are impulsive loads which hit the structures locally with pressures in the order of GPa's and durations of msec's. This usually leads to severe local damage of structural elements (columns, beams and slabs), before it can respond as a structure, and long before the entire structure being dynamically exited. Therefore, to determine the resistance of structures to explosions and impact, the local response/damage of individual or sets of structural elements must be analyzed before considering the dynamic response of the structure. These last analyses are usually done with the same type of models used to design structures against earthquakes and wind. But, the local analysis requires more sophisticated models that can represent the nonlinear response and failure of the different materials used in construction under impulsive dynamic loading conditions. Although there are many empirical and numerical models available to conduct such studies, new and more realistic models are needed in order to enhance the engineering design capabilities for safe structures.

Since concrete is probably the most commonly used construction material

worldwide, the development of realistic numerical tools to efficiently simulate its failure behavior under explosions or ballistic impacts is of paramount importance. But, despite the considerable resources dedicated to the study of the dynamic behavior of concrete, this is still an open challenge [5]. Very few of the models currently in use by engineers in finite element analysis are able to capture all failure mechanisms observed in concrete when subjected to such extreme dynamic loads [6]. This thesis presents a new phenomenological approach towards the numerical simulation of ballistic impact on concrete structures.

1.2 RESEARCH SCOPE AND AIM

During high velocity impact, intense pressure waves are induced, which expand radially in front of the impactor, leading to a complex process of interfering stress waves which exposes the material to rapidly changing multiaxial stress states and strain rate conditions. This leads to different failure mechanisms which, depending on the impactor properties (shape and material) and velocity, as well as the thickness of the target, may be as complex as represented in fig. 1.1. The mechanisms include: (1) compaction and crushing (hydrostatic damage) of the material in front of the impactor (strike face), associated with pore collapse and comminution (pulverization) of the material under pressure, leading to the formation of the Mescal zone [7]; (2) radial cracking in front and around the impactor (mixed mode failure), caused by hoop stresses raised in the wake of the initial pressure wave [8, 9]; (3) spalling (dynamic tensile fracture) at the rear face, upon reflection of the pressure wave; and (4) formation/expansion of the crater due to spalling at the impacted face [10].

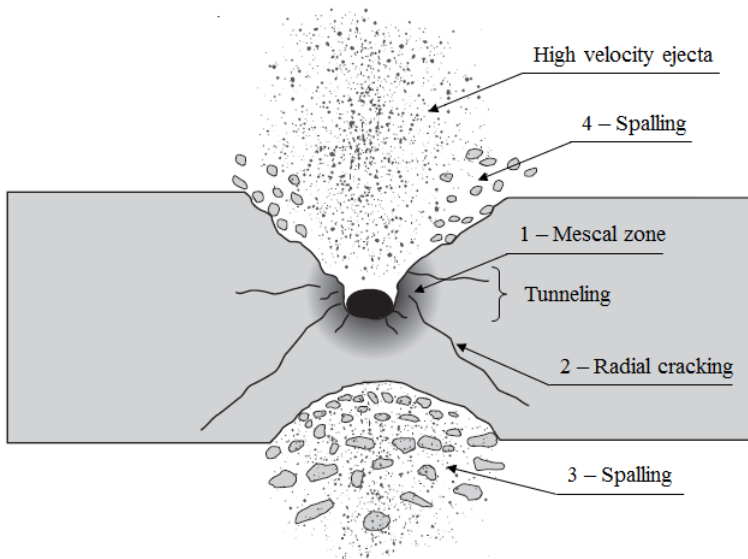


Figure 1.1: Failure mechanics observed in a normal ballistic impact on a slender concrete plate.

The flow of the pulverized material around the penetrator allows it to cut through the target (cratering and tunneling). Under certain conditions, at the end of the deceleration phase of the impactor, conical punching failure (Hertzian cone) may occur as an extension of radial cracking. In a later stage, structural oscillations at moderate strain rates become the leading loading condition, and the main cause for further material mechanical degradation [11], such as the formation of the radial cracks visible at the front and back surfaces of the target.

It has been experimentally observed that the ballistic resistance is directly proportional to the thickness of the concrete plate and inversely proportional to the impact velocity (see for example [12, 13]). The extension or even the manifestation of the different failure modes depends on both factors. For example, dynamic failure on a slender concrete plate hit normally can vary from a small crater for a relatively low impact velocity to complete perforation at high velocity. The example depicted in fig. 1.1 represents an intermediate impact velocity where both cratering and spalling occurs.

It has been shown [8, 14, 15] that the evolution of failure of quasi-brittle materials is basically governed by three interdependent damage mechanisms (see fig. 1.2): (a) tensile (mode I) fracture; (b) compressive-shear (mode II and mixed-mode) failure; and (c) hydrostatic damage (crushing) of the cement matrix under compression, due to pore collapse during compaction. Furthermore, concrete is known to exhibit a significant dynamic increase of strength, stiffness and fracture energy in both tension and compression [16], due to the presence of water in the pores of the hardened cement past (*Stefan effect*), viscoelastic properties of the bulk material and inertia effects. Although many models can successfully simulate one or more aspects of the dynamic failure of quasi-brittle materials (e.g. plasticity [17–23], damage [24–34], plastic-damage [8, 35–45] and fracture based approaches [6, 46, 47]), very few are able to capture all failure modes observed during ballistic impact. It is believed that the development of more realistic formulations has been hampered by a poor representation of the sub-scale physical mechanisms responsible for the well known rate and pressure dependency of concrete.

This thesis focuses on overcoming these limitations in the development of a new phenomenological model of concrete for engineering purposes. The aim is to build numerical tools capable of objectively predicting the relevant failure modes of concrete observed during ballistic impact, independently of the impact velocity and target thickness. These mechanisms are: cratering, spalling, perforation (tunneling) and dynamic cracking. The models should be able to:

- accurately simulate failure behavior of concrete structures under impact;
- simulate simultaneous and subsequent evolution of the relevant failure mechanisms;
- properly account for the rate-dependent properties of concrete;
- simulate failure with models that are robust and objective with respect to finite element discretization.

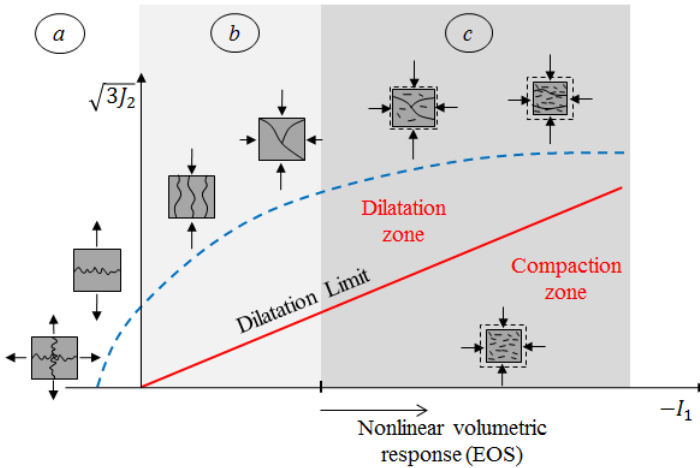


Figure 1.2: Schematic representation of the damage modes of concrete in the deviatoric space. The dashed line represents an experimental yield surface.

1.3 RESEARCH METHODOLOGY AND THESIS OUTLINE

This thesis presents a new stress-based nonlocal (SBNL) *effective rate-dependent* damage model for concrete, developed to simulate the different failure mechanisms observed during ballistic impact. In each chapter, the model is in a step-wise manner extended to describe a new damage mechanism associated with a different failure mode, as described in fig. 1.2. Each new feature/property of the model has been developed following the same four-step methodology:

1. Development of conceptual model based on experimental observations;
2. Formulation and implementation of constitutive model capable to describe the key phenomena/mechanisms hypothesized in the conceptual model;
3. Verify numerical robustness, stability and objectivity of the model using simple academic numerical examples;
4. Validate the model by simulating relevant experimental tests.

The proposed formulations have been developed entirely in a continuous damage mechanics framework and implemented as a *user defined material* (UMAT) in LS-DYNA [48] following explicit computation schemes.

The foundation for the proposed phenomenological model is set in chapters 2 and 3 with a study to dynamic tensile failure (spalling) of concrete (damage mode (a) in fig. 1.2). In chapter 2, the rate-dependent version of the well-known Mazars' damage model [24] is introduced. To overcome spurious mesh sensitivity, which is typical for this class of models, the recently proposed stress-based nonlocal [30, 49] model is used. The formulation is updated in order to be combined with a rate-dependent damage model. This regularization model uses a variable interaction domain defined as a

function of the stress-state of neighboring elements. A contraction of the interaction domain is induced in the direction of the smaller principal stresses, resulting in a more realistic localization behavior observed in a direction perpendicular to developing crack, free boundaries and/or other discontinuities. Since LS-DYNA does not provide a framework to implement a nonlocal model, an explicit computation scheme [50, 51] has been implemented, outside the UMAT, to determine the nonlocal quantity.

Chapter 3 presents a new rate-dependent damage model for concrete under dynamic tensile loading conditions. A simplified version of the newest Mazars' damage model [52] is used instead of the original one [24]. In the proposed formulation, the dynamic strength and fracture energy increase of concrete is described by an enhanced strain-rate formulation. An *effective rate* is considered to update the constitutive law, instead of the commonly used *instantaneous* strain-rate. This new concept adds a *time* scale to the constitutive relations which restrains the 'evolution of strain-rate', to represent the inherent micro-dynamic properties of concrete associated with dynamic retardation of cracking due to micro-inertia effects and viscous properties of the material.

Chapter 4 presents an extension of the damage model presented in chapter 3 to investigate the dynamic propagation of cracks and crack branching in quasi-brittle materials (damage mode (b) in fig. 1.2). A compressive damage variable is added to the formulation in order to have a realistic description of the unconfined behavior of concrete in mode I, mode II and mixed mode loading states. The stress-based nonlocal formulation presented in chapter 2 is also updated in order to correctly describe the evolution of the interaction domain in both tension and compression stress states. Based on the results presented in this chapter, it is discussed how the addition of a *time* scale and a variable *material length* scale contributes to a more realistic characterization of the dynamic crack propagation and branching in concrete.

In chapter 5, the development of the model is finalized. A new hydrostatic damage variable is added to the formulation in order to account for the destruction of the cement matrix observed during high-rate compaction (damage mode (c) in fig. 1.2). Besides controlling the evolution of the nonlinear volumetric response of the material, hydrostatic damage contributes to the deterioration of the material stiffness when confinement reduces. With the help of single element analyses of triaxial tests conducted by Gabet et al. [53], the need for an explicit description of the loss of cohesion under compression for a realistic description of the nonlinear volumetric behavior of concrete is discussed. Finally, a set of ballistic impact experiments [13] is simulated for validation of the proposed model.

Chapter 6 presents the main conclusions of this work and recommendations for future research.

2

STUDY OF DYNAMIC TENSILE FAILURE OF CONCRETE RATE-DEPENDENT STRESS-BASED NONLOCAL DAMAGE MODEL

In this chapter, the recently proposed stress-based nonlocal regularization scheme is enhanced and combined with a rate-dependent version of the well-known Mazars' damage model to study the dynamic tensile failure (spalling) of quasi-brittle materials. This regularization model uses a variable interaction domain defined as a function of the stress-state of neighboring elements. A contraction of the internal length is induced in the direction of the smaller principal stresses, resulting in a more realistic localization effect observed in a direction perpendicular to developing 'crack', free boundaries and other discontinuities. The proposed formulation was implemented in LS-DYNA using a fully explicit computational scheme.

Two sets of numerical examples are presented. First, one-dimensional analyses are used to evaluate the model capabilities, applicability and limitations. Second, the model is validated against experimental results. The proposed model, in addition to correcting spurious mesh sensitivity, also provides a realistic representation of damage initiation and growth, in particular around discontinuities (notches and free boundaries) and damaged areas, overcoming a known limitation of standard nonlocal formulations.

This chapter is based on L. Pereira, J. Weerheijm, and L. Sluys. A new rate-dependent stress-based nonlocal damage model to simulate dynamic tensile failure of quasi-brittle materials. *Int. J. Impact Eng.*, 94:83–95, 2016.

2.1 INTRODUCTION

The development of realistic numerical tools to efficiently model the response of concrete structures subjected to close-in detonations and high velocity impact has been one of the major quests in defense research. Even with today's state of the art finite element tools, it is still a great challenge to properly and efficiently simulate the response of a complex concrete structure under extreme dynamic loadings. For example, when a concrete structure is subjected to a contact detonation or high velocity impact, a shock wave is locally generated and expands radially through the structural element. The consequence is a complex process of interfering stress waves where the material is exposed to rapidly changing multiaxial stress states and strain rates conditions which lead to very different failure (damage) mechanisms: (i) compaction and crushing (hydrostatic damage), (ii) tensile failure (spalling) with an apparent dynamic increase of strength and (iii) mixed mode failure associated with anisotropic behavior [8]. In a later stage, (iv) structural oscillations at moderate strain rates become the leading loading condition, thus the main cause for further material mechanical degradation [11].

Dynamic tensile failure (e.g. spalling), characterized by a significant strength increase associated with loading rate, has revealed to be particularly challenging to represent. Failure in concrete develops from growth and coalescence of micro-cracks followed by formation of a fracture process zone, where the stresses are transferred by aggregate interlock and crack bridges. This process eventually culminates in a visible traction-free macro-crack. Concrete behavior is often described by nonlinear phenomenological models using a strain softening law in order to describe progressive cracking and stiffness reduction, and a regularization technique to correct spurious mesh sensitivity. Commonly, these constitutive laws are modeled in the framework of continuum damage mechanics [24, 26, 54], plasticity [29, 55, 56] or a combination of both [37, 41, 57]. There are also formulations promoted under different fracture-based approaches such as *microplane* models [46], lattice models [58] and discontinuous models [59, 60] (fracture mechanics, XFEM, GFEM, etc.).

Continuum damage mechanics models with a nonlocal formulation of integral or gradient type are among the most successful to represent concrete behavior, especially when used under monotonic tensile loading situations. The key idea behind nonlocal regularization methods is that the stress response at a material point depends on the state of its neighborhood. An internal length is introduced into the constitutive relation in order to describe micro-structural interactions. In the continuum damage mechanics context, regularization is obtained by the direct coupling of damage to a nonlocal variable, derived from a weighted average over a certain volume in the vicinity of the considered integration point of its local counterparts. Although successful in mitigating the spurious localization and pathological mesh sensitivity [61], this regularization technique is prone to some erroneous results and may lead to unrealistic damage initiation and evolution [62]. These misrepresentations are usually visible in the vicinity of free boundaries and discontinuities. This is the consequence of an inadequate treatment of interaction in these particular situations. There is now general consensus that the interaction domain should expand and contract as a function of the stress state, damage evolution and geometry of the problem. In the last decade several

nonlocal damage models with evolving length scale have been proposed to mitigate some of these deficiencies [49,63–70].

For models based on an integral regularization schemes, Krayani et al. [64] have proposed a model to improve the representation of damage in the vicinity of free boundaries. One of the limitations of this model is the need of a specific preprocessing technique where the effect of free boundaries on nonlocality are explicitly introduced in the model. Furthermore, the model does not take into consideration the effect of damage in the nonlocal interaction domain. To overcome this, Pijaudier-Cabot and Dufour [65] and Desmorat and Gatuíngt [66] proposed models where the interaction domain is indirectly made a function of local damage. Both models were developed following the *path attenuation in the nonlocal transfer of information* concept. Although very promising results have been presented for 1D examples, the extension of these models to 2D and 3D calculations is a difficult open challenge [69].

Finally, Giry et al. [49] proposed a model where the interaction domain (internal length) varies as a function of the stress state in the neighboring elements. A contraction of the weight function in the direction of the smaller principal stress-states is induced by this technique. Consequently, the interactions between elements decrease close to free boundaries, geometrical discontinuities (cracks) and damaged areas in their normal directions. The result is a desirable localization effect observed in these situations. In this chapter the stress-based nonlocal criterion [30, 49] has been updated in order to be consistently combined with a rate-dependent version of Mazars damage model [24]. This makes it possible to study dynamic tensile failure of quasi-brittle materials.

As it is well known, quasi-brittle materials exhibit a significant strength increase associated with high rate straining, in particular under tension [16]. The representation of dynamic tensile failure has motivated many experimental and numerical researchers. The retardation of internal microcracking observed at high deformation rates has been pointed out by several researchers as the leading cause of the observed strength increase, in particular in tensile stress conditions [11]. In the continuum damage mechanics framework one may say that the evolution of damage has a strong connection with the rate sensitivity of the material. Notwithstanding, the rate sensitivity of concrete and other geomaterials is still not completely understood. In particular, the rate effects in the post-peak regime are still very difficult to properly analyse and characterize. Thus, a simple strain-rate dependent criterion is proposed where only the damage threshold (peak stress) in the Mazars model is affected by rate. The corresponding modifications were made to the stress-based nonlocal formulation.

The model has been implemented within the framework of LS-DYNA [48] using a fully explicit computational scheme recently developed by de Sá et al. [50, 51]. This algorithm is used to determine the nonlocal quantity. It has been developed under the premise that the variation of the ratio between the local and nonlocal variables is infinitesimal in consecutive time steps. Accordingly, the current nonlocal quantity is simply determined by multiplying its local counterpart by a correction factor computed from weight averaging the results obtained in the previous time step.

After a complete description of the model and explicit algorithm (sec. 2 and 3), two sets of numerical studies are presented in this chapter. First (sec. 4), one-dimensional

examples are used to explore the limitations and applicability of the stress-based nonlocal formulation and the explicit computational scheme considering a rate-independent damage model. Second (sec. 5), the rate-dependent version of the stress-based model is validated against experimental results. Two experiments conducted at Delft University of Technology using a split Hopkinson bar are simulated [71].

2

2.2 STRESS-BASED NONLOCAL FORMULATION

2.2.1 ISOTROPIC DAMAGE MODEL (LOCAL FORMULATION)

Continuum damage mechanics has been widely and successfully used to describe quasi-brittle materials (concrete). The *damage* quantity is the macroscopic representation of the material stiffness degradation associated with micro-cracking (and other microscopic phenomena) that lead to fracture and rupture. Damage is driven by the density and orientation of micro-defects thus, in order to take the anisotropic nature of material failure into account, it should be represented by a vector or tensorial variable. However, simple isotropic damage models are generally sufficient to describe the behavior of concrete especially under monotonic uniaxial loading. For the present study, an adapted version of the damage model developed by Mazars [14] has been updated with different nonlocal formulations. Since this model is well described in literature, only a brief explanation is presented in order to introduce the nonlocal formulation discussed hereafter.

The Mazars model is an isotropic damage model that considers a single scalar variable ω to represent the material stiffness degradation. This damage parameter evolves from zero (virgin or undamaged material) to one (complete failure). Assuming that the Poisson ratio is not affected by damage, i.e. the relative reduction of all stiffness coefficients is the same and independent of the direction of loading. The stress tensor is expressed as:

$$\sigma = (1 - \omega)C : \varepsilon \quad (2.1)$$

where ε is the strain tensor and C the elastic stiffness tensor. During loading, the damage evolution is assumed to be a function of the internal variable κ that denotes the maximum equivalent strain (ε_{eq}) level reached in the material:

$$\kappa(t) = \max \varepsilon_{eq}(\tau) \quad \text{for all } t \geq \tau \quad (2.2)$$

$$\varepsilon_{eq} = \sqrt{\sum_{I=1}^3 \langle \varepsilon_I \rangle^2} \quad (2.3)$$

where $\langle \cdot \rangle$ are the Macaulay brackets, consequently $\langle \varepsilon_I \rangle$, with $I = 1, 2, 3$, are the positive parts of the principal strains. Damage initiates when the equivalent strain surpasses the damage threshold (κ_0) and its growth is described by the Kuhn-Tucker conditions:

$$f \leq 0 \quad \dot{\kappa} \geq 0 \quad \dot{\kappa} f = 0 \quad (2.4)$$

where $f(\varepsilon, \kappa) = \varepsilon_{eq} - \kappa$ is the loading function.

Mazars introduced two damage parameters, ω_t and ω_c , in order to describe the uniaxial behavior of concrete under tension and compression. For general stress states, ω results from the weighted combination of tensile and compressive damage according to

$$\omega = \alpha_t \omega_t + \alpha_c \omega_c \quad (2.5)$$

where the coefficients α_t and α_c take the stress state into account. In line with the most recent implementation of Mazars model (cf. Jirásek [72]), these coefficients are evaluated as

$$\alpha_t = \sum \frac{\varepsilon_{tI} \langle \varepsilon_I \rangle}{\varepsilon_{eq}^2} \quad \alpha_c = 1 - \sum \frac{\varepsilon_{tI} \langle \varepsilon_I \rangle}{\varepsilon_{eq}^2} \quad (2.6)$$

where ε_{tI} , with $I = 1, 2, 3$, are the principal strains due to positive effective stresses ($\bar{\sigma}$). In the present study, the damage functions or softening relations are described by the following exponential laws, for tension and compression respectively.

$$\omega_t(\kappa) = \begin{cases} 0 & \text{if } \kappa \leq \kappa_0 \\ 1 - \frac{\kappa_0}{\kappa} \exp\left(-\frac{\kappa - \kappa_0}{\kappa_f}\right) & \text{if } \kappa > \kappa_0 \end{cases} \quad (2.7)$$

$$\omega_c(\kappa) = \begin{cases} 0 & \text{if } \kappa \leq \kappa_0 \\ 1 - (1 - A_c) \frac{\kappa_0}{\kappa} - A_c \exp[-B_c(\kappa - \kappa_0)] & \text{if } \kappa > \kappa_0 \end{cases} \quad (2.8)$$

where κ_0 and κ_f are set as the equivalent strains (ε_{eq}) at the onset and end of tensile softening. The material parameters A_c and B_c are related to the shape of the uniaxial compressive stress-strain relation.

2.2.2 STANDARD NONLOCAL MODEL

As amply documented in literature, standard ‘local’ damage models are spuriously mesh sensitive. This pathology is usually mitigated with a nonlocal formulation, which introduces an *internal* or *intrinsic length* (l_r) in the constitutive relation, either by means of an integral-type [73] or a gradient-enhanced [74] formulation. In these models the stress response at a material (Gauss) point is made dependent on its neighbors.

In general, for the integral formulation, a nonlocal update of most continuum (damage) models is attained by replacing a certain variable ($Z = \varepsilon_{eq}, \kappa, \omega$, etc.) by its nonlocal counterpart:

$$\bar{Z}(x) = \int_V \beta(x, \xi) Z(\xi) dV(\xi) \quad (2.9)$$

Here, for each material point x , the nonlocal variable is evaluated as a weighted average of the local counterpart (Z) at all points ξ within the integration domain V . $\beta(x, \xi)$ is a weight averaging operator given by:

$$\beta(x, \xi) = \frac{\alpha(x, \xi)}{\Omega_r} \quad \text{with} \quad \Omega_r = \int_V \alpha(x, \zeta) dV(\zeta) \quad (2.10)$$

where Ω_r is the normalization operator commonly referred to as *interaction volume* and $\alpha(x, \xi)$ is an arbitrary weight function, here considered to be the Gaussian function:

$$\alpha(x, \xi) = \exp\left(-\frac{4\|x - \xi\|^2}{l_r^2}\right) \quad (2.11)$$

2.2.3 STRESS-BASED NONLOCAL MODEL

These nonlocal formulations are generally accepted as a proper approach to avoid spurious localization and pathological mesh sensitivity [61]. However, this regularization technique is prone to some erroneous results and may lead to unrealistic damage representation [62]. Damage initiation and growth are usually misrepresented in the vicinity of free boundaries and discontinuities [65]. This is the consequence of an inadequate treatment of the interaction between the different material points around these singularities. In this study, the stress-based nonlocal formulation developed by Giry et al. [49] is used. In this enhanced formulation the interaction domain is no longer fixed. It varies as a function of stress state of the surrounding elements.

In this approach, the nonlocality is no longer defined in terms of what a point x can receive, but rather on what a point located at ξ can distribute. The new influence domain around ξ is now defined by an ellipsoid which main axes are a function of its principal stress direction and magnitude. Consequently, by cross weighting the original interaction domain around x defined with a fixed l_r with the influence domains of all source points ξ , a final anisotropic interaction domain around x is created (fig. 2.1). A contraction of the weight function in the direction of the smaller principal stress-states is induced by this technique. Consequently, the interactions between elements decrease close to free boundaries, geometrical discontinuities (crack) in their normal directions and parallel to damaged areas. As a result, a more realistic representation of the stress-state is observed in these situations.

The influence domain of point ξ is defined by an ellipsoid whose principal axes have the same directions as the principal stresses and a magnitude of:

$$a_i = \rho_i l_r \quad \text{with} \quad \rho_i = \begin{cases} \left| \frac{\sigma_I}{f_t} \right| & \text{if } -f_t < \sigma_I < f_t \\ 1 & \text{if otherwise} \end{cases} \quad (2.12)$$

where ρ_i is the parameter that introduces the influence of the stress state in the nonlocal description. σ_I are the principal stresses and f_t is the material tensile strength. For numerical stability the influence domain axis a_i may vary between l_{min} and l_r [49]. One may notice that there is no distinction between the effects of a compressive or tensile stress-state in the regularization of the internal lengths. Since the focus of this study is to analyze predominantly tensile failure situations, this omission has no significant impact on the model response.

The influence of the source point ξ on the target point x is determined after the definition of the influential domains for all integration Gauss points. As it can be

interpreted from the scheme in fig. 2.1(a), the updated internal length $l_{x\xi}$ is defined as the ‘radius’ of the ellipsoid centered in ξ in the direction of the vector connecting the two points ($\underline{\xi} - \underline{x}$).

$$l_{x\xi} = \rho_{x\xi} l_r \quad \text{with} \quad \rho_{x\xi}^2 = \frac{1}{\frac{\sin^2 \varphi \cos^2 \theta}{\rho_1^2} + \frac{\sin^2 \varphi \sin^2 \theta}{\rho_2^2} + \frac{\cos^2 \varphi}{\rho_3^2}} \quad (2.13)$$

where the scaling factor $\rho_{x\xi}$ is defined in the conventional spherical coordinates system (fig. 2.1(b)). It is important to notice that the interaction between two points is no longer constant throughout the simulation as in the standard nonlocal model. Since the influential domain depends on the local stress-state, the lengths of the interaction weight function relating two points are not necessarily equal, i.e. $l_{x\xi} \neq l_{\xi x}$.

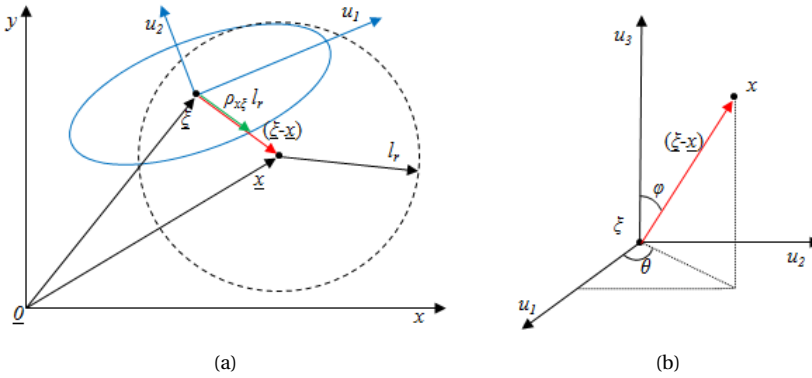


Figure 2.1: (a) Schematic representation, in a 2D projection, of the influence between the source point ξ and the target point x (black) and the original interaction domain of x (dashed). (b) Spherical coordinates system used to compute $\rho_{x\xi}$.

2.3 EXPLICIT COMPUTATION SCHEME TO DETERMINE \bar{Z}

In the current approach, an approximation algorithm is used to determine the nonlocal quantity \bar{Z} . This computation scheme has recently been developed, by de Sá et al. [50, 51], considering the assumption that the variation of the ratio between the local (Z) and nonlocal (\bar{Z}) variables is considered to be infinitesimal, in consecutive time steps [75]. Thus, the approximated nonlocal quantity of any local variable at any time step t_{n+1} is determined as:

$$\bar{Z}_{n+1} = K_{nl} Z_{n+1} \quad \text{with} \quad K_{nl} = \frac{\bar{Z}_n}{Z_n} \quad (2.14)$$

where K_{nl} is the *nonlocal penalty factor*. It is important to emphasize that this quantity is solely determined after the local and nonlocal results of the previous time step. Therefore, the extension to a nonlocal formulation of an existing damage model is done

by simply replacing the designated local variable by its nonlocal counterpart and the stress-state update procedure keeps its local format. This algorithm is particularly attractive because the resulting computation scheme remains fully explicit (see fig. 2.2).

The derivation of this computational scheme is now straightforward. The integral in equation 2.9 has the following discrete solution:

$$\bar{Z}_x = \sum_{\xi=1}^{NGP_x} \omega_{\xi} J_{\xi} \beta_{x\xi} Z_{\xi} \quad (2.15)$$

The nonlocal variable \bar{Z} at the Gauss point x results from the discrete combination of a weighted contribution of all local quantities that lie inside the interaction volume (Z_{ξ}). NGP_x represents the number of points belonging to that set. The quantities ω_{ξ} and J_{ξ} are the Gaussian weight and the Jacobian evaluated at point ξ , respectively. Finally, $\beta_{x\xi}$ is the weight of the nonlocal interaction between source (ξ) and target (x) points, determined by eq. 2.10, rewritten as:

$$\beta_{x\xi} = \frac{\alpha_{x\xi}}{\Omega_x} \quad \text{with} \quad \Omega_x = \sum_{\zeta=1}^{NGP_x} \omega_{\zeta} J_{\zeta} \alpha_{x\zeta} \quad (2.16)$$

where $\alpha_{x\xi}$, is the Gaussian function from eq. 2.11 and Ω_x represents the interaction domain of x . In the stress-based nonlocal model, this quantity is a variable, as well the weight interaction between elements ($\alpha_{x\xi}$), now determined after the updated influence length ($l_{x\xi}$).

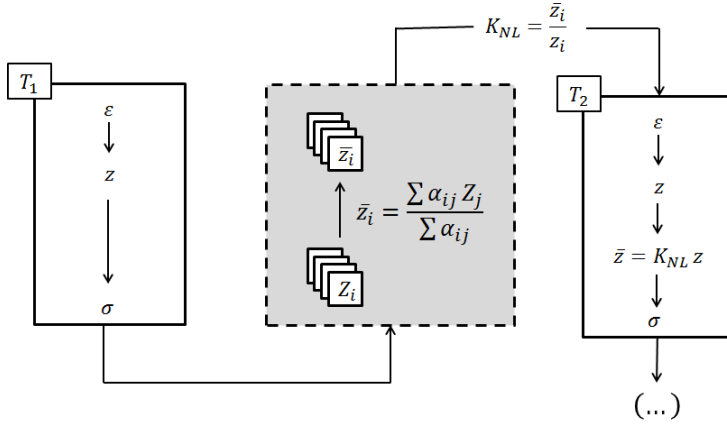


Figure 2.2: Schematic representation of the explicit computation algorithm used to determine the nonlocal variable.

Table 2.1 summarizes the computation sequence of nonlocal quantity $\bar{Z}_x^{(n+1)}$ when all local quantities, obtained in the previous time step, $Z^{(n)}$ are known. One may notice that the new interaction domain (Ω_i^{new}) is always a sub-domain of the original one (Ω_i) defined by l_r . Thus, for efficiency reasons and to keep the computation sequence explicit, the new nonlocal algorithm is called separately for every integration point x

and the nonlocal penalty factor K_{nl} (eq. 2.14) is determined just before entering the user defined material model subroutine.

It is important to mention that, if the usual assumption of considering nonlocal effects completely independent of the deformation history and the nonlocal internal length (l_r) is made (cf. Jirásek [76]), in a standard nonlocal formulation the averaging operators $\beta_{x\zeta}$ are constant throughout the simulation. Since these quantities are only related to the geometry of the problem, they only have to be evaluated once, saving precious computational resources. Considering the proposed scheme in tab. 2.1, this is the same as saying that the initial four steps are only performed at the beginning of the simulation, and only the last two steps have to be performed every time, making this a relatively efficient computational scheme for standard nonlocal models. The stress-based formulation presented herein does not take advantage of this. The only simplification used here is to consider the distance between points unchanged through the simulation, i.e. they are related to the undeformed geometry. Thus, the use of the model as implemented for this study is limited to problems undergoing small deformations.

Table 2.1: Computation sequence of the nonlocal procedure

Step	Output	Description
1.	Z_x with $j \in [1, \dots, NPG_i]$	Find the maximum source ξ for all target x elements
2.	$\Omega_x = \sum_{\zeta=1}^{NGP_x} a_{x\zeta}$	Define the influence domain of each point x
2.1	$a_i = \rho_i l_r$ with $\rho_i = \min(1, \frac{\sigma_i}{f_i})$	Define the interaction domains for all source points ξ_i
2.2	$l_{x\zeta} = \rho_{x\zeta} l_r$	Find influence length between x and all $\zeta = \xi_i$
2.3	$\alpha_{x\zeta}$	define the Gaussian function for the new $l_{x\zeta}$
2.4	$a_{x\zeta} = V_\zeta \alpha_{x\zeta}$	Determine interaction between points
3.	$\beta_{x\zeta} = \frac{a_{x\zeta}}{\Omega_x}$	Weight the nonlocal interactions between two points
4.	$\bar{Z}_x^{(n)} = \sum_{x=1}^{NGP_x} \beta_{x\zeta} Z_\zeta$	Determine nonlocal variable from previous results
5.	$K_{nl} = \frac{\bar{Z}_x^{(n)}}{Z_x^{(n)}}$	Determine nonlocal penalty factor
6.	$\bar{Z}_x^{(n+1)} = K_{nl} Z_x^{(n+1)}$	Correction of the local variable

One major restriction of this model is that very small time steps are needed in order to guarantee stable and convergent results. As it is discussed in the original work of de Sa et.al [50, 51], this condition is naturally met within explicit codes. However, as it will be demonstrated later, the accuracy of the model, under dynamic loading conditions, also depends on the nonlocal variable considered.

2

2.4 ONE DIMENSIONAL EXAMPLES

Numerical examples are used to illustrate features of the proposed model with adaptive nonlocal effects and to demonstrate the efficiency of the approximated explicit nonlocal formulation. First, a one-dimension pulling test is used in a sensitivity study to select the best variable to describe nonlocality. This example is also used to show the applicability and limitations of the explicit algorithm. Next, a spalling test is presented to study how damage initiation and growth is represented close to free boundaries. For both examples, a generic calibration of the Mazars damage model, for a concrete with $f_t = 3.0$ MPa, is considered (see tab. 2.2).

Table 2.2: Parameter set of the nonlocal rate-dependent damage model

Symbol	Parameter	Symbol	Parameter	Symbol	Parameter
E	30 GPa	ρ	2400 kg/m ³	ν	0.00
f_t	3 MPa	κ_0	f_t/E	κ_f	$5 \kappa_0$
A_c	1.34	B_c	$[(A_c - 1)/A_c]\kappa_0$	l_r	10 mm

2.4.1 DYNAMIC FAILURE OF A ROD IN TENSION (1D EXAMPLE)

A simple one-dimensional tension test was used to evaluate and compare the performance of different versions of the standard and stress-based nonlocal models. A clamped 100 mm long bar was axially loaded as described in fig. 2.3. The loading was designed to guarantee that after the reflection of the initial wave a continuous rectangular pressure pulse is attained, with double magnitude of the incident one. The bar is composed of a row of hexahedron elements (linear single integration point elements) with a 1 mm² cross section. Different mesh refinements (40, 100 and 200 elements) were considered to study the mesh sensitivity of the models. In order to preserve one-dimensionality the Poisson ratio has been set to zero ($\nu = 0$).

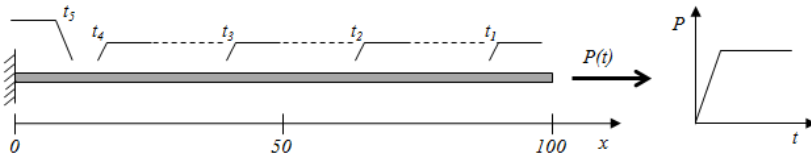


Figure 2.3: Schematic representation of a clamped bar in tension and respective loading.

SELECTION OF THE NONLOCAL VARIABLE (\bar{Z})

The equivalent strain (ε_{eq}) is the variable commonly used to describe nonlocality within the Mazars damage model. Nonetheless, according to Jirásek [77], any variable which is precursor of damage may be considered as nonlocal with only minor influence on the model performance. For the present case, this is the same as saying that considering either ε_{eq} or κ as nonlocal variables, i.e. Z in eq. 2.9. In figs. 2.4 to 2.6 the general performance of the stress-based nonlocal model considering these two variables as nonlocal are compared.

The stress-displacement relations considering different mesh refinements are presented in fig. 2.4. Convergent results for mesh refinements between 40 and 200 elements are observed. From these results, the use of ε_{eq} or κ as nonlocal variable seems not to make significant difference on the model performance. However, since an explicit algorithm is used, in addition to the mesh sensitivity study, the stability and convergence of the models must be evaluated for different incremental time steps (ΔT). It is common practice in explicit finite element algorithms to define ΔT as a fraction (T_{Fac}) of the critical time step (ΔT_{crit}) computed as the minimum time that the sound speed needs to cross any element in the mesh.

The final distribution of damage along the bar for different T_{Fac} is presented in fig. 2.5. In nonlocal formulations, these distributions are expected to be smooth across the fracture process zone. The presented results show that using κ as nonlocal variable leads to more stable results and convergence is observed even with the highest computation time increments ($T_{Fac} < 0.7$) (figs. 2.5(b)). In contrast, the use of ε_{eq} as nonlocal variable leads to less smooth damage profiles and convergence is only met with considerably smaller time steps ($T_{Fac} = 0.1$), as it can be seen in fig. 2.5(a).

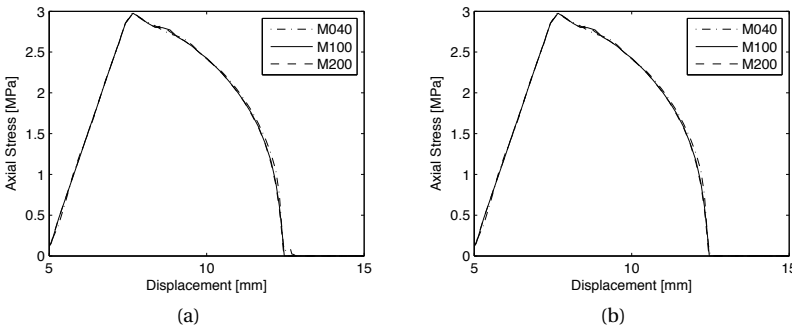


Figure 2.4: Stress-displacement relations for the stress-based nonlocal model for three meshes (40, 100 and 200 elements) and different nonlocal variables: (a) ε_{eq} and κ . ($T_{Fac} = 0.10$)

The difference between the two model performances is explained by the evolution (in time) of the respective local variables. The equivalent strain (ε_{eq}) is a variable dependent only on the current stress-state and in transient stress conditions between compression and tension it may fluctuate considerably. Consequently, even with very small time steps no smooth profile is guaranteed because the nonlocal quantity is the result of a weighted averaging of these quantities in a (nonlocal) domain that can

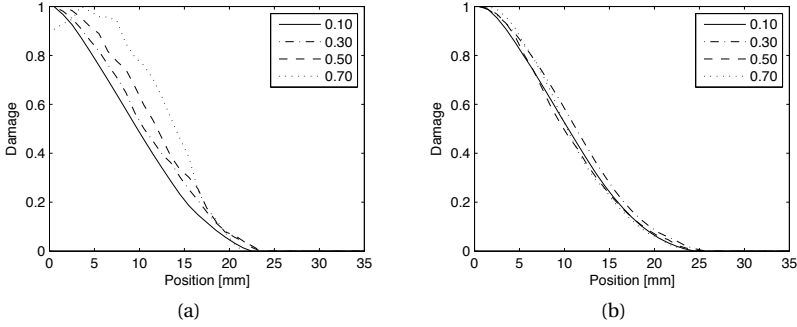


Figure 2.5: Final distribution of damage for the stress-based nonlocal (SNL) model with different T_{Fac} (Mesh of 100 elements). (a) ε_{eq} and (b) κ .

contain a large number of elements (see fig. 2.6(a)). On the other hand, κ is a monotonically growing variable dependent on the material loading history, which leads to a smoother evolution of its nonlocal counterpart even in transient situations and with relatively large time steps (see fig. 2.6(b)).

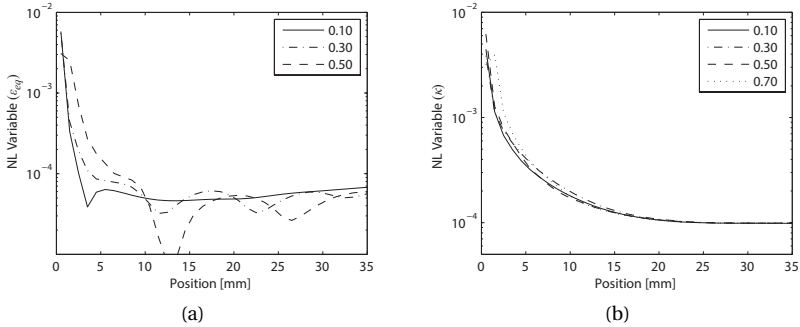


Figure 2.6: Final distribution of the nonlocal variable for the stress-based nonlocal (SNL) model with different T_{Fac} (Mesh of 100 elements). (a) ε_{eq} and (b) κ .

It is important to notice that, in the proposed algorithm, the current nonlocal quantities are not determined as a function of the actual stress-state (at time step T_n), but approximated by the stresses at the previous time step T_{n-1} . For that reason, a significant reduction of ΔT was expected to be necessary in order to ensure numerical stability. In LS-DYNA this is usually guaranteed with a $T_{Fac} = 0.9$ and $T_{Fac} = 0.67$ for *moderate* or *highly dynamic* simulations, respectively. Hence, making a conservative classification of the presented example, a reduction of only 25% of the default T_{Fac} must be considered if κ is used as nonlocal variable with a rate-independent damage model, i.e. stable results are obtained for $T_{Fac} = 0.7$ instead of $T_{Fac} = 0.9$.

COMPARISON BETWEEN STANDARD AND STRESS-BASED NONLOCAL MODELS

In the continuation of this chapter, the standard and stress-based nonlocal models are compared only considering $\bar{\kappa}$ as nonlocal variable. Fig. 2.7 shows the stress-displacement relations and evolution of damage of both nonlocal models considering the bar divided into 100 elements and $T_{Fac} = 0.3$. The long tailed softening behavior observed in the standard formulation results from a continuous expansion of the damage area even after maximum damage is attained ($\omega = 1$) disappears in the stress-based nonlocal formulation. Thus, the unrealistic continuous damage growth observed for standard nonlocal models is corrected in the presented enhanced version. In the stress-based model, when damage develops the stress decreases, leading to a contraction of the interaction domains around the damaged elements. The result is a more pronounced localization evidenced by the evolution of damage in fig. 2.7(b).

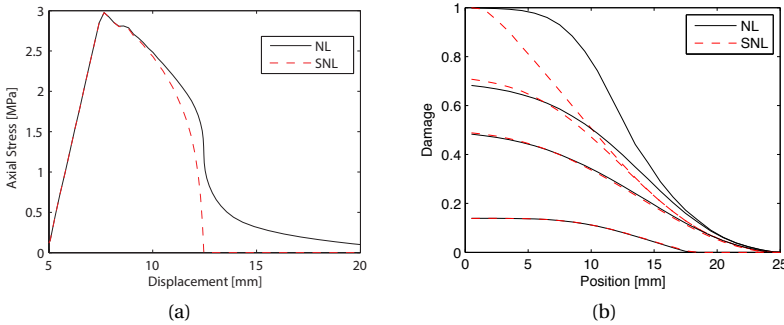


Figure 2.7: Comparison between standard (black lines) and stress-based nonlocal (red lines) models considering $Z = \kappa$: (a) stress-displacement relations and, (b) damage (ω) at times 40, 45, 55 and 80 μs .

2.4.2 1D SPALLING TEST

In order to continue the comparison between the two nonlocal formulations a one-dimensional simplification of a modified split Hopkinson bar experiment is modeled. With this example it is possible to study how these models represent damage initiation and evolution close to a free boundary.

As in the modified split Hopkinson bar experiment, a compressive wave, generated by a striker or an impulsive load produced by a blast, is applied at one side of the bar. The magnitude of the wave is chosen small enough such that linear elastic behavior of the material is guaranteed under compression, but high enough to ensure tensile failure upon reflection of the wave. When this elastic compression wave reaches the free edge of the bar, reflection occurs and the sign of the wave changes into tension. The two waves cancel each other up to the point when the tensile wave propagates a certain distance away from the boundary. For a block shaped pulse this distance equals to half of the initial signal length. Failure is initiated when the tensile strength is reached and spalling occurs. During failure, energy is dissipated in the fracture process

zone leading to damage increase and dispersion of the transmitted wave.

In the present study, a 100 mm long bar was axially loaded by a trapezoidal pressure pulse, as depicted in fig. 2.8. Again the material data set from tab. 2.2 is used. Two different loading conditions were considered with the only objective of changing the failure position d_{fail} . The same maximum pressure ($P = 7$ MPa) and loading rate ($\Delta P/\Delta t = 7$ MPa/ $2 \mu\text{s}$) were considered in both cases. The only difference is the total duration of the load (t_{load}). For $t_{load} = 20 \mu\text{s}$ and $t_{load} = 6 \mu\text{s}$, failure is expected to occur at a distance of the free edge (d_{fail}) of 31.5 mm and 7.6 mm, respectively. In the results shown in fig. 2.9 and 2.10 the theoretical failure positions are marked with a vertical black line.

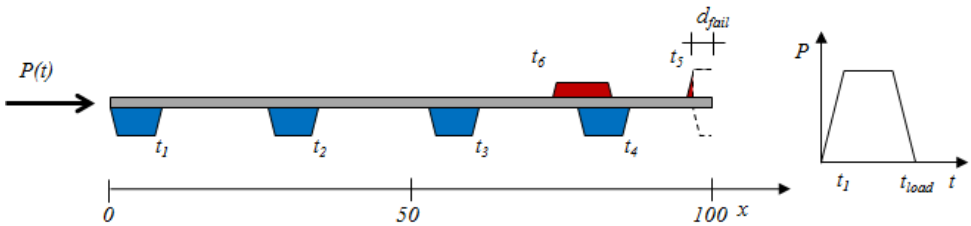


Figure 2.8: Schematic representation of 1D spalling test.

In the first case, shown in fig. 2.9, fracture takes place far from the right edge ($d_{fail} \gg l_r$). In both nonlocal models, the evolution of damage (ω) and nonlocal variable ($\bar{\kappa}$) is approximately symmetric and centered at the correct position. In the stress-based model the weight function diminishes progressively as damage develops leading to a more realistic description of a sharper damage zone.

In the second scenario, shown in fig. 2.10, the pulse load duration was reduced in order to obtain fracture very close to the free edge. In the standard nonlocal model, although damage initiation occurs at the correct position, it rapidly disperses in a wider zone and its apex ‘moves’ in the direction of the reflected wave (figs. 2.10(a-b)). In this case $d_{fail} < l_r$ so, in the presence of a fixed interaction domain the averaging process is unbalanced around the failure zone leading to the observed skew dispersion of damage. In contrast, the stress-based nonlocal model correctly predicts the fracture location with damage evolving around the initially damaged elements. In this case, only the stressed elements may contribute to damage growth, so the unloaded elements, as the ones close to the free edge during the wave reflection, are not considered in the weight averaging process.

From these results one may conclude that the issue of incorrect initiation and propagation of damage associated with traditional models with a fixed nonlocal internal length is minimized by the stress-based nonlocal formulation. The spurious boundary effects and the over-prediction of the width of the damaged zone observed in the standard nonlocal model are improved, also in dynamic simulations.

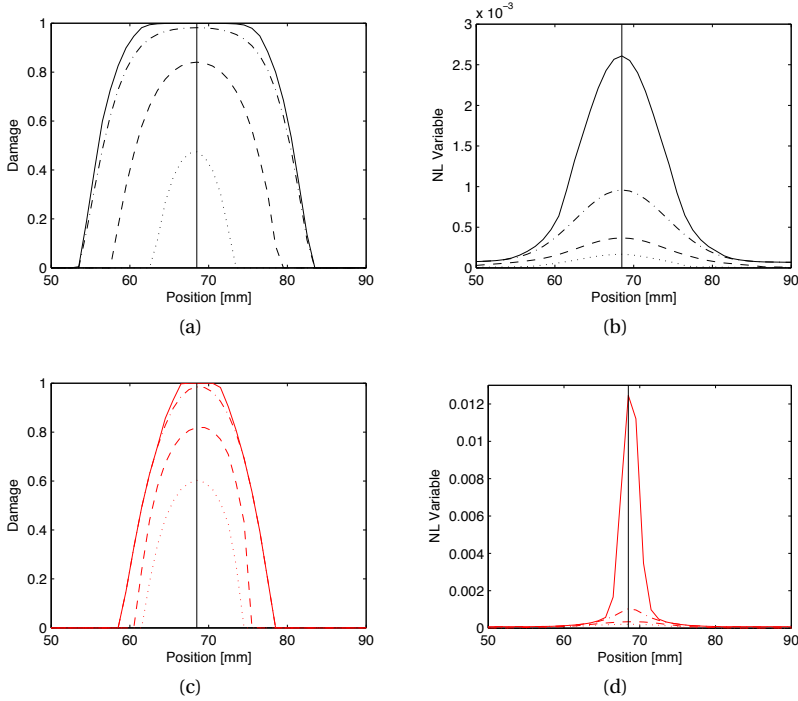


Figure 2.9: Damage (ω) and nonlocal variable $\bar{\kappa}$ evolutions for 1D spalling test with $t_{load} = 20 \mu s$.
 (a-b) standard nonlocal and (c-d) stress-based nonlocal models.
 (Data plotted at times 32, 34, 37 and 61 μs)

2.5 RATE DEPENDENT MODEL

As mentioned in the introduction, concrete-like materials are strain rate sensitive, exhibiting a significant strength increase when subjected to impulsive loadings, as generated by explosions or high velocity impacts. So far, there is no full understanding of the strain rate effect, in particular in the post-peak regime. Thus, for the present study, a strain-rate dependent formulation, similar to the one introduced by Pontiroli et. al [78], has been considered. In this approach only the damage threshold κ_0 in eqs. 2.7 and 2.8, is modified as a function of rate, here defined as the time variation of the nonlocal variable ($\dot{\bar{\kappa}}$):

$$\kappa_0^{dyn} = \kappa_0 + \eta_0 \dot{\bar{\kappa}}^{n_0} \quad \text{with} \quad \dot{\bar{\kappa}} = \frac{\partial \bar{\kappa}}{\partial t} \quad (2.17)$$

where η_0 and n_0 are material constants. The damage threshold κ_0^{dyn} is considered a variable only updated up to damage initiation and kept fixed from that moment on. This provides a numerically stable solution.

$$\kappa_0^{dyn}(t) = \max \kappa_0^{dyn}(\tau) \quad \text{for all } t \geq \tau \quad \text{and} \quad \omega = 0 \quad (2.18)$$

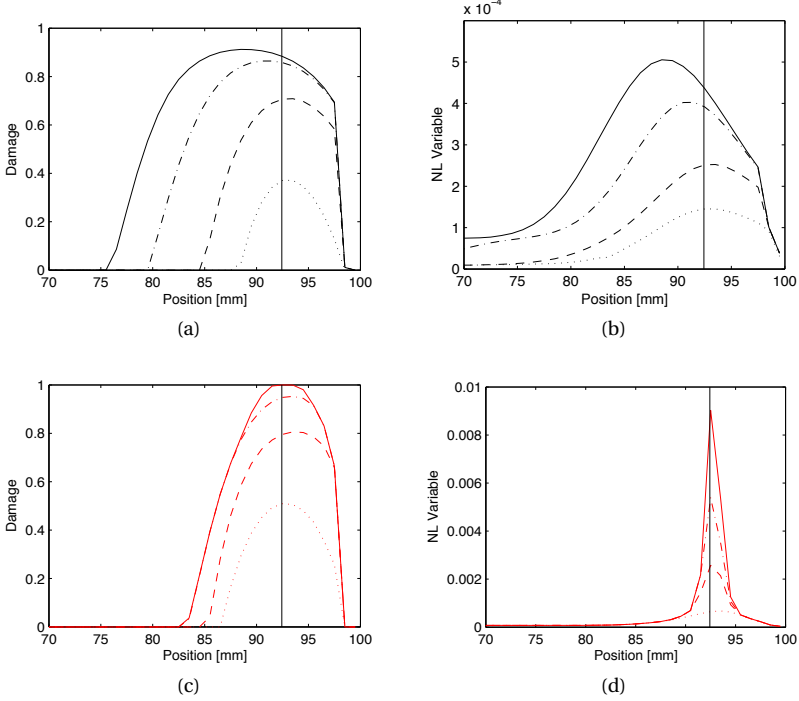


Figure 2.10: Damage (ω) and nonlocal variable $\bar{\kappa}$ evolutions for 1D spalling test with $t_{load} = 6 \mu s$.
(a-b) standard nonlocal and (c-d) stress-based nonlocal models.
(Data plotted at times 32, 34, 37 and 61 μs)

In order to avoid that κ_0^{dyn} exceeds κ_f and to promote a decreasing softening behavior with rate, the ultimate tensile equivalent strain κ_f is also updated with rate:

$$\kappa_f^{dyn} = \kappa_0^{dyn} \frac{\kappa_f}{\kappa_0} \quad (2.19)$$

Under compression, a similar effect is directly ensured because the condition $A_c B_c \kappa_0 = a_c - 1$ is considered in this study [72]. This ensures a continuous variation of slope of the compressive stress-strain curve.

The definition of this new rate-dependent damage model is only completed with the proper change to the nonlocal formulations. This has been done by updating the tensile strength (f_t) in the definition of ρ_i in eq. 2.12 by:

$$f_t^{dyn} = \kappa_0^{dyn} E \quad (2.20)$$

One may notice that the observed rate sensitivity of the elastic properties (such as the Young's modulus - E) are not taken into account. Since this phenomenon is considerably less significant than the strength sensitivity with respect to rate, it has

been ignored. However, it is noted that it may be included via an additional viscoelastic contribution.

2.5.1 EXPERIMENTAL VALIDATION

An experimental research project at Delft University of Technology has been conducted to characterize the dynamic tensile response of concrete [71]. In this section, two of the performed experiments are simulated in order to access the potentialities of the implemented model on representing the dynamic tensile failure of quasi-brittle materials.

In the experimental framework, two different set-ups of the split Hopkinson Bar test were used. With a gravity driven Split Hopkinson Bar (SHB) set-up (fig. 2.11a)) it was possible to study the dynamic response of concrete at intermediate loading rates ($\approx 50\text{ GPa/s}$ or 1 s^{-1}). A drop weight generates a relative long tensile load pulse, when compared to the specimen length, that propagates elastically through the incident (lower) bar. At the interaction between the incident bar and the specimen, this wave is partially transmitted and failure of the concrete specimen occurs. The residual tensile wave, which represents the strength of the concrete specimen, is then registered at the strain gages in the transmitter (upper) bar. Long aluminum bars are necessary to avoid reflecting waves interferences.

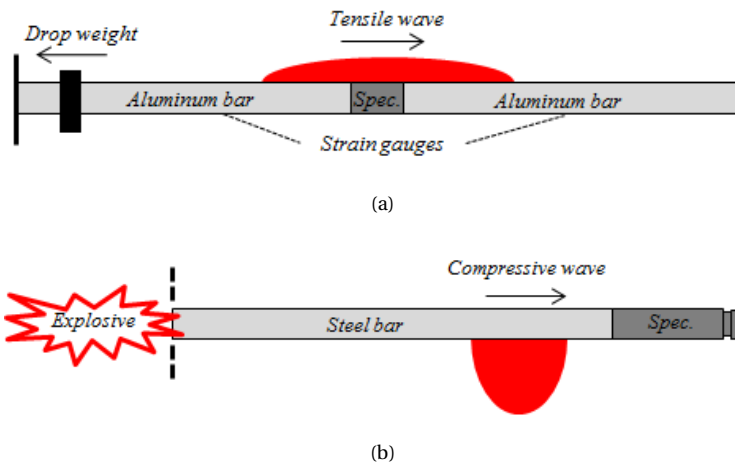


Figure 2.11: Schematic representation of the experimental set-up:

a) Tensile Split Hopkinson Bar test and b) Modified Split Hopkinson Bar (spalling) test.

In order to achieve higher loading rates a Modified Split Hopkinson Bar (MSHB) was considered (fig. 2.11b)). In this set-up only the incident bar is used. At one end of the bar a concrete specimen is attached, and at the other end a compressive elastic shock wave is generated by an impactor or the detonation of an explosive. At the interaction between the incident bar and the specimen, this compressive wave is partially transmitted. When this new elastic wave reaches the free edge of the specimen, reflection occurs and the sign of the wave changes leading to the tensile failure of the specimen. This is known

as the spalling technique and allows to reach stress/deformation rates in the order of 1000 GPa/s or 50 s^{-1} . The complete description of the experiments can be found in literature (e.g. Vegt et al. [71]).

2

MATERIAL MODEL CALIBRATION

Both experiments simulated hereafter were realized using the same concrete material. The parameter set of the damage model (see tab. 2.3) results from a general calibration procedure supported by single element uniaxial simulations, taking into consideration the quasi-static properties measured during the experimental campaign.

Table 2.3: Parametrization of the nonlocal rate-dependent damage model

Symbol	Parameter	Symbol	Parameter	Symbol	Parameter
E	35 GPa	ρ	2400 kg/m ³	ν	0.16
f_t	3.3 MPa	κ_0	f_t/E	κ_f	$5 \kappa_0$
A_c	1.34	B_c	2537	η_0	7.0×10^{-5}
l_r	10 mm	l_{min}	mesh size	n_0	0.33

The rate parameters considered (η_0 and n_0) are the ones that provide a close fit to the peak stress measured in the experiments. The uniaxial tensile stress-strain relations produced by this model in a single element test for different loading rates are presented in fig. 2.12a). The dynamic increase factors ($\text{DIF} = f_t^{dyn}/f_t^{stat}$) are compared with the CEB recommendation [16] for concrete under tension and the experimental results (see fig. 2.12b)).

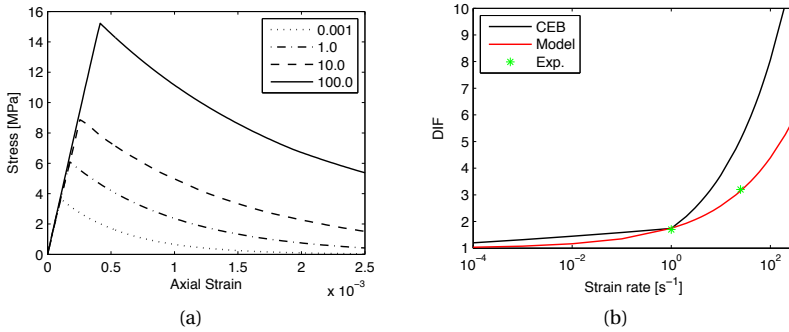


Figure 2.12: Single element uniaxial tension test at different strain rates ($\dot{\epsilon}$):
a) stress-strain relations and b) Dynamic Increase Factor (DIF).

Finally, the proper calibration of the nonlocal internal length (l_r) is not a trivial task. Although this quantity is usually related to the theoretical width of the fracture process zone (material characteristic length), its actual definition is not completely clear. After some experimentation, $l_r = 10 \text{ mm}$ was considered adequate to represent the

interaction domain of the material. The influence of this parameter in the response is not discussed in this chapter.

TENSILE SPLIT HOPKINSON BAR TEST

The Split Hopkinson Bar (SHB) set-up at the Delft University of Technology consists of two vertical cylindrical aluminum bars, with a diameter of 74 mm and a total length of about 10 m, between which the concrete specimen was glued. Considering that purely elastic behavior is expected to occur in the aluminum bars, it is reasonable to assume that wave dispersion effects in the incident and transmitter bars are negligible. So, for numerical efficiency reasons, only 1.5 m of each aluminum bar has been simulated. The specimen geometry and the strain gages located 750 mm from each side of the specimen were modeled as in the actual experiment (See fig. 2.13). The tensile loading originally generated by a drop weight is simulated by a tensile force distributed along the edge of the incident bar ($F(t)$) such that the deformations (strains) registered at the incident bar strain gage (SG_I) are replicated. This experimental set-up was modeled with a structured mesh with element sizes of 4 mm, 2 mm and 1 mm using an axisymmetric formulation.

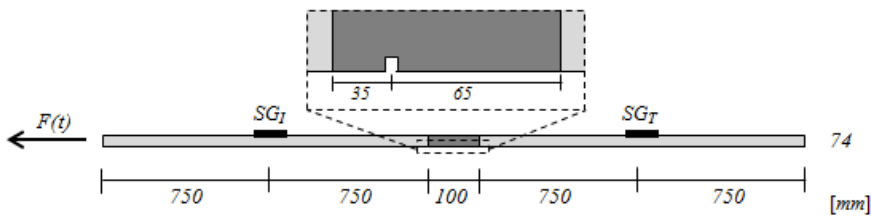


Figure 2.13: Model of the tensile split Hopkinson bar test with a notched specimen.

Fig. 2.14 shows the final damage profiles across the specimen for the different models and mesh refinements. The deformation measured at a strain gage located at the transmitter (upper) bar (SG_T) are compared with the average experimental results in fig. 2.15. As expected, the damage distribution (fig. 2.14a) and the deformations (figs. 2.15a) of the local model are mesh dependent. In contrast, the results of both nonlocal models are fairly mesh independent, although mutually different.

The most evident difference between the three models is the final damage profile. The bifurcation of the damage zones, visible for the local model, disappears with standard nonlocal averaging, however it is recovered by the stress-based formulation. The contraction of the interaction domain in the direction of the principal stresses in the vicinity of the damage areas leads to a desirable localization effect, resulting in a notorious contraction of the damage profile. The stress-based nonlocal model further improves the standard formulation ones by properly predicting damage initiation and growth from the crack tip inwards without damage spreading around the notch. It is worth noting that, in both nonlocal models, the final damage profiles are slightly different for all meshes, i.e. the damage distribution is smoothen out with mesh refinement. This is expected because when a 4 mm mesh (M4) is used with a nonlocal

internal length of $l_r = 10$ mm, there are only $2.5(= l_r/l_{element})$ elements across the interaction domain radius. Nevertheless, the results show that it is possible to obtain objective output from both nonlocal formulations even with relatively coarse meshes.

2

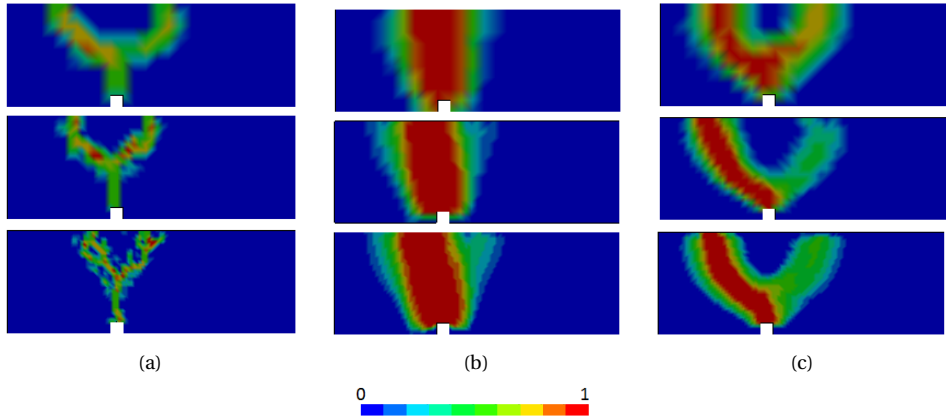


Figure 2.14: SHB - Final damage profile ($t = 1000 \mu s$) for meshes of 4 mm, 2 mm and 1 mm (refinement increases top to bottom): a) local; b) standard nonlocal and c) stress-based nonlocal.

The predictions for the deformation (fig. 2.15) are also different for all models, especially the deformations at which the peak tensile stress takes place. The highest stresses are registered with the standard nonlocal model. The second highest values come from the stress-based nonlocal model. Finally, the local model shows the smallest tensile strength prediction. From the first to the last model, the effective internal length contracts from $l_r = 10$ mm, fixed in the standard nonlocal formulation, to an 'internal length' of the size of a single element in the local model. In the intermediate scenario we have the stress-based nonlocal formulation in which the interaction domains are not fixed and tend to contract around the discontinuities (like notches) and damaged areas ($l_r \leq 10$ mm). In this experiment, a non-uniform distribution of stresses is observed across the specimen section where damage takes place during the failure process between the notch tip and the core of the specimen (vertical line across the notch in fig. 2.14). The stresses registered at the tip of the notch, in this example, are significantly higher than the ones at the core of the specimen. So, with the reduction of the number of elements that contribute to the failure process the average peak stress also reduces, i.e. the highest stresses are related with bigger damage areas (cf. figs. 2.14 and 2.15). For example, in the local model, with mesh refinement the higher stresses concentrate in fewer elements close to the notch, having a smaller contribution to the overall failure process. Consequently the peak stresses decrease with mesh refinement.

Although both nonlocal models apparently have a mesh independent response, a closer look to the results of the stress-based nonlocal model (fig. 2.15c)) reveals a slightly higher stress prediction for the finer mesh. In this case, the center part of the 4 mm wide notch is discretized by four elements (of 1 mm). Considering that the interaction domain expands in the direction of the principal stresses, in the

stress-based nonlocal model, during damage initiation the elements that are considered for averaging are the most stressed ones. Thus, the model tends to show localization in the center of the notch leading to a higher concentration of stresses in this zone and a slightly different and more realistic distribution of damage. This suggests that mesh refinement should be considered around physical discontinuities such as notches in order to improve the representation of failure with the stress-based nonlocal formulation.

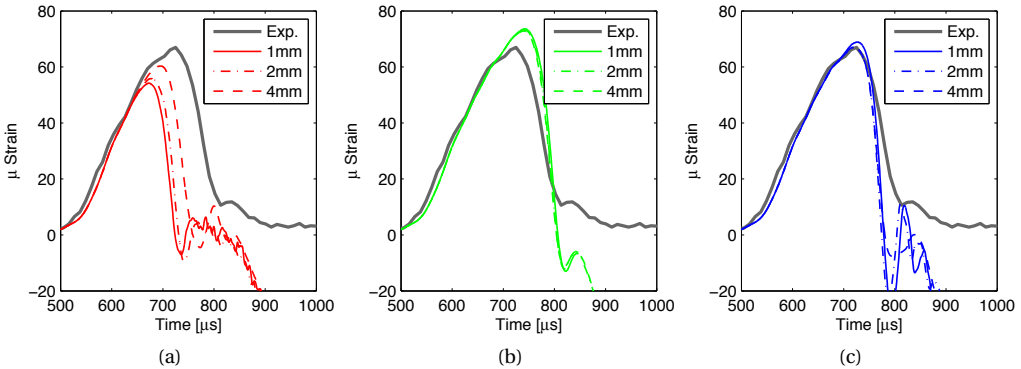


Figure 2.15: SHB - Strains evolution at transmitter bar (SG_T). Comparison with experimental results: a) local; b) standard nonlocal and c) stress-based nonlocal.

MODIFIED SPLIT HOPKINSON (SPALLING) TEST

The Modified Split Hopkinson Bar (MSHB) set-up consists of a 2 m long steel bar and a 300 mm long specimen attached on one edge, both with a 74 mm diameter specimen. Like in the previous example a notch was used to enforce the location of failure in the concrete specimen. Several strain gages ($SG1$ to $SG3$) located at the surface of the specimen (see fig. 2.16) were used to measure the longitudinal deformations. Since the incident pulse length, registered at $SG1$, is shorter than the specimen and the contact between the steel bar and the concrete specimen was lost immediately after loading, there is no need to simulate the complete apparatus.

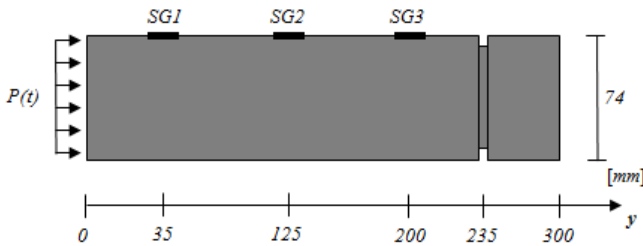


Figure 2.16: Model of the modified split Hopkinson bar with a notch specimen.

Here, only the specimen was modeled and the compression shock wave originally created by a blast is simulated by a pressure load uniformly distributed along the specimen edge as demonstrated in fig. 2.16. This load was designed in such a way that the strains measured at SG1 coincide with the ones registered in the experimental campaign. As in the previous example an axisymmetric model with three mesh refinements (4 mm, 2 mm and 1 mm) has been considered.

The results in figs. 2.17 to 2.19 show the final damage profiles and the stains at SG3 for the three versions of the proposed model and different mesh refinements. These strains are compared with the average strains measured at the same positions in the actual test. Similar to the previous example, only the local model reveals spurious mesh dependency. In this case, a bigger difference between the models, in addition to the damage profiles, is seen for the post peak response.

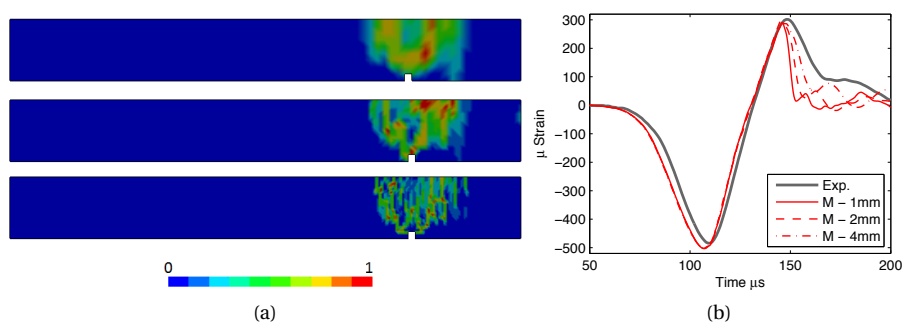


Figure 2.17: Modified split Hopkinson bar test – local model: a) Final damage profiles ($t = 200 \mu\text{s}$) for meshes of 4 mm, 2 mm and 1 mm (refinement increases top to bottom) and b) Strain evolution at SG3.

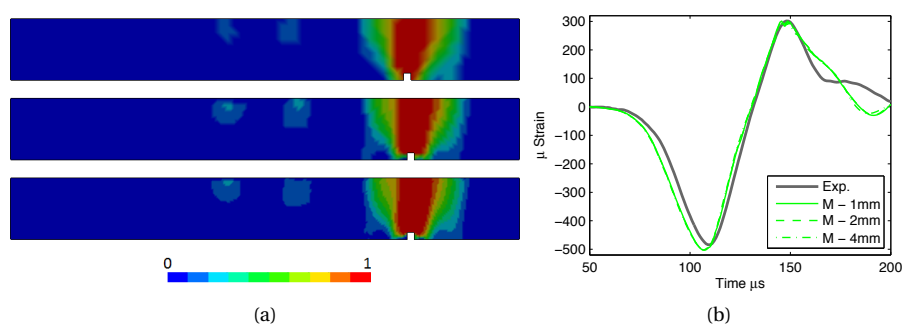


Figure 2.18: Modified split Hopkinson bar test – standard nonlocal model: a) Final damage profiles ($t = 200 \mu\text{s}$) and b) Strain evolution at SG3.

Unlike in the Split Hopkinson Bar case, a high rate short duration loading pulse induces a more uniform distribution and rapid variation of stresses in the failure region,

leading to an almost uniform stress distribution across the notch section. So, the concentrated stresses around the notch have a smaller influence on the averaged response of the model and the peak stress predictions are almost coincidental. The softening behavior of the models, on other hand, is directly related to the ‘amount’ of damage and its distribution. For example, as it is well known, upon mesh refinement the global response of the local damage model becomes more brittle, as a consequence of a reduction of the damaged area/volume (see fig. 2.17a)). Thus, it is natural to expect that the stress-based model reveals a more brittle behavior than the standard nonlocal formulation, as it can be seen by comparing figs. 2.18 and 2.19.

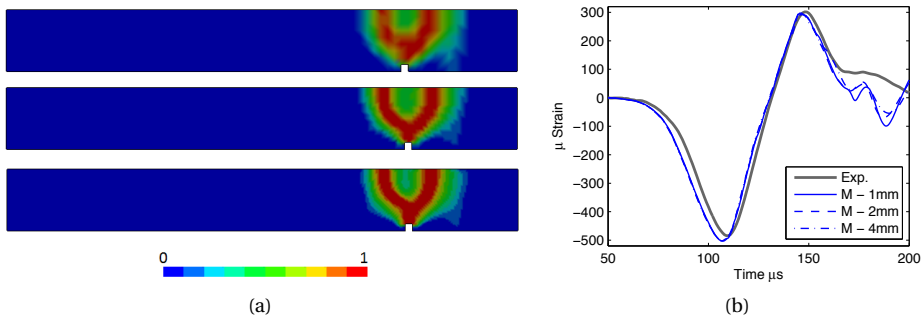


Figure 2.19: Modified split Hopkinson bar test – stress-based nonlocal model: a) Final damage profiles ($t = 200 \mu\text{s}$) for meshes of 4 mm, 2 mm and 1 mm (refinement increases top to bottom) and b) Strain evolution at SG3.

Overall, these simulations appear to agree reasonably well with experimental data. However, the post-peak response is not correctly represented. It is also not clear whether the damage profile properly represents the crack patterns (fracture process zone) observed in the experimental campaign. This is to be expected since in the proposed model only the peak-stress is updated with rate. These results suggest that the strain-energy (softening-law) should also be updated with rate. Furthermore, rate is only accounted for in the elastic regime. Although this simplification is acceptable for the pure mode-I examples explored in this chapter, the definition of rate has to be improved for a more general applicability of the model. Therefore, further investigation is recommended to fully evaluate the potential of this model. Nevertheless, it has been clearly shown that the stress-based nonlocal regularization technique associated to a rate-dependent damage law minimizes spurious boundary effects and the over-prediction of dispersion of damage observed in standard nonlocal models. The stress-based nonlocal approach yields a better solution for modeling damage initiation and propagation in dynamic tensile dynamic failure conditions.

To close this chapter, a final remark on the numerical efficiency of the presented models is given. By adding rate-dependency to the constitutive relation, the efficiency of the explicit computational scheme, used to compute the nonlocal quantity, decreases considerably. In the two examples presented above, convergence was only met when considerably smaller time steps are taken than the ones needed for the

rate-independent cases. Nevertheless, the stress-based nonlocal model is consistently more efficient, with convergence being met for $T_{Fac} < 0.2$, in contrast with a $T_{Fac} < 0.05$ needed in the standard nonlocal model.

2

2.6 CONCLUSION

A new rate-dependent nonlocal damage model is presented. A stress-based nonlocal criterion was coupled to a rate-dependent damage model and implemented using a fully explicit computational scheme. Several numerical examples are presented to evaluate the computational capabilities of the proposed model in simulating damage in dynamic tensile failure problems. The model is validated against two experiments carried out with the Split Hopkinson Bar technology.

The stress-based nonlocal damage model uses a variable interaction domain defined as a function of the stress-state of neighboring elements. A contraction of the internal length (l_r) in the direction of the smaller principal stresses is induced. The result is a more realistic localization effect observed in a direction perpendicular to free boundaries and other discontinuities. The efficiency of this nonlocal formulation has only been tested in earlier works in a rate-independent framework. Here, it was further developed and coupled to a rate-dependent damage model in order to study the dynamic tensile failure of concrete.

The proposed nonlocal formulation, in addition to correcting spurious mesh sensitivity, also provides a more realistic representation of damage. This model effectively solves the problems with damage initiation and growth near discontinuities. For example, in the crack tip problem, damage initiation and growth is properly predicted from the crack tip inwards, without spreading around the notch. It was also observed that objective results are obtained even with relatively coarse meshes.

In this study, different nonlocal variables have been considered. It was shown that the use of κ , instead of the traditionally considered equivalent strain (ϵ_{eq}), to determine the nonlocality of the model leads to qualitatively equivalent results. However, it was concluded that the use of a monotonically growing variable, such as κ , is considerably more efficient, especially in dynamic problems characterized by abrupt changes in the stress field.

In the numerical algorithm, the nonlocal quantities are determined as a function of the stress-state in the previous time step instead of the current time step. It was observed that a reduction of only 25% of the generally proposed fraction of the critical time step ($T_{Fac} = 0.75 \times 0.9$) is needed to ensure convergence with the rate-independent model. The numerical efficiency decreases considerably when the rate-dependent formulation is considered. For the examples presented in this chapter, objective results are obtained only if $T_{Fac} < 0.2$ for the stress-based nonlocal model, and $T_{Fac} < 0.05$ for the standard nonlocal formulation. Since, in the considered rate dependent formulation, the damage threshold is no longer fixed, a smaller time step is needed to properly accommodate its variation within the nonlocal averaging domain, as a function of rate. Nevertheless, although relatively small time steps are needed to ensure numerical stability, such algorithm is particularly interesting for explicit finite element packages, such as LS-DYNA.

3

STUDY OF DYNAMIC TENSILE FAILURE OF CONCRETE NEW *effective rate dependent* DAMAGE MODEL

This chapter focuses on correcting the limitation of the model proposed previously. A strain-rate dependent version of the μ damage model, recently proposed by Mazars, is used to describe the strength and fracture energy increase of concrete under dynamic tensile loading conditions. However, instead of the commonly used instantaneous strain-rate ($\dot{\epsilon}$) to update the constitutive law, an effective rate ($R(\dot{\epsilon}, t)$) is considered. With this new concept a time scale is introduced in the constitutive law which restrains the 'evolution of strain-rate', to represent the inherent dynamic properties of concrete. This has a weak regularization effect and acts as a localization limiter. Mesh objectivity is recovered with the addition of a material length scale to the constitutive relations, here accomplished by an explicit stress-based nonlocal regularization scheme.

Two sets of modified split Hopkinson bar tests are simulated for validation, using respectively notched and un-notched specimens. The results are objective and in good agreement with the experiments.

This chapter is based on L. Pereira, J. Weerheijm, and L. Sluys. A new effective rate dependent damage model for dynamic tensile failure of concrete. *Int. J. Fract.*, 176:281–299, 2017.

Under dynamic transient conditions, concrete is known to exhibit a significant dynamic strength increase [16] in tension [79] and, to a smaller extent, in compression [80]. This increase is associated with a rise of both stiffness and fracture energy. The consideration of these strain-rate effects in the design of critical (infra-)structures, such as power plants, dams, bridges and hospitals, is crucial to protect ourselves and our societies from the devastating effects of extraordinary actions such as earthquakes, explosions, impacts and other highly dynamic loading situations. Therefore, the development of realistic numerical tools to efficiently simulate the dynamic failure of concrete is of paramount significance.

Although rate dependency of concrete has been known for a century now [81], the understanding of the underlying physical mechanisms is far from complete, despite the numerous experimental and numerical studies on dynamic fracture of quasi-brittle materials. It is more or less common knowledge that the dynamic response of concrete is directly related to the viscous behavior of the bulk material, as well as to the inertia effects at multiple scale levels that directly and indirectly control the cracking (damage) process. As it is well known, the evolution of cracks cannot expand arbitrarily fast [82–84]. Since damage in concrete is essentially the result of the initiation, growth and coalescence of micro-cracks, its evolution is a strongly time dependent phenomenon [85]. At high deformation rates ($\geq 1 \text{ s}^{-1}$), crack propagation is retarded due to inertia effects at the crack tip [64, 86, 87]. At low to moderate deformation rates, the enhanced resistance of the material is mainly caused by moisture in the pores [88, 89]. Due to viscous forces caused by the *Stefan effect*, the crack initiation process is delayed. In either case, the evolution of damage is delayed due to an apparent resistance to straining [11], which results in a retarded crack opening process. This retardation of cracking (damage) is usually nominated as the main cause of the observed dynamic strength increase. Additionally, with increasing loading rates, more micro-cracks are activated at the same time, leading to an increase of effective fracture surface (damage) and of the dynamic fracture energy [6, 90, 91].

The viscous properties of the bulk material also have a considerable influence on the dynamic response of quasi-brittle materials. Eibl and Schmidt-Hurtienne [35] demonstrated that in case of rapid variations of the loading rate, its effects are not ‘felt’ instantaneously. The material has some kind of *memory*. Thus, in case of a sudden drop of the deformation rate an inertial-related stress relaxation process is triggered and a certain time is needed for the stress-strain state to evolve to the new rate-dependent condition.

Finally, mass inertia effects at the structural level have also been identified as another potential contributor to the dynamic strength increase. Several numerical studies with the split Hopkinson pressure bar (e.g. [92–95]) showed that the strength increase under uniaxial compression is partially caused by triaxial compressive stress states associated with inertial lateral confinement. On the other hand, Lu and Li [96] demonstrated that in the dynamic splitting test the material strength is hardly affected by stress triaxiality. Under uniaxial tensile loading condition (direct tension or spalling tests), triaxial tension stress states are induced. Thus, although structural inertial effects partially explain the strength increase under compression, it cannot explain the dynamic tensile response [97].

It has been demonstrated that the retardation of micro-cracking at high deformation rates associated with micro and meso-scale inertia effects can be analyzed by a rate-independent model as long as the material is discretized in all its phases (aggregates, cement paste and voids) [98]. However, this is not possible with phenomenological models, which provide homogenized macroscopic representations of the material. Rate enhanced formulations must be considered in order to explicitly simulate the underlying dynamic mechanisms which cannot be captured and need to be simulated explicitly, as intrinsic material properties [35, 85, 97]. That is, the description of rate effects within the constitutive law must be adjusted to the level of representation [35].

From a macroscopic point of view, rate dependency of concrete-like materials is often characterized by dynamic strength increase factor (DIF) functions. Many models based on continuum plasticity and/or damage mechanics have been developed over the years using these semi-empirical equations to increase the strength of the model with rate so as to fit laboratory test data. However, these models usually cease to be predictive in new situations because, despite their experimental foundation, DIF laws are not truly materials constitutive relations. They ignore the time dependent phenomena which control the dynamic evolution of damage such as the effect of inertia in the evolution of damage, and the history of deformations. Thus, adopting the current strain state and the *instantaneous* rate ($f(\varepsilon, \dot{\varepsilon})$) to derive the dynamic constitutive relations, as is usually done in *hydrocodes*, does not adequately describe the complex evolution of stresses and damage in dynamics. New sound and physically justified approaches are needed.

Various enhanced formulations have been proposed in the last two decades describing the dynamic evolution of damage as a time dependent phenomenon. Viscous-damage formulations, similar to a Perzyna-type of viscoplasticity, have been used to describe the rate of damage (see for example [25, 37, 99]). Plotzitz et al. [85], following Eibl and Schmidt-Hurtienne's work [35], proposed a formulation where the evolution of damage depends, to some extent, on the immediately preceding strain history. A history function, derived from a simple Maxwell rheological model, is used to retard the evolution of damage, representing the resistance to micro-cracks growth due to inertia effects. Recently, Haussler-Combe and Kuhn [97] proposed a model to address both the viscosity of the bulk material and the dynamic retardation of damage.

In this contribution, a stress-based nonlocal (SBNL) rate-dependent damage formulation is used to describe the strength and fracture energy increase with rate. This model was developed as an extension of the authors' previous work, in the attempt to mitigate the limitations of the model published at Pereira et al. [33]. Two main modifications were made to the model. First, the underlying damage law was revised. A simplified version of the newest Mazars' damage model [52] is used instead of his original one [24]. This alters the dynamic evolution of damage, especially in tension-compression stress states. Second, the constitutive law is updated according to an *effective rate* (R) instead of the *instantaneous* strain-rate ($\dot{\varepsilon}$) (see for example [17–19, 100]). With this new concept, the evolution of 'rate' is restricted to account for the delayed response of the material to stress/strain variations due to inherent inertia properties and retarded crack opening processes observed in

dynamics.

In the following section, the stress-based nonlocal damage model is briefly described. In section 3.2 the *effective rate* concept is presented and combined with a strain-rate dependent formulation, as an enhancement of the proposed model. Finally, a set of numerical studies of dynamic tensile failure of concrete is presented for validation. First (section 3.3), a one-dimensional spalling example is used to explore the new properties of the proposed model, namely the influence of the time and material length scales. Then (section 3.4), two sets of experiments of a modified split Hopkinson bar, using notched [71] and un-notched [101] specimens, are simulated for 'experimental' validation of the model (see. 3.4).

3.1 STRESS-BASED NONLOCAL DAMAGE MODEL

Continuum damage mechanics has been widely and successfully used to model concrete for a broad range of applications and loading conditions [24, 27, 54]. For the present study, a simplified version of the μ *damage* model, recently proposed by Mazars et al. [31], has been implemented in LS-DYNA [48]. In the original formulation, two damage modes are considered to describe the material stiffness degradation under tension and compression. In the present study, however, since only pure mode I failure is under investigation, only the tensile damage effects are modeled.

3.1.1 DAMAGE MODEL

A classical isotropic damage formulation is considered. The single scalar damage variable ω represents the material stiffness degradation, due to tensile cracking. Damage evolves from zero (virgin or undamaged material) to one (complete failure). It is assumed that the Poisson's ratio is not affected by damage, i.e. the relative reduction of all stiffness coefficients is the same and independent of the loading direction. The stress tensor is expressed as:

$$\sigma = (1 - \omega) \tilde{\sigma} \quad \text{with} \quad \tilde{\sigma} = C : \varepsilon, \quad (3.1)$$

where ε is the strain tensor, C is the elastic stiffness tensor and $\tilde{\sigma}$ is the effective-stress tensor [102]. The evolution of damage in time (t) is derived from the thermodynamic variable Y_t which is the historical maximum equivalent strain (ε_t):

$$Y_t(t) = \max_{\tau \geq t} \varepsilon_t(\tau) \quad (3.2)$$

$$\varepsilon_t = \frac{0.5}{1 - 2\nu} I_\varepsilon + \frac{0.5}{1 + \nu} \sqrt{3J_\varepsilon} \quad (3.3)$$

where ν is the Poisson's ratio. I_ε is the first invariant of the strain tensor and J_ε is the second invariant of the deviatoric strain tensor, according to:

$$I_\varepsilon = \varepsilon_1 + \varepsilon_2 + \varepsilon_3,$$

$$J_\varepsilon = \frac{1}{6} [(\varepsilon_1 - \varepsilon_2)^2 + (\varepsilon_2 - \varepsilon_3)^2 + (\varepsilon_3 - \varepsilon_1)^2]$$

with ε_i being the principal strains. Damage initiates when the equivalent-strain surpasses the damage threshold (Y_{t0}). Its growth is described by the Kuhn-Tucker conditions:

$$f \leq 0 \quad \dot{Y}_t \geq 0 \quad \dot{Y}_t f = 0 \quad (3.4)$$

where $f(\varepsilon_t, Y_t) = \varepsilon_t - Y_t$ is the damage loading function. Finally, the softening relations or damage function is described by the original Mazars' exponential law [24]:

$$\omega = 1 - (1 - A_t) \frac{Y_{t0}}{Y_t} - A_t e^{-B_t(Y_t - Y_{t0})} \quad (3.5)$$

where A_t and B_t are material parameters.

3.1.2 REGULARIZATION MODEL

To overcome spurious mesh sensitivity, typical for standard 'local' damage models, a regularization scheme is needed. In this study the stress-based nonlocal formulation presented by Giry et al. [49] is used. Like in any other nonlocal formulation of integral type, the stress response in a material Gauss point (x) is made dependent on its neighbors (ξ) by weight averaging of a selected variable, which in the present study is ε_t . The respective weight averaged value within the interaction domain Ω is given by the following equation:

$$\bar{\varepsilon}_t(x) = \frac{\int_{\Omega} \alpha(x, \xi) \varepsilon_t(\xi) d\Omega}{\int_{\Omega} \alpha(x, \xi) d\Omega} \quad (3.6)$$

where $\alpha(x, \xi)$ is an arbitrary weight function, here considered to be the Gaussian function:

$$\alpha(x, \xi) = e^{-\left(\frac{2\|x - \xi\|}{l_r}\right)^2} \quad (3.7)$$

The nonlocal update of the damage model is simply attained by replacing ε_t by its nonlocal counterpart ($\bar{\varepsilon}_t$).

Although efficient in solving the mesh sensitivity problem [61], classical nonlocal formulations fail to properly describe damage initiation close to discontinuities (e.g. free boundaries and notches) and are prone to spurious damage dispersion upon complete failure. These erroneous results are a direct consequence of the fixed interaction domain characterized by a constant internal length l_r . In a stress-based nonlocal formulation, the influence of the neighboring elements stress state is introduced in the description of the nonlocal interactions by updating the interaction length $l_{x\xi}$ between the Gauss point x and its neighbors ξ in eq. 3.7 as follows:

$$l_{x\xi} = \rho(x, \xi) l_r \quad (3.8)$$

with

$$\rho^2(x, \xi) = \frac{1}{(f_t^{dyn})^2 \left(\frac{\sin^2 \varphi \cos^2 \theta}{\langle \sigma_1 \rangle^2} + \frac{\sin^2 \varphi \sin^2 \theta}{\langle \sigma_2 \rangle^2} + \frac{\cos^2 \varphi}{\langle \sigma_3 \rangle^2} \right)} \quad (3.9)$$

where φ and θ are the angles between the principal stresses σ_I , with $I = 1, 2$ and 3 , at point ξ , defined in the conventional spherical coordinates system. Considering that $\langle \cdot \rangle$

are the Macaulay brackets, the expression between parentheses is the projection of the positive part of σ_I over the vector $\overline{x\xi}$, $\langle \sigma_{x\xi} \rangle$, as it is depicted in fig. 3.1 for an example with $\sigma_1 > 0$, $\sigma_2 < 0$ and $\sigma_3 = 0$.

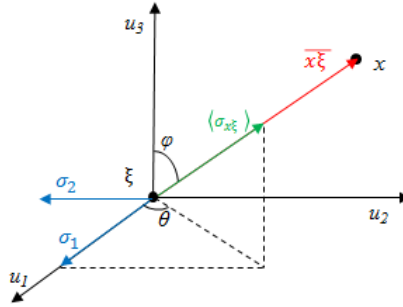


Figure 3.1: Spherical coordinate system used to compute $\rho(x, \xi)$.

So, $\rho(x, \xi)$ is the ratio between $\langle \sigma_{x\xi} \rangle$ and f_t , which has a value between zero and one for tensile stresses and is equal to zero otherwise. The interaction length between two points is allowed to vary between l_r and a minimum l_{min} , which in this study is always considered equal to the element size in the center of the interaction domain. A non zero interaction length must be used to prevent localization into a singularity when l_r in eq. 3.7 tends to zero. This would lead to numerical instabilities when stresses tend to zero or change sign. It is worth noticing that this formulation differs from the original [49] in two ways. First, the interaction between elements is only variable for tensile (positive) stress states. Second, the dynamic tensile strength f_t^{dyn} must be used instead of the static value f_t to account for the rate dependency of the model [33]. For more information about this model and the computation scheme used for this research, the reader is referred to the works by Giry et al. [30, 49] and Pereira et al. [33].

This stress-based nonlocal formulation, in combination with other isotropic damage models, has proven to realistically represent damage initiation and growth. During failure, the nonlocal interaction across the FPZ progressively decreases, leading to a strong discontinuity in the strain field upon complete failure [49]. Furthermore, in comparison to standard nonlocal modeling, the interactions close to free boundaries also improve, correcting the spurious damage dispersion around notches and free boundaries [33].

3.2 RATE ENHANCEMENT

As is well known, concrete is a highly rate dependent material, especially under tensile loading conditions. The experimentally observed strength and fracture energy increase is directly related to changes of the fracturing (damage) process with rate, as depicted in fig. 3.2. It is generally accepted that under quasi-static tensile loading conditions, the material undergoes three distinctive crack-deformation stages up to complete failure. The material response starts as (visco-)elastic with uniform distribution of stresses/strains across the specimen. During this stage (a) stresses concentrate around

multiple micro-cracks and other defects in the material matrix. With increasing deformation, just before and immediately after the peak stress, (b) micro-cracks start to develop and coalesce degrading the material stiffness and strength, i.e. damaging the material irreversibly. In a later stage (c), while single macro-cracks start to appear leading to complete material failure, the surrounding material relaxes. Considering the low deformation rates in static loadings, inertial forces can be neglected and the crack opening and material relaxation can be considered as *instantaneous* processes.

The main difference between the responses of the material under quasi-static and dynamic loading is ‘time’. In the dynamic situation, the supplied energy crosses through the structure at a certain velocity and damage is no longer instantaneous due to inertia, as explained in the introduction. At high deformation rates crack initiation is retarded (d and e in fig. 3.2) due to a combined effect of moisture in the pores of the material (*Stefan effect*) [88, 89] and reduced stress concentration at the crack tip due to inertia contribution in the dynamic equilibrium (*micro inertia* effects) [64, 86, 87]. Inertia also contributes to the observed limited crack propagation velocity. In any case, from a macroscopic point of view, this dynamically induced retarded crack opening process is seen as a resistance to straining and to damage evolution. Additionally, with increasing loading rates, more micro-cracks are activated at the same time and the distribution of micro (and macro) cracks across the fracture process zone (FPZ) changes. Thus, the effective fracture surface and consequently the fracture energy also changes with rate. Notwithstanding, it is not yet clear how the post peak relations (f) evolve from low to high loading rates. For example, it is accepted that for low to moderate strain-rates ($\dot{\epsilon} < 1\text{s}^{-1}$) the fracture energy is almost unaffected by rate [11]. But, it apparently increases significantly with increasing loading rates.

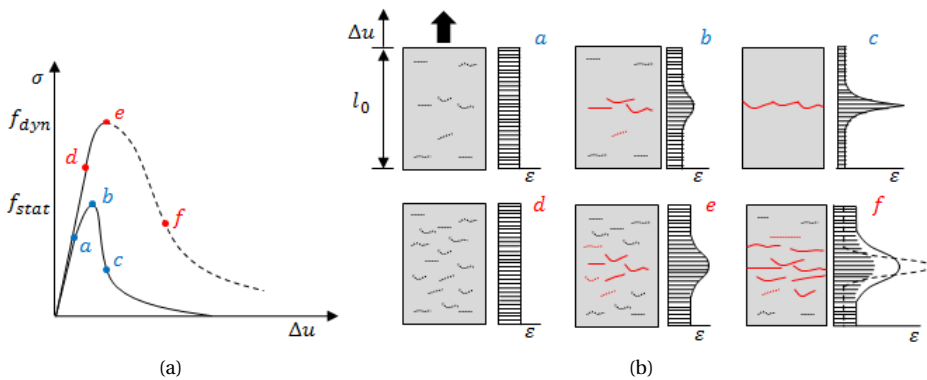


Figure 3.2: Behavior of concrete when loaded under tension at low and high loading rates. (a) Stress-displacement curves and (b) crack evolution.

The viscous behavior of the bulk material has also been pointed out as another cause of the time-dependent behavior of quasi-brittle materials. Eibl and Schmidt-Hurtienne [35] demonstrated that in case of a sudden change of the loading rate, its effects are not ‘felt’ instantaneously. In such cases, the material undergoes an

inertia-related stress relaxation process. In modeling perspective this implies that a certain time is needed for the stress-strain state to evolve to the new rate-dependent condition. This phenomenon can be easily understood with the theoretical example of an abrupt variation of the loading deformation rate, as represented in fig. 3.3. Obviously, a certain time delay is needed for the dynamic strength prevalent during the acceleration phase of the loading, to drop to the static strength which is expected after transition point *A*.

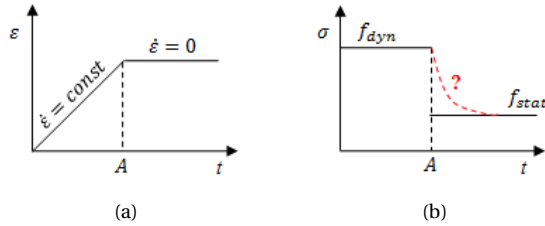


Figure 3.3: Eibl's fictitious experiments [35]. (a) loading, (b) evolution of dynamic strength

It is easily understood that, it is almost impossible to monitor the real time evolution of straining in the fracture zone under dynamic loading. The experimentally derived dynamic strength increase factor (DIF) functions are merely semi-empirical relations, which represent the average of the rate dependent response in the entire FPZ during the fracture/damage process. Consequently, these laws cannot be directly used in macroscopic models to simulate the dynamic behavior of concrete within the FPZ. As described before, multiple, somehow interdependent, phenomena contribute to the rate dependent response of concrete. Each individual contribution varies according to the specific composition of the material (e.g. maximum aggregate size and humidity), geometry of the specimen, loading conditions, etc.. These contributions to the dynamic response of the material are impossible to quantify at macroscopic level. So, the best way to overcome this barrier is by creating and testing new conceptual models. The contribution of different underlying physical phenomena have to be coupled in order to mimic the observed global response of the material in a phenomenological way.

In this study, macroscopic rate effects are phenomenologically described as combination of three mechanisms. (i) First, the dynamic strength and fracture energy increase, associated with an effective fracture surface growth with rate, is simulated by a rate dependent damage formulation. Additionally, a stress-based nonlocal enhancement is considered to obtain a more realistic and objective representation of the damage zone [33] and this may capture the broadening of the FPZ. (ii) Second, the dynamically delayed straining response of the material, i.e. the time dependent phenomena commonly associated with micro-inertia effects, is simulated by an *effective rate* R . With this concept the evolution of 'rate' is no longer instantaneous. It is delayed in order to simulate the effects of the dynamically retarded crack opening process and to viscous properties of the bulk material, respectively. (iii) Finally, the structural inertia effects are accounted for by the equations of motion.

3.2.1 STRAIN RATE DEPENDENT FORMULATION

A classical strain-rate dependent formulation is used. By updating the damage threshold (Y_{t0}) in eq. 3.2 according to the following equation, the strength of the material is updated with rate.

$$Y_{t0}^{dyn} = Y_{t0}(1 + \zeta_t R^{\eta_t}), \quad (3.10)$$

where ζ_t and η_t are user defined material constants, Y_{t0} is the static damage threshold, and R is the effective rate characterized in the following section. As it can be seen by the evolution of the stress-strain relations with rate in fig. 3.5(a) (dashed lines), of a material point analysis of a generically calibrated constitutive law of a concrete with $f_t = 3.0$ MPa (see tab. 3.1), the increase of strain/fracture energy (g_f/G_f) is minimal if only Y_{t0}^{dyn} is updated with rate. In order to account for the observed growth of fracture energy the post peak response of the material also has to be updated with rate. To that end, the parameter B in the damage law (eq. 3.5) is also made rate dependent:

$$B_t^{dyn} = B_t \left[1 - \delta_t \ln \left(\frac{R}{\dot{Y}_0} \right) \right], \quad (3.11)$$

where δ_t is an input parameter and \dot{Y}_0 is the rate after which the loading is considered dynamic. Consistently with the *fib* recommendation [16] $\dot{Y}_0 = 10^{-6} s^{-1}$ is considered.

3.2.2 DEFINITION OF EFFECTIVE RATE – R

Dependent on the level of representation (micro, meso or macro-scale) an inertia driven physical mechanism can be considered as intrinsic material property or as structural response. As discussed above, a macro-scale phenomenological representation of concrete should account for at least two underlying dynamic (inertia) properties of the material: (1) retarded crack initiation and opening process observed in dynamics due to the *Stefan effect* and/or due to (micro-)inertial effects at the crack tip and (2) delayed response/adaptation of the bulk material in the close vicinity of the cracks to rapid stress/strain variations. These phenomena, combined or individually, have been modeled as visco-elastic, visco-plastic, visco-damage, delayed/retarded damage, etc. [35, 85, 103]. In this research, the phenomena are considered to affect the evolution of straining in time. It is inferred that the variation of strain cannot occur infinitely fast. Consequently, the variation of strain rates ($\dot{\epsilon}$) must be delayed in time. This is described by a new *effective rate* (R) concept, which restricts the evolution of ‘rate’ in time to account for the delayed response of the material to strain-rate variations.

This concept is schematically explained by fig. 3.4, where R_{down} and R_{up} are the functions that limit the variation of *effective rate* (R) in case of an abrupt decrease ($\delta\dot{\epsilon}_1 < 0$) or increase ($\delta\dot{\epsilon}_3 > 0$) of the ‘instantaneous’ strain-rate ($\dot{\epsilon}$), respectively. $R = \dot{\epsilon}$ in case of small or no variation of straining ($\delta\dot{\epsilon}_2 \approx 0$).

$$R_{down} = \max_{t \geq \tau} \left[\dot{\epsilon}_t(\tau) e^{-\frac{t-\tau}{\lambda}} \right] \quad (3.12)$$

$$R_{up} = \min_{t \geq \tau} \left[\dot{\epsilon}_t(\tau) e^{\frac{t-\tau}{\lambda}} \right] \quad \text{for } \omega > 0 \quad (3.13)$$

where λ is a user defined *characteristic time* of the material, t is the current time and τ is the last time when the strain-rate was constant ($\dot{\epsilon}_t$). Please note that strain-rate is defined here as the variation in time of equivalent strain ϵ_t defined in eq. 3.3. Note that the parameter λ is directly related to the time needed for the material to accommodate to strain-rate variations. It is argued by Plotzitz et al. [85] that with increasing strain-rates the micro-cracks become smaller and more uniformly distributed, which induces a faster relaxation of stresses around defects reducing the reaction time of the material around a single defect. Consequently they propose that the characteristic time that governs the dynamic damage evolution is by itself rate-dependent. Here, for simplicity, and because the main goal of this chapter is to develop the *effective rate* concept, the characteristic time of the material is considered to be independent of the loading history and to be the same for relaxation and retardation.

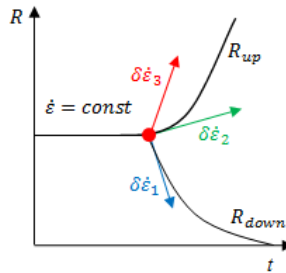


Figure 3.4: Maximum allowed evolution of strain-rate in time.

3.2.3 SINGLE ELEMENT SENSITIVITY STUDY

To illustrate the basic properties of the proposed model, simple point analysis were conducted considering constant and variable loading histories. Fig. 3.5 shows the variation of the stress-strain relations with rate ($R = \dot{\epsilon} = const$) and the respective DIF plot considering the model calibrated as described in tab. 3.1 for different values of δ_t . As usual for a rate dependent model of this class, the yield strain/stress increases with rate (eq. 3.10). If B_t is kept constant in the damage law (eq. 3.5) by considering $\delta_t = 0$ in eq. 3.11, the strain energy (area under the stress-strain curve) of the model is almost not affected (see dashed lines in fig. 3.5(a)). As it will be shown later, this leads to underprediction of the material dynamic fracture energy. So, a variable B_t^{dyn} is considered. As it can be seen, the evolution of damage is considerably altered by a growing δ_t (eq. 3.11), which significantly influences the model's strain energy but has a small impact on its dynamic strength.

Fig. 3.6 shows the stress-strain relations in case of an abrupt variation of straining after damage initiation, of plus or minus ten times the reference strain-rate ($\dot{\epsilon} = 0.2s^{-1}$), considering the constitutive law (cf. fig. 3.5 for $\delta_t = 0.045$) calibrated with different values for λ . As a reference, the stress-strain relations considering constant deformation rates throughout loading are plotted in black. It can be seen that when $\lambda = 0$, the material gains or loses strength almost instantaneously, leading to sudden

jumps in the stress-strain relations (red lines in fig. 3.6). When $\lambda > 0$, the evolution of stresses are smoothed out, in case of an abrupt variation of the loading rate. The use of R in the constitutive law has a desirable *viscous* effect on the evolution of damage in case of variable strain-rate loading histories.

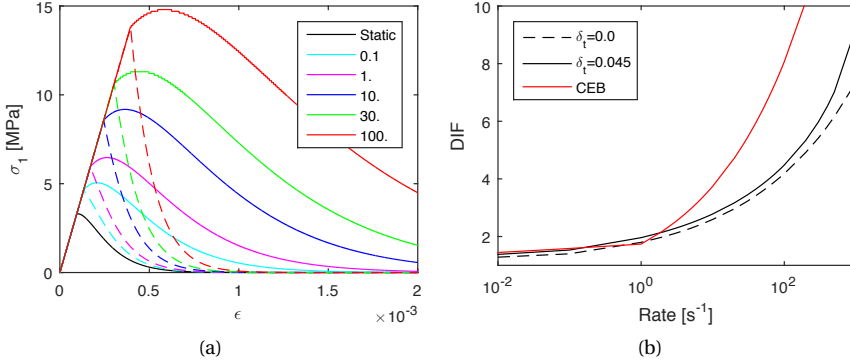


Figure 3.5: Single element uniaxial tension test at constant deformation rates up to 100 s^{-1} , considering $\delta_t = 0.0$ (dashed) and $\delta_t = 0.045$ (solid): (a) $\sigma - \epsilon$ relation for different loading rates and (b) respective DIF functions compared to CEB formulation [16].

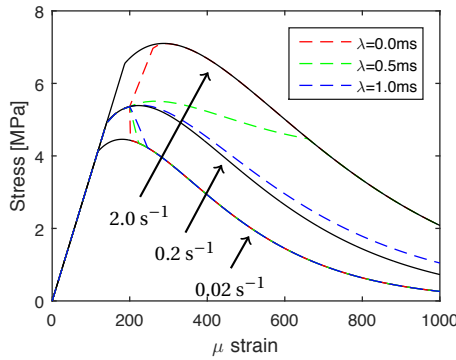


Figure 3.6: Stress-strain relations in case of a variation of the deformation rate after damage initiation, considering different λ .

Finally, it is worth mentioning that the proposed model is conceptually identical to the models by Plotzitz et al. [85] and Häussler-Combe and Kuhn [97]. In those models, a time scale was introduced in the constitutive law, through a *history function*, to explicitly control the evolution of damage with rate, taking into account the mechanics of microcrack opening, i.e. all phenomenological rate effects are simulated by a dynamic damage law. In the model proposed here, rate effects are partially segregated. The variation of strength and fracture energy due to the change of fracturing (comminution) are directly accounted for in the constitutive law, while the viscous

behavior of the bulk material and (micro and meso scale) inertia effects are simulated with R . This has the advantage of allowing the independent control of these two phenomena. Moreover, the proposed effective rate concept can be easily adapted to existing models without the need for especially designed damage laws to simulate viscous behavior of the material.

In the next section, a one-dimensional spalling example and two sets of experiments of a modified split Hopkinson bar are used for validation of the model under high loading rate conditions.

3

3.3 ONE DIMENSIONAL EXAMPLE – SPALLING

Various adaptations of the traditional split Hopkinson bar test have been developed over the years to characterize the dynamic behavior of concrete. A modified split Hopkinson bar (MSHB) setup is usually considered when high loading rates need to be activated. In this set-up only the incident bar is used. At one end of the bar a concrete specimen is attached, and at the other end a compressive elastic shock wave is generated by an impactor or by detonation of an explosive. The incident compressive wave propagates through the bar. At the interface between the incident bar and the specimen, this compressive wave is partially transmitted. When it reaches the free edge of the specimen, reflection occurs leading to tensile failure of the specimen. The magnitude of the incident wave is chosen small enough such that linear elastic behavior of the specimen is guaranteed under compression, but high enough to ensure tensile failure after reflection of the pressure wave. During the failure (damage) process energy is dissipated. The maximum intensity of the transmitted wave after failure is limited by the dynamic tensile strength of the material. The complete description of the experiments can be found in literature (e.g. [71, 101, 104]).

The one dimensional example elaborated in this section consists of a 200 mm long bar composed of one row of linear hexahedron elements with a single integration point and a 1 mm² cross section. Different mesh refinements were used for the mesh sensitivity studies, with element lengths varying from 1 mm (M1) to 4 mm (M4). A generic calibration of the constitutive law for concrete with $f_t = 3.0$ MPa was used and the Poisson ratio has been set to zero ($\nu = 0$) in order to preserve one-dimensionality (see tab. 3.1).

Table 3.1: Constitutive law parametrization – 1D spalling

Symbol	Parameter	Symbol	Parameter	Symbol	Parameter
E	30 GPa	ρ	2400 kg/m ³	ν	0.00
f_t	3.0 MPa	Y_{t0}	f_t/E	A_t	1.0
ζ_t	0.80	η_t	0.30	B_t	1.0×10^4
δ_t	0.000	λ	1 ms	$l_r(l_{min})$	12(3) mm

A sinusoidal pressure pulse is applied to the left free end of the bar, with $P_{load} = 10$ MPa and $t_{load} = 50 \mu s$, as depicted in fig. 3.7. This pulse amplitude is considerably smaller than the materials compressive strength to ensure that the wave is

elastic until tensile failure occurs. Fig. 3.8 shows the distribution of stresses and strain-rate along the bar at different time steps considering a linear-elastic material. When the elastic compression wave reaches the free edge of the bar, reflection occurs and the wave changes signal. During reflection, the compressive and tensile waves compensate each other, and the stresses are momentarily zero at the bar tip region while strain-rates double, up to the point when the tensile wave propagates a certain distance away from the free boundary. In case of a (quasi-)brittle material, failure (spalling) occurs at a specific distance from the free edge (d_{fail} in fig. 3.7) when the (dynamic) tensile strength (f_t^{dyn}) is reached.

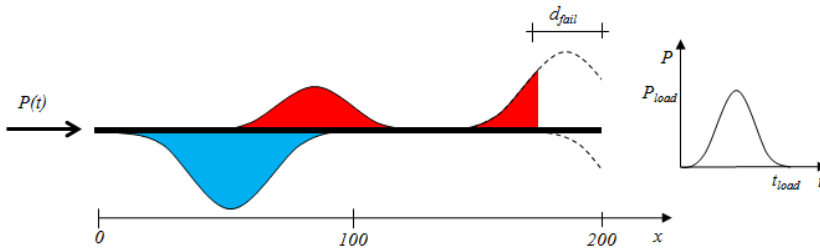


Figure 3.7: Schematic representation of 1D spalling test.

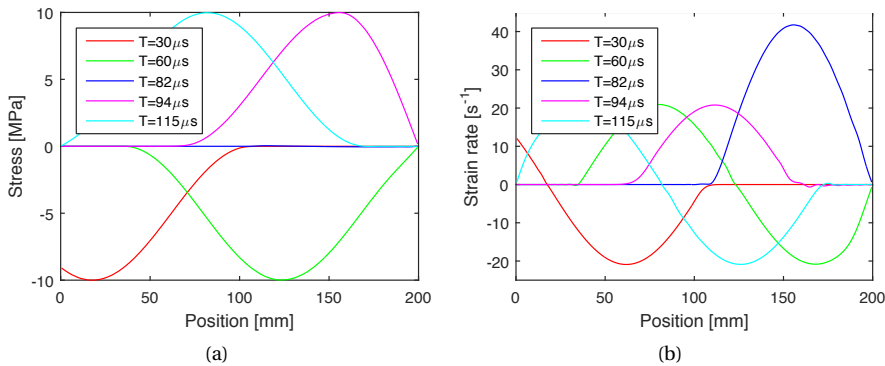


Figure 3.8: Distribution of (a) stresses and (b) strain-rate ($\dot{\epsilon}$) along the bar at different time steps considering a linear-elastic material.

In the following it is discussed how the addition of a material characteristic time (λ) and length (l_r) enhance the proposed constitutive relations in a dynamic tensile situation. This is done by sequentially activating the *effective rate* and stress-based nonlocal regularization in the model, and evaluate the contribution of each of them to the evolution of stresses and damage. Then, a convergence study is conducted to determine the critical computation time step (Δt_{crit}) to ensure the effectiveness of λ and minimize numerical instabilities [105].

3.3.1 NUMERICAL VERIFICATION

LOCAL MODEL IGNORING THE MATERIAL *characteristic time* SCALE

The original rate dependent formulation is recovered by ignoring the material *characteristic time* scale, i.e. considering the local version of the proposed model parameterized according to tab. 3.1 and $\lambda = 0$ ($R = \dot{\epsilon}$). Fig. 3.9 shows the stress evolution at the middle point of the bar ($x = 100$ mm) and the final damage distributions along the bar considering this version of the model. The results are mesh dependent with an unrealistic and irregular damage distribution. Furthermore, the stress wave transferred through the damaged zone is reduced to the level of the static tensile strength of the material ($f_t^{static} = 3$ MPa). This is in clear contradiction to experimental evidence which suggests that failure develops in a relatively narrow fracture process zone and the stress of the transmitted wave is higher than the static strength of the material [71, 101].

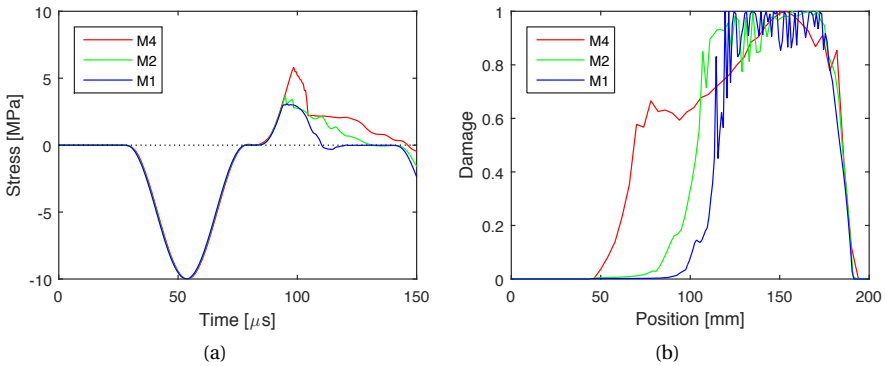


Figure 3.9: Mesh sensitivity of local model considering $\lambda = 0$ ($R = \dot{\epsilon}$) :
 (a) Stress evolution at $x = 100$ mm and (b) final damage profiles.

As it can be perceived by the evolution of stress, damage and strain-rate immediately after damage initiation, depicted in fig. 3.10, that these unrealistic results are the consequence of updating Y_{t0}^{dyn} (eq. 3.10) with $\dot{\epsilon}$. It is fundamental to understand how the variation of material stiffness and strength, respectively controlled by damage and rate, influence the evolution of straining, and vice versa. For simplicity, one may consider that damage starts in one point. This makes it momentarily weaker than the surroundings. This leads to local acceleration of straining, i.e. the strain-rate increases, which enforces a rise of material strength in the following computation time step. Meanwhile, the stiffer surrounding elements exhibit the opposite behavior. This leads to the observed strain-rate oscillations. The consequence is an unnatural evolution of damage where almost all incoming energy is absorbed.

These results lead to question the validity of common phenomenological rules which consider the Dynamic Increase Factor (DIF) depending on an assumed constant strain-rate history to describe the dynamic response of concrete. Apparently, such models tend to underestimate the material dynamic strength and overestimate fracture energy in a spalling situation.

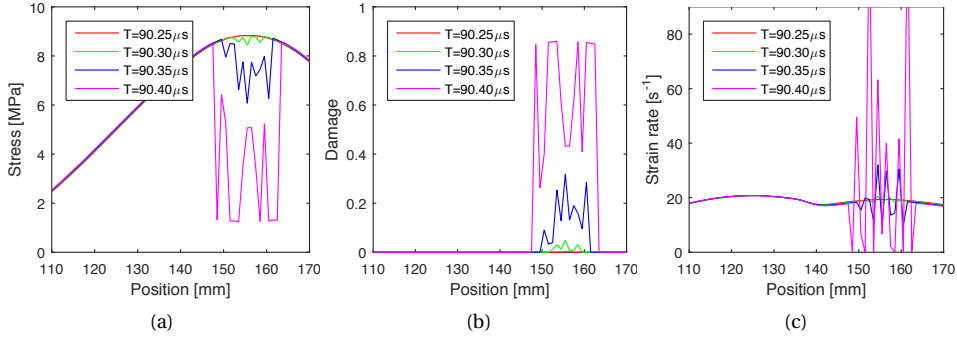


Figure 3.10: Distribution of (a) stresses, (b) damage and (c) strain-rate in the time step ($0.05\mu\text{s}$ intervals) immediately after damage initiation of local model considering $\lambda = 0$ (M1).

LOCAL MODEL CONSIDERING THE MATERIAL *characteristic time SCALE*

The consideration of R in the constitutive law has a weak regularization effect, as evidenced by the evolution of stress at $x = 100$ mm and final damage distribution for the different meshes depicted in fig. 3.11. Although the results remain mesh dependent, they improve considerably. The damage zone width and peak transmitted stress are now independent of mesh refinement. Only the damage distribution alongside with the amount of energy absorbed during failure remains mesh dependent. So, the introduction of a material time scale (λ) in the constitutive law has a weak regularization effect and acts as a localization limiter.

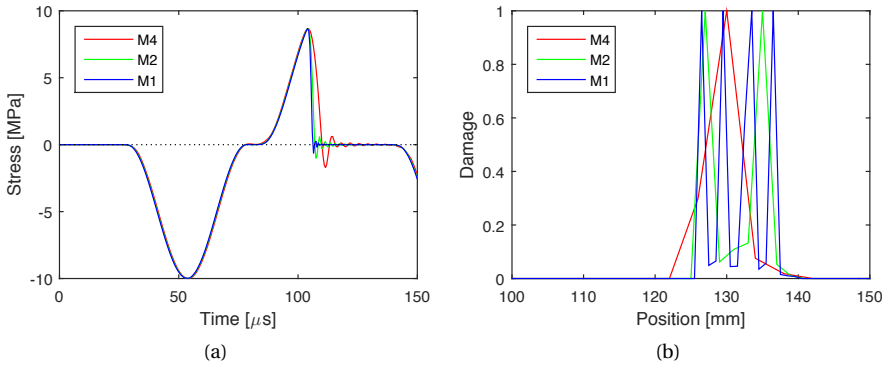


Figure 3.11: Mesh sensitivity of local model considering $\lambda = 1$ ms: (a) Stresses evolution at $x = 100$ mm and (b) final damage profiles.

Unlike the previous example, the maximum transmitted stress is higher than f_t^{stat} . Moreover, the damage zone starts further away from the free boundary. This is due to the restricted evolution of rate by R , in particular R_{down} which keeps the elastic material beyond the damaged zone ($x \approx 140$ mm) stiffer and prevents damage from spreading in

the edge direction (see fig. 3.12). The irregular distribution of damage is interpreted as a consequence of the explicit computation algorithm. Like in the previous example, after damage localization, the material properties tend to oscillate between time steps but, in this case these variations are minimized due to R . The fragmented localization effect visible in the oscillating damage profile is caused by slight strength differences between neighboring elements at the onset of damage.

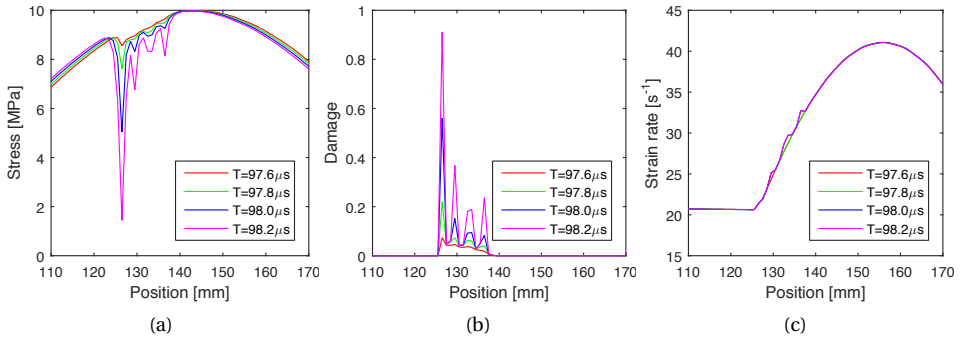


Figure 3.12: Distribution of (a) stresses, (b) damage and (c) *effective rate* in $0.2 \mu\text{s}$ intervals immediately after damage initiation of local model considering $\lambda = 1 \text{ ms}$ (M1).

SBNL MODEL CONSIDERING THE MATERIAL *characteristic time* SCALE

Finally, mesh objectivity is attained by regularizing ε with a stress-based nonlocal (SBNL) scheme, as it can be seen in figs. 3.13 and 3.14. The maximum transmitted stress is apparently not affected by the addition of a length scale (l_r) to the constitutive relations. Only the post peak response is regularized. The evolution of damage is now smooth, even for a relatively coarse mesh (4 mm long elements), which only has 6 elements across the maximum interaction domain ($n_{elements} = 2l_r/l_{element}$).

In summary, these results indicate that the introduction of a material time scale (λ) in the constitutive law, through the *effective rate*, partially works as a localization limiter, similar to what has been observed by Eibl and Schmidt-Hurtienne [35]. Mesh objectivity is only recovered by introducing a material length scale (l_r) in the constitutive law. It was studied and concluded earlier that the stress-based nonlocal model used in this chapter leads to more realistic solutions than a standard nonlocal version of the same model [33].

3.3.2 CONVERGENCE STUDY – DETERMINE Δt_{crit}

A sensitivity study has been conducted to evaluate the numerical stability of the model as function of computational time step (Δt) and characteristic time (λ), considering the SBNL version of the model and the finest mesh (M1). Fig. 3.15 and 3.16 show the stress evolution at $x = 100 \text{ mm}$ and the final damage profile considering different fractions of the critical time step (Δt_{crit}) with fixed λ and vice versa, respectively. Please note that these results only represent a fraction of all possible combinations of Δt between 1% and 60% and λ between 0.01 ms and 10 ms.

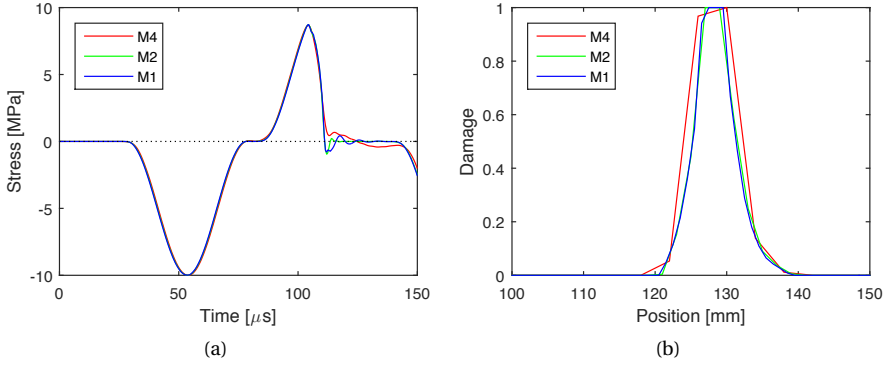


Figure 3.13: Mesh sensitivity of SBNL model considering $\lambda = 1$ ms: (a) Stresses evolution at $x = 100$ mm and (b) final damage profiles.

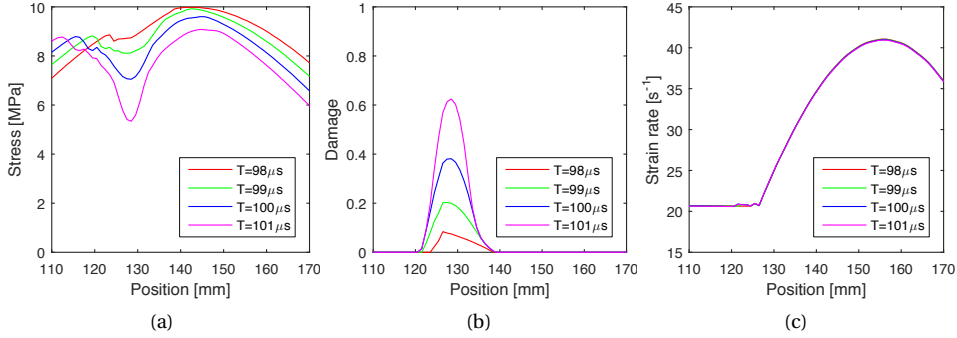


Figure 3.14: Distribution of (a) stresses, (b) damage and (c) *effective rate* after damage initiation of SBNL model ($l_r = 12$ mm and $l_{min} = 1$ mm) considering $\lambda = 1$ ms (M1).

As expected, stability improves with decreasing time step (Δt) and increasing characteristic time (λ). In the present example, numerical stability was found for $\Delta t < 0.1 \Delta t_{crit}$ (with $\Delta t_{crit} \approx 0.28 \mu s$) and $\lambda > 0.5$ ms.¹ It is important to notice that these results only ensure numerical stability for the loading conditions under investigation. The validity of the model can only be evaluated by simulating real experiments with different geometries and loading rates. Only then, it is possible to properly characterize this new material parameter (λ) and evaluate its physical meaning.

¹The computation time step used throughout this study is considerably smaller than the material characteristic time ($\Delta t < 0.001\lambda$). This is critical to ensure the effectiveness of λ and minimize numerical instabilities [105].

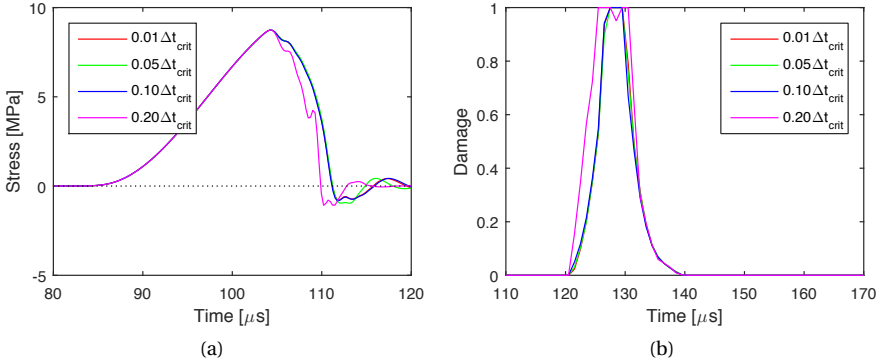


Figure 3.15: Time-step sensitivity for SBNL model considering 1, 5, 10 and 20% of Δt_{crit} and $\lambda = 1$ ms (M1): (a) Stresses evolution at $x = 100$ mm and (b) final damage profile.

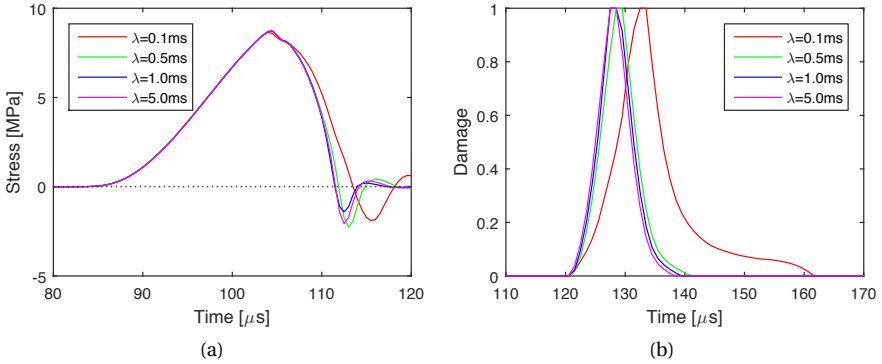


Figure 3.16: Reaction time (λ) sensitivity for SBNL model considering $\Delta t = 0.1 \Delta t_{crit}$ (M1): (a) Stresses evolution at $x = 100$ mm and (b) final damage profile.

3.3.3 EFFECT OF LOADING

The effect of load duration (t_{load}) and amplitude (P_{load}) was also investigated. Fig. 3.17 shows the stress evolution at $x = 100$ mm and the final damage distributions along the bar for loads with the same duration and variable amplitudes with P_{load} between 9 MPa and 11 MPa. This example mimics the experimental effect of impacting the split Hopkinson bar with the same striker at different velocities. As it can be seen in fig. 3.17(b) multiple localization (damage) zones are predicted in the case of the highest pressure load. This phenomenon is consistent with many experimental results with the modified split Hopkinson bar which indicates that dynamic failure of concrete evolves from a single to a multiple macro-crack configuration with increasing load intensity (see for example [101, 104, 106]).

It is interesting to observe that above $P=10$ MPa the transmitted peak stress is almost not affected by the load intensity. Only the absorbed energy increases. To better

understand why this happens, in fig. 3.17(b) the final damage profiles (solid lines) are superimposed to the respective *effective rate* along the bar immediately before damage initiation (dashed lines). So, due to the higher deformation rates registered close to the free edge of the bar in combination with the material reaction time, the material dynamic strength increases significantly in a narrow zone close to the free end between $x = 120$ mm and $x = 160$ mm. Higher pressure loads lead to an initial 'crack' closer to the free edge, in the region where the material is stronger due to the momentarily higher strain-rate in this region. The transmitted wave is then strong enough to force further damage, way from the free edge, where the maximum strain-rates are relatively lower and therefore, the material is weaker. Consequently, a multiple crack pattern occurs.

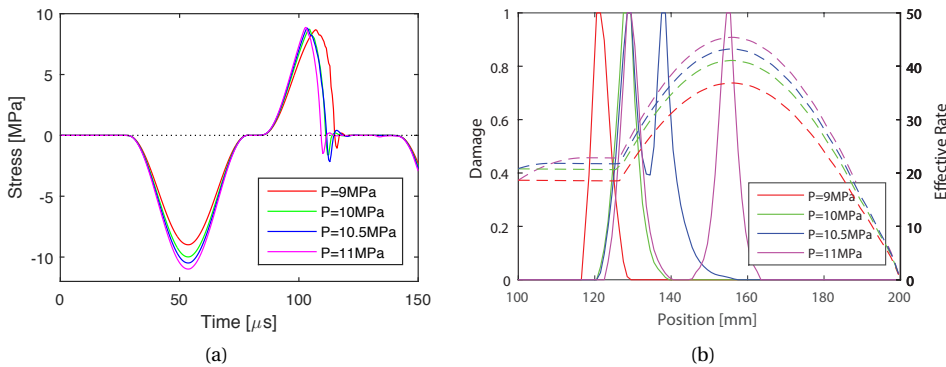


Figure 3.17: (a) Stress evolution at $x = 100$ mm and (b) final damage distributions (solid) and *effective rate* at onset of damage (dashed), for different P_{load} and $t_{load} = 50 \mu s$.

These results suggest that, in a spalling situation, cracking has a higher probability to occur in a region close to the free boundary. The dimensions and location of the damage zones are directly related to the loading wave length and shape. Considering a sinusoidal load with $l = t_{load}/C$, where C is the material sound speed, the potential failure zone extends roughly between $l/2$ and l from the free edge. To the best of the authors knowledge, such relations have never been made for concrete. However, a preliminary analysis of the experimental results available in literature [101, 104, 106] suggests that the fracture process zone tends to expand in the direction of the free edge with increasing load intensity. So, further experimental and numerical investigation is advised to evaluate how the crack pattern and transmitted wave after failure are related to the loading length and magnitude for the same material.

3.4 'EXPERIMENTAL' VALIDATION

3.4.1 MODIFIED SPLIT HOPKINSON BAR TEST - NOTCHED SPECIMEN

An experimental research project at Delft University of Technology has been conducted to characterize the dynamic tensile response of concrete [71]. In this work a Modified

Split Hopkinson Bar (MSHB) was applied to study the material under stress/deformation rates in the order of 1000 GPa/s or 50 s^{-1} . The experimental set-up consists of a 2 m long steel bar and a 300 mm long specimen attached at one edge, both with a 74 mm diameter (see fig. 3.18). A notch was used to enforce the location of failure in the concrete specimen to enable recording directly the deformation of the fracture zone. Several sets of strain gauges (SG1 to SG3) located at the surface of the specimen (see fig. 3.19) were used to measure the longitudinal deformations. Since the incident pulse length, registered at SG1, is shorter than the specimen and the contact between the steel bar and the concrete specimen was lost immediately after loading, there is no need to simulate the complete apparatus. So, only the specimen was modeled and the compression shock wave originally created by a blast and then transmitted to the specimen was simulated by a pressure load uniformly distributed along the specimen end surface as depicted in fig. 3.19. This load was designed in such a way that the strains measured at SG1 coincide with the ones registered in the experimental campaign. Three axisymmetric structured meshes with element sizes of 4 (M4), 2 (M2) and 1 mm (M1) were used in this study.

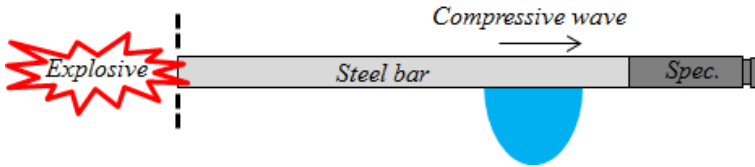


Figure 3.18: Schematic representation of the Modified Split Hopkinson Bar (MSHB) test.

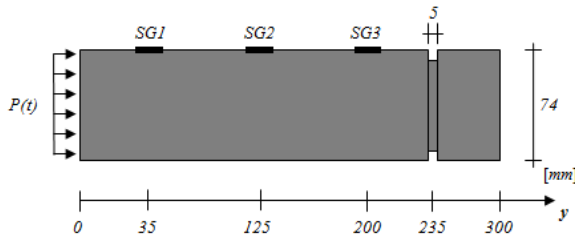


Figure 3.19: Model of the modified split Hopkinson bar test with a notched specimen.

The model parameter set presented in tab. 3.2 is the result of a general calibration procedure based on single element uniaxial simulations, taking into consideration the quasi-static and dynamic properties measured during the experimental campaign. The nonlocal length is usually considered to be a material property related to the theoretical width of the fracture process zone, however its calibration is not trivial. The effect of the nonlocal length in the damage evolution and softening response is discussed in a convergence study later in this section, by considering l_r between 12 and 20 mm. For simplicity, $l_{min} = 1 \text{ mm}$ was fixed for all simulations. The rate parameters considered (ζ_t and η_t) are the ones that provide a close fit to the peak stress measured in the

experimental campaign.

Table 3.2: Constitutive law parametrization – MSHB notched specimen

Symbol	Parameter	Symbol	Parameter	Symbol	Parameter
E	35 GPa	ρ	2400 kg/m ³	ν	0.20
f_t	3.3 MPa	Y_{t0}	f_t/E	A_t	1.0
ζ_t	0.80	η_t	0.30	B_t	1.0×10^4
δ_t	0.045	λ	1 ms	$l_r(l_{min})$	15(1) mm

Although the internal time is presented here as a physical property, it is still to be experimentally quantified. In fig. 3.20 are shown the strain evolution at SG3 considering $\lambda \in [0.0, 1.0]$ ms and the respective final damage profiles, for a 2 mm structured mesh (M2). As it can be seen in the top-right figure, damage spreads unrealistically around the notch when $\lambda = 0.0$. It was observed that in this case, even though nonlocal regularization is used, the results are mesh dependent, comparable to what is observed in fig. 3.9. Since SG3 is located inside the damaged zone, the strain history is not meaningful, and therefore it is not depicted in fig. 3.20(a). This result clearly suggests that a classical rate-dependent formulation does not realistically represent the dynamic behavior of concrete. When the *effective rate* concept is applied, damage immediately concentrates in the notched zone, even with a very small λ . As expected, the results become numerically more stable with increasing values of λ . In this case, results converge for $\lambda > 0.05$ ms. This is in good agreement with Plotzitz et al. [85] and by Haussler-Combe and Panteki [45] who calibrated their *material relaxation time* between 0.05 ms and 1.0 ms for similar loading rates. In order to meet the stability range defined in the previous section, $\lambda = 1.0$ ms is considered in all the following simulations.

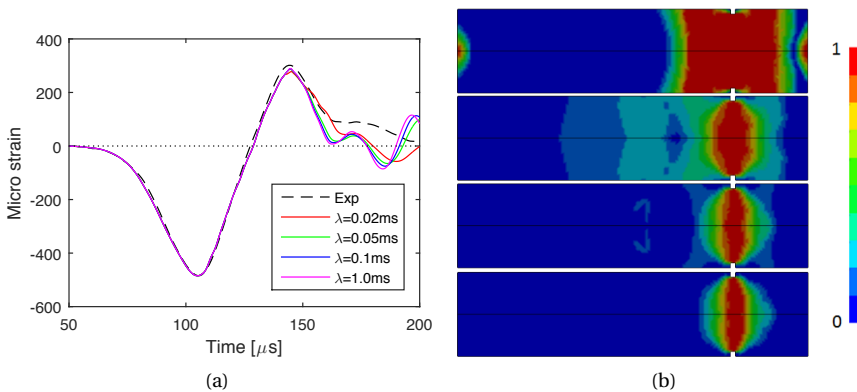


Figure 3.20: Internal time (λ) sensitivity SBNL model ($l_r = 15$ mm and M2).
 (a) Strains at SG3 and (b) final damage profile ($\lambda = 0.0, 0.02, 0.05,$ and 0.1 ms top to bottom).

The results in fig. 3.21 show the strain evolution at SG3 and the final damage distribution for different mesh refinements. The strain histories are compared with the average strains measured at the same positions in the actual test (dashed line). Similar to the one dimensional example, the results are mesh objective. The damage profile is realistic and the peak stress and the first phase of the post peak response are correctly captured. Only the last stages of the strain evolution are still misrepresented.

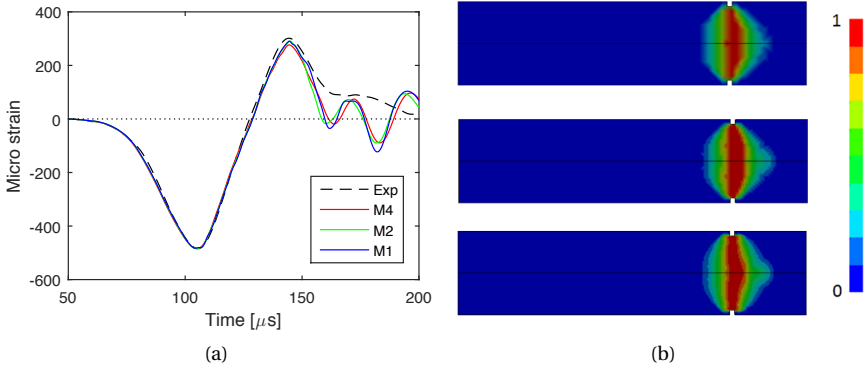


Figure 3.21: Mesh sensitivity SBNL model ($l_r = 15$ mm and $\lambda = 1$ ms).
 (a) Strains at SG3 and (b) final damage profile (M4 top, M2 middle and M1 bottom).

The global dynamic response of the model is a consequence of how energy is absorbed during failure in the FPZ. In continuum mechanics, this means that the global stress-deformation relations are a consequence of the effective strain energy associated with the specific damage (softening) law of the material model and the (nonlocal) interactions between elements [107]. So, a convergence study was conducted to evaluate how these two properties influence the nonlinear response of the material. In fig. 3.22, the strain evolution at SG3 considering (a) a fixed characteristic length (l_r) and variable damage law with rate, by changing parameter δ_t in eq. 3.11, and (b) vice versa, are shown. From the results in fig. 3.22(a) it becomes clear that only changing the peak strength with rate (Y_t^{dyn}), as it is commonly done in rate dependent formulations, is not enough to describe the dynamic nonlinear response of concrete failure. The damage (softening) law, here controlled by B_t^{dyn} (see eqs. 3.5 and 3.11), has to be adapted in order to increase the strain(fracture)-energy with rate. As it is shown in fig. 3.22(b), the post peak response is also affected by changing the nonlocal interaction domain. The post peak response seems to improve with increasing l_r , i.e. by expanding the maximum interaction domain. The peak stress is not affected in this case because a stress-based nonlocal formulation is used.

The simulated results show that the post-peak response in a dynamic situation is governed by both the characteristic length l_r as well as the rate dependent damage law (controlled by δ_t). The peak stress is governed by the evolution of dynamic strength of the material indirectly controlled by the *time* scale (λ) introduced in the definition of rate. These results agree with the findings by Wang et al. [107], who state that the

localization zone width is determined by the minimum of the material length scale (l_r) and the length induced by a material characteristic time scale (λ) in combination with the softening properties of the material. In other words, the dynamic response of the model is governed by the damage law and both *material length* scales, introduced by l_r and λ . Since it is not known to what extent these properties depend on rate, further investigation is needed.

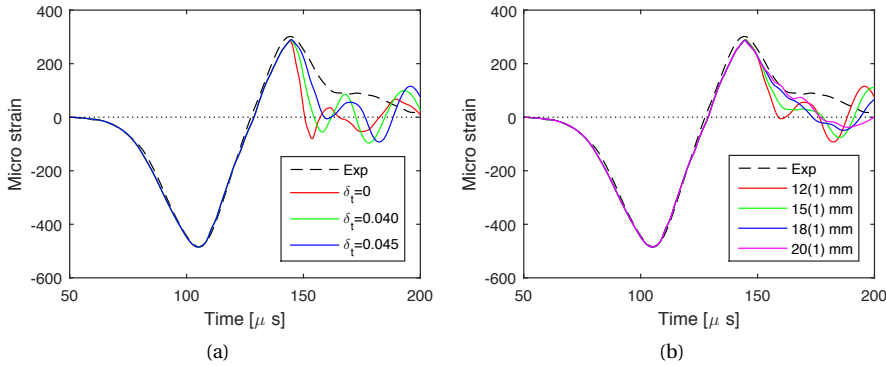


Figure 3.22: Sensitivity study SBNL model (M2 and $\lambda = 1$ ms).
(a) variable δ_t with $l_r = 12$ mm and (b) variable l_r and $\delta_t = 0.045$.

Finally, it is worth noticing that this MSHB test has already been studied in Pereira et al. [33]. The results presented here show a clear improvement (see fig. 18at [33] for comparison). The most evident change can be seen from the damage patterns. In the previous study, damage split into two branches soon after it initiates at the notch. These unrealistic results are directly linked to the damage law considered. Although the biaxial yield/failure envelope of original the Mazars damage model [24] is somehow realistic, it poorly represents the evolution of damage in mixed-mode (tension-compression) stress states.

The introduction of the *effective rate* dependence concept hardly contributes to the observed changes of the damage profiles. As explained in sec. 3.3, this new definition of rate is crucial to control the variation of the material stiffness and strength after damage initiation, while representing the inherent material inertial properties. This problem was circumvented in the previous study by updating the constitutive relations with rate only in the elastic regime. After damage initiation, the constitutive relations were kept unaltered until the end of the simulation.

3.4.2 MODIFIED SPLIT HOPKINSON BAR TEST – UN-NOTCHED SPECIMEN

Multiple cracking in dynamics is a well known phenomenon. This phenomenon is usually captured when un-notched specimens are used in a modified split Hopkinson bar test [101, 104, 106]. Schuler et al. [101], was one of the first to use this configuration to study the dynamic fracture of concrete. They used a classical modified split Hopkinson bar test setup composed of a 60 mm projectile, a 5.5 m long incident bar

and 250 mm specimens, all with 74.2 mm diameter. Three impact velocities, $v_1 = 4.1$ m/s, $v_2 = 7.6$ m/s and $v_3 = 11.1$ m/s, were considered to simulate different loading conditions. They showed that the dynamic failure of concrete evolve from a single to a multiple crack configuration with increasing load velocities.

Like in the previous example, only the specimen was simulated. Considering that only the uniaxial compressive strength is provided, $f_c = 35$ MPa, the tensile properties of the model were calibrated following the *Eurocode 2* [4] recommendations. The nonlocal internal length (l_r) and characteristic time (λ) are the same as the ones used in the previous example. The other dynamic properties (ζ_t , η_t and δ_t) were calibrated in order to have a DIF function identical to *fib's* recommendation [16]. The complete parameterization of the model is summarized in tab. 3.3.

Table 3.3: Constitutive law parametrization – MSHB un-notched specimen

Symbol	Parameter	Symbol	Parameter	Symbol	Parameter
E	38 GPa	ρ	2400 kg/m ³	ν	0.18
f_t	3.2 MPa	Y_{t0}	f_t/E	A_t	1.0
ζ_t	0.80	η_t	0.40	B_t	1.0×10^4
δ_t	0.045	λ	1 ms	$l_r(l_{min})$	15(1) mm

The specimen was modeled with an axisymmetric structured mesh of 2×2 mm² elements. The pressure load transmitted to the specimen as a consequence of the lower impact velocity ($v_1 = 4.1$ m/s) was directly reconstructed from the available data. Since the same projectile was used in all tests, only the load intensity changes with increasing impact velocity. The wave length remains unaltered. So, to simulate an higher impact velocity ($v_2 = 7.6$ m/s and $v_3 = 11.1$ m/s), the same load profile affected by amplification factors was considered. These corrections were obtained by computing the relations between the incident and transmitted stress of an elastic wave hitting normally on a boundary between two media, as described by Meyers [108].

Fig. 3.23 shows the damage profiles for the three loading scenarios investigated, side-by-side to one of the corresponding fragmentation profiles. The simulated fragment lengths are compared with the corresponding experimental results (between brackets). Despite the scarce information available about the concrete mechanical properties, the numerical results agree very well with the experiments. These results corroborate the hypothesis that, the dynamic fracture of concrete is partially dictated by the stress/loading history and the evolution in time of the material dynamic properties, simulated by the proposed damage model. The natural heterogeneity of concrete is the cause for the experimentally observed scattered distribution of cracks.

3.5 CONCLUSIONS

In this chapter it has been demonstrated that common phenomenological rules which consider the Dynamic Increase Factor (DIF) depending on an assumed constant strain-rate history are not adequate to describe the dynamic nature of concrete. A *time* scale should be introduced in the constitutive law in order to describe inherent material

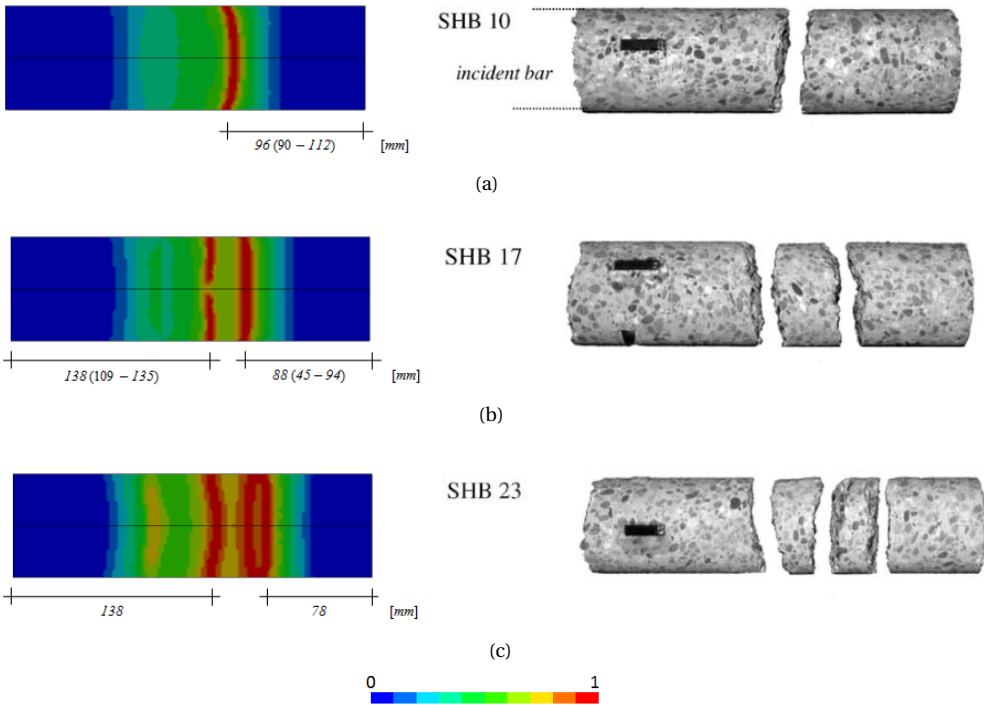


Figure 3.23: Damage and respective fragmentation profiles for:
 (a) $v_1 = 4.1$ m/s, (b) $v_2 = 7.6$ m/s and (c) $v_3 = 11.1$ m/s.

dynamic properties and the history of deformations. It was discussed that, from a macroscopic view point, the dynamic tensile response of concrete is characterized by an apparent resistance to straining associated with a natural viscous behavior of the bulk material; and by a dynamically delayed evolution of damage associated with the retarded crack opening process due to the *Stefan effect* and/or (micro-)inertia effects at the crack tip.

These phenomena were interpreted from the deformation point of view and described by an innovative *effective rate* concept which restricts the evolution of rate by a set of simple rheological models. Instead of the commonly used $\dot{\epsilon}$ (*instantaneous strain-rate*), an *effective rate* (R) is used to update the constitutive law in a classical strain-rate dependent formulation. Additionally, a material length scale is added to the model through a stress-based nonlocal regularization scheme.

It was demonstrated that the dynamic response of the model is governed by the damage law and both the material *length* and *time* scales. The simulated results show that, in dynamic situations, the peak stress is governed by the evolution of dynamic strength of the material indirectly controlled by the *time* scale, here introduced in the definition of *effective rate*, and the post-peak response governed by both the characteristic nonlocal length as well as the rate dependent damage law (effective strain

energy). Furthermore, the addition of a *time* scale in the constitutive relations acts as a localization limiter and provides a weak regularization effect. Nevertheless, mesh objectivity is only recovered with the inclusion of a material length scale, here accomplished by an explicit stress-based nonlocal regularization scheme.

Two sets of modified split Hopkinson bar tests using respectively notched and un-notched specimens were objectively simulated with axisymmetric models. The stress-based nonlocal formulation used in this chapter proved to realistically describe damage initiation and growth in a spalling situation even with relatively coarse meshes. The numerical results with the notch specimen agree very well with experimental data. In the un-notched example, it was possible to represent the phenomenon of multiple fracture zones observed in the experiments, despite the scarce information available about the concrete mechanical properties. These results open new perspectives about the conditions associated with multiple fracture.

4

STUDY OF DYNAMIC CRACK PROPAGATION IN CONCRETE BALANCE BETWEEN TENSILE AND COMPRESSIVE DAMAGE

This chapter presents a numerical study towards the propagation and branching of cracks in quasi-brittle materials, using an extended version of the stress-based nonlocal (SBNL) effective rate-dependent damage model presented in the previous chapter. A new compressive damage mode is added to the formulation in order to have a realistic description of the unconfined behavior of concrete in mode I, mode II and mixed mode loading states. This phenomenological model is mesh objective and reproduces the major phenomena associated with crack propagation and branching in quasi-brittle materials.

It is discussed and demonstrated that the branching phenomenon is not controlled by a specific, material dependent, crack speed. Instead, it is governed by the evolution of the principal stresses at the crack tip, which are controlled by the evolution of damage. It is demonstrated that, with increasing crack speeds, the principal stresses at the crack tip tend to evolve from a mode-I to a mixed-mode state. Beyond a certain (critical) crack speed, the stress distribution around the crack tip reaches a critical state at which a single crack is no longer stable. When this condition is met, crack branching occurs whenever the stress field at the crack tip is destabilized by either a physical discontinuity or an interfering stress wave reflected at the specimen boundaries.

This chapter is based on L. Pereira, J. Weerheijm, and L. Sluys. A numerical study on crack branching in quasi-brittle materials with a new effective rate-dependent nonlocal damage model. *Int. J. Fract.*, 182:689–707, 2017.

4.1 INTRODUCTION

Complex damage mechanisms develop when concrete structures are subjected to dynamic loads. Cracks are the main driver of material failure [109, 110], thus understanding its dynamics is of utmost importance for the design of concrete structures [111], in particular the ones that have to withstand earthquakes, high velocity impacts and explosions.

Although considerable research effort has been devoted to characterize concrete's dynamic behavior, only a few experimental and numerical studies focus on the dynamics of cracks in this material [35, 83, 111–115]. Most of the available knowledge on why a single crack often curves and/or splits into two or more branches at increasing load intensity [116] and deformation rates [113] come from studying brittle materials. For obvious technical reasons, researchers have favored homogeneous transparent materials such as glass, brittle polymers (PMMA) and more recently soft polyacrylamide gels, to conduct these studies. Nonetheless, since the fundamental laws of crack propagation are expected to be universal, the acquired knowledge is prone to be generalizable to heterogeneous materials such as rocks and concrete.

In (quasi)-brittle materials under a mode-I loading condition, a single crack splits into two or more branches when reaching a material dependent critical velocity. However, it has been experimentally reported that, for the same material, branching may occur for a relatively wide range of cracks speeds, depending on the material characteristics, load history, geometry and boundary conditions of the problem [84]. For example, the maximum crack branching velocity observed for concrete falls in a wide interval, between $0.2C_R$ and $0.57C_R$ [111, 113, 117], with C_R being the Rayleigh wave speed. Although we are still far from understanding this complex multiscale phenomenon, it is now accepted that the propagation of cracks is governed by the dynamic evolution of the dissipative processes occurring in the finite fracture process zone (FPZ) [118–120] and the dynamic interaction with the elastic material around the crack tip [121, 122].

It has been consistently observed for different materials that, under mode-I loading conditions, the damaging process ahead of the crack tip changes considerably with increasing crack speeds, as depicted in fig. 4.1. Up to a critical speed of $v_c = 0.3 \sim 0.4C_R$, cracks accelerate very fast leaving behind a nearly smooth crack surfaces (fig. 4.1(a)). Above this limit (v_c), crack acceleration is retarded and the crack surface roughens while the fracture zone progressively evolves from a single discontinuity to an assemblage of small cracks (see for example [123] for images of experimental results). First, micro-cracks and voids tend to grow and coalesce parallel to the forward cracking direction (fig. 4.1(b)). Then, with further increase of the crack speed (and/or load intensity), micro-branches sprout from the crack tip leaving in its wake a rough crack surface (fig. 4.1(c)).

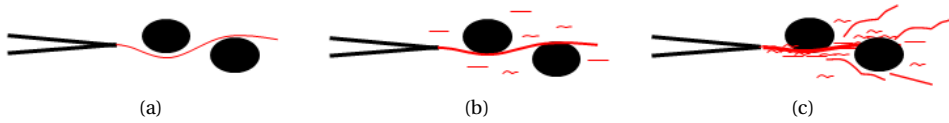


Figure 4.1: Evolution of Fracture Process Zone (FPZ) with increasing crack velocity (adapted from [124]): (a) $v < v_c$, (b) $v \approx v_c$ and (c) $v > v_c$.

Although a single crack becomes intrinsically unstable when $v > v_c$ [120, 125–127], it is not enough to explain why cracks change direction (rotate) or branch. Ravi-Chandar [122] observed that, under equivalent loading conditions, the path and bifurcation of cracks change in time and space as a function of the specimen geometry. He suggested that the evolution of crack is also affected by the interference of the waves bouncing back and forth between the crack and the specimen boundaries. This is the main reason why, in brittle materials, single cracks rarely reach velocities above $0.6C_R$ [122] before dividing into a macroscopic so-called ‘river-delta crack pattern’ [116].

Crack propagation is a complex multiscale phenomenon governed by the initiation, growth and coalescence of micro-cracks and voids [121]. These are time and rate dependent phenomena controlled by inertia effects at the crack tip and the viscous behavior of the bulk material in between cracks. Numerous models have been developed over the years to simulate crack dynamics in brittle materials (for recent reviews, see [109, 120, 128, 129]). Since fracture is an irreversible failure mechanism that starts with the physical debonding of atoms, researchers have been using molecular-dynamic analyses [126, 127, 130] in the hope to unveil its fundamentals. Unfortunately, the size of samples and duration of events modeled are too small to realistically account for the effect of elastic wave interaction with the fracture zone. The inherent material defects caused by (micro) cracks and voids or grain boundaries are also usually not modeled. Thus, although these models provide valuable information about brittle failure dynamics, they do not capture the full multiscale complexity of dynamic fracture of real materials [131].

Micro/meso-scale models are often used to study fracture. It is easily understood that if all the material phases/heterogeneities (aggregates, cement matrix, micro-cracks, voids, etc. in the case of concrete) are explicitly simulated, the known rate effects, such as the increase of fracture energy, the variation of crack patterns (i.e. size of the FPZ) and the retardation of micro-cracking associated to inertia effects at the crack tip, are naturally represented by rate-independent constitutive theories [98, 119, 132, 133]. However, such approaches require very realistic characterizations of the material micro/meso-structure in order to be representative. Thus, these models are not very interesting for engineering purposes because they tend to be cumbersome and computationally expensive.

More successful results have been achieved in the field of continuum mechanics in the finite element method (FEM) framework. The models in this class can be subdivided in two big groups, according to the way cracks are simulated. Eigen-erosion techniques [134], cohesive-zone [135–137] and extended finite element methods (XFEM) [59, 60, 138] simulate cracks as discontinuities created by removing, separating

or splitting elements, respectively. Although it is possible to qualitatively simulate crack dynamics with these methods, each of them faces well-known issues and drawbacks. In all these methods, crack initiation and branching is determined by criteria which have to be defined specifically. The first two methods are pathologically mesh-dependent. XFEM, on the other hand, works around this problem by allowing cracks to ‘cut through’ the finite elements by enabling a local enrichment of approximation spaces through the partition of unity concept. However, in order to do that in 3D, level-set functions are needed to track the crack path, which makes it cumbersome and computationally expensive.

In classical continuous damage or plasticity models, crack initiation, propagation and branching are naturally simulated without needing any *ad hoc* criteria [32]. The major shortcoming of these models, for (quasi-)brittle materials, is their pathological mesh sensitivity. Nonlocal regularization schemes are frequently used to circumvent this problem. Compared to formulations based on energy dissipation regularization (e.g. crack band models [139]) and viscous models [140]), the nonlocal models generally lead to a more realistic representation of the FPZ [61]. In general, nonlocal formulations add a *characteristic length* to the model that defines the influence domain of a integration point over which a meaningful constitutive quantity (strain, energy, etc.) is weight averaged. This suppresses the singularity related issues and leads to mesh objective results. Unfortunately, the standard integral nonlocal [73, 141] and implicit gradient models [74], are prone to some physical inconsistencies [62] in the characterization of crack kinematics in (quasi-)brittle materials. In the urge of solving these issues, multiple nonlocal formulations have been developed recently, as for example the phase-field model [133, 142] and the thick-level set model [143, 144]. These models have shown to reproduce the kinematic of cracks qualitatively well (propagation and branching) in brittle materials. Although conceptually different, these models share a property which is thought to be the key of their success. The damage distribution in space, approaching a discontinuity (*crack*), is of an exponential form instead of the Gaussian (bell like) form observed in standard nonlocal models. Here, the focus is on the recently developed stress-based nonlocal formulation [30, 33, 49].

Generally numerical studies on dynamic crack propagation are validated against tests with a single geometry at one loading or deformation rate. This obviously limits the applicability of these models. Recently, Ozbolt and coworkers [112, 113, 115, 145] broke this trend and conducted a series of experimental and numerical studies on fracture of concrete, where the specimens were subjected to different loading rates. This chapter presents a numerical study towards the propagation and branching of cracks in quasi-brittle materials, using a new *effective rate-dependent* damage model, enhanced by a stress-based nonlocal (SBNL) regularization scheme. After a brief description of the model in the next section (sec. 4.2), two examples are used for its numerical verification and validation. First, an academical example of a single-edge notched tension test (sec. 4.3) is used to compare the proposed formulation with others in literature. For consistency with those, rate effects are ignored in this example. In this section, a sensitivity study is conducted to explore how the material properties (damage law and nonlocal criteria) influence the characterization of the kinematics of cracks. By also studying different geometries and loading histories it is possible to evaluate why

cracks rotate and branch. Finally, in sec. 4.4, a set of dynamic compact tension tests of concrete, recently conducted by Ozbolt et al. [113], are simulated for the numerical validation of the model. In this section, is discussed how the *effective rate-dependent* concept, recently proposed by the authors [34], contributes to a more realistic characterization of the dynamic fracture of concrete.

4.2 CONSTITUTIVE LAW

The damage model developed for this study evolved from the μ *damage model*, recently proposed by Mazars et al. [31]. Rate dependency is accounted for through a recently proposed *effective rate-dependent* formulation [34]. With this concept, the evolution of 'rate' is restricted to account for the delayed response of the material to stress/strain variations due to inherent sub-scale inertia properties of the material. A variable length scale is introduced in the constitutive relation, by an explicit stress-based nonlocal (SBNL) formulation [30, 49], which guarantees an effective and consistent numerical regularization [33]. The model was developed and implemented in LS-DYNA [48].

4.2.1 DAMAGE MODEL

A classical definition of isotropic damage is considered. The stress tensor is expressed as:

$$\sigma = (1 - \omega)\tilde{\sigma} \quad \text{with} \quad \tilde{\sigma} = C : \varepsilon, \quad (4.1)$$

where ε is the strain tensor, C the elastic stiffness tensor and $\tilde{\sigma}$ is the effective stress tensor [102]. The single scalar damage variable ω , which represents the degradation of the material stiffness, results from the combination of the tensile (ω_t) and the compressive (ω_c) damage variables following an adapted version of Lee and Fenves's formulation [36].

$$\omega = 1 - (1 - \omega_t)(1 - \omega_c) \quad (4.2)$$

The evolution of both damage variables is derived from two principal equivalent strain scalar quantities, ε_t and ε_c , which represent the local strain state in tension and compression, respectively

$$\varepsilon_t = \frac{0.5}{1 - 2\nu} I_\varepsilon + \frac{0.5}{1 + \nu} \sqrt{3J_\varepsilon} \quad (4.3)$$

$$\varepsilon_c = \frac{0.2}{1 - 2\nu} I_\varepsilon + \frac{1.2}{1 + \nu} \sqrt{3J_\varepsilon}, \quad (4.4)$$

where ν is the Poisson's ratio, I_ε is the first invariant of the strain tensor and J_ε the second invariant of the deviatoric part of the strain tensor, according to:

$$I_\varepsilon = \varepsilon_1 + \varepsilon_2 + \varepsilon_3,$$

$$J_\varepsilon = \frac{1}{6} [(\varepsilon_1 - \varepsilon_2)^2 + (\varepsilon_2 - \varepsilon_3)^2 + (\varepsilon_3 - \varepsilon_1)^2]$$

The evolution of the nonlinear response is directly related to the growth of two monotonic thermodynamic variables Y_t and Y_c , determined as follows:

$$Y_i(t) = \max[r_i \varepsilon_i, Y_i(\tau), Y_{i0}] \quad \text{for all } t \geq \tau \quad (4.5)$$

where Y_{i0} are the initial damage threshold for tension and compression. The index i in this and the following equations should be interpreted as t for tension and c for compression. The parameters r_i are internal variables derived from the triaxiality factor (r), which provides information on the actual loading state [31, 36].

$$r = \frac{\sum_{I=1}^3 \langle \bar{\sigma}_I \rangle}{\sum_{I=1}^3 |\bar{\sigma}_I|}, \quad (4.6)$$

$$r_t = r^\alpha, \quad (4.7)$$

$$r_c = (1 - r)^\alpha \quad (4.8)$$

where $\langle \bar{\sigma}_I \rangle$ and $|\bar{\sigma}_I|$ are the positive and absolute values of the principal effective stresses. The parameter α controls the ‘amount’ of tensile or compressive straining that contributes to the damage evolution in a traction-compression stress-state. This triaxiality factor varies between 1 and 0 in tension-compression situations, being 1 in tensile and 0 in compressive conditions. Thus, the evolution of r_t and r_c is nonlinear for $\alpha \neq 0$, as it can be seen in fig. 4.2 for $\alpha = 0.1$.

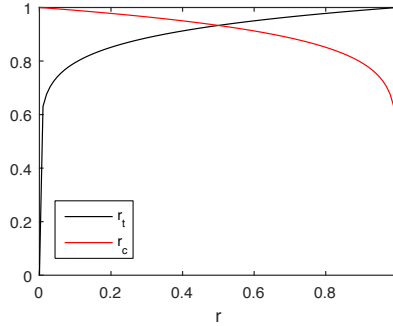


Figure 4.2: Variation of r_t and r_c for $\alpha = 0.1$

The damage evolution laws for tension (ω_t) and compression (ω_c) are of the same type as in the original Mazars model [24].

$$\omega_i = 1 - (1 - A_i) \frac{Y_{i0}}{Y_i} - A_i e^{-B_i(Y_i - Y_{i0})} \quad (4.9)$$

where A_i and B_i are material parameters and Y_{0i} are the equivalent strain damage thresholds. The index i in the equations should again be interpreted as c for compression and t for tension.

In fig. 4.3, the biaxial failure (solid line) and yield (dashed line) envelopes of the model proposed in this study (black lines) are compared to the μ damage model by Mazars et al. [31] (red lines). Both models agree very well with the experimental results by Kupfer et al. [146]. That is not surprising because both models share the same roots.

The main difference between these two models, relies on how the evolution of damage is determined under a tension-compression loading condition. In the earliest model [31], the parameters A_t , A_c , B_t and B_c are weight averaged by a non trivial function dependent on r (eq. 4.6) and a user-defined k to respectively determine the parameters A and B of a single damage law (eq. 4.2). Here, two effective equivalent strains, $\varepsilon_t^* = r_t \varepsilon_t$ and $\varepsilon_c^* = r_c \varepsilon_c$, are determined instead (eq. 4.5). Furthermore, it is important to mention that the strength recovery due to the crack-closure effect is not explicitly considered in this formulation.¹ Although both models produce similar and realistic 2D failure envelopes, in the authors opinion the formulation presented here is considerably simpler. The proposed model is also compared to the modified von Mises model and the original Mazars' model [24] in the appendix of this chapter.

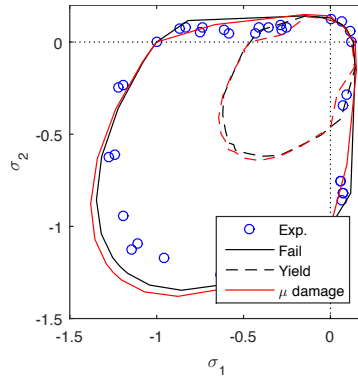


Figure 4.3: Comparison of the biaxial yield (dashed lines) and failure (solid lines) envelopes of the proposed model ($\alpha = 0.1$) and μ damage model ($k = 0.7$) [31] with experimental results [146].

4.2.2 RATE ENHANCEMENT – *Effective rate-dependent* FORMULATION

As it is well known, concrete is a highly rate-dependent material. The effects of rate can be phenomenologically divided into the variation of strength and fracture energy *i*) associated with the change of fracturing process (increase of effective fracture surface) with rate [86, 87] and *ii*) the *reaction time* of the material to stress/strain variations, related to the retardation of cracking due to inertia and the viscous behavior of the bulk material between cracks [35, 64, 85]. The *effective rate* concept recently proposed by the authors [34] accounts for these time dependent phenomena. In this formulation, the material strength and energy is updated as a function of an *effective rate* (R) instead of the *instantaneous* strain-rate ($\dot{\varepsilon}$), as it is commonly done in *hydro-dynamic* modeling. *Effective rate* is a time dependent quantity conditioned by the immediately preceding strain history.

In this concept, it is assumed that the effect of a variation of the strain rate takes some time (λ) to be experienced by the material and becomes effective. The evolution of rate is restricted by the following exponential laws, in case of decrease (R_{down}) or increase

¹The strength recovery due to the crack-closure effect can be easily introduced in the proposed model by simply considering the triaxiality effect (r_t and r_c) in the damage law (eq. 4.2) instead of Y_t (eq. 4.5)

(R_{up}) of the deformation rate (defined as the variation in time of the equivalent strain $\dot{\epsilon}_i$), respectively:

$$R_{down} = \max \left[\dot{\epsilon}_i(\tau) e^{-\frac{t-\tau}{\lambda}}, \dot{\epsilon}_i(t) \right] \quad \text{for all } t \geq \tau \quad (4.10)$$

$$R_{up} = \min \left[\dot{\epsilon}_i(\tau) e^{\frac{t-\tau}{\lambda}}, \dot{\epsilon}_i(t) \right] \quad \text{for all } t \geq \tau \quad \text{and } \omega > 0 \quad (4.11)$$

where λ is a user defined *characteristic time* of the material, t is the current time and τ is the last time that *strain-rate* ($\dot{\epsilon}_i$) was constant. Please note that *effective rate* is independently defined for tension and compression as the variation in time of the respective equivalent strains, i.e. $R_t(\dot{\epsilon}_t)$ and $R_c(\dot{\epsilon}_c)$.

Then, the material strength and strain-energy are updated as in a typical rate-dependent damage formulation. This is done by updating the damage threshold Y_{i0} and the parameter B_i with the *effective rate* (R_i), respectively, in the damage evolution law (eq. 4.9):

$$Y_{i0}^{dyn} = Y_{i0}(1 + \zeta_i R_i^{\eta_i}), \quad (4.12)$$

$$B_i^{dyn} = B_i \left[1 - \delta_i \ln \left(\frac{R_i}{\dot{Y}_0} \right) \right], \quad (4.13)$$

where ζ_i , η_i and δ_i are material constants, defined respectively for tension and compression. The values for increased or decreased loading rates are computed according to eqs. 4.10 and 4.11. The parameter \dot{Y}_0 , represents the rate after which the loading is classified as dynamic. Consistently with the *fib* recommendation [147], $\dot{Y}_0 = 10^{-6} s^{-1}$ is considered. For more information about this model, the reader is referred to the work by Pereira et al. [34].

4.2.3 REGULARIZATION MODEL – STRESS BASED NONLOCAL

To overcome spurious mesh sensitivity, typical for standard ‘local’ damage models, a regularization scheme is needed. In this study, an updated version of the stress-based nonlocal regularization scheme presented by Girya et al. [49] is used. As in any other nonlocal formulation of integral type, the stress response at a material Gauss point (x) is made dependent on its neighbors (ξ) by weight averaging a certain internal variable Z with the interaction domain Ω following eq. 4.14. The nonlocal update of the damage model is simply attained by replacing variable Z by its nonlocal counterpart (\bar{Z}).

In this study, only the equivalent strain under tension is regularized, i.e. $Z = \epsilon_t$. Although both equivalent strains (ϵ_t and ϵ_c) should be independently weight averaged, considering the bi-dissipative nature of the model, it was observed that the results are equivalent in both cases. So, for numerical efficiency, only one nonlocal variable (ϵ_t) was considered.

$$\bar{\epsilon}_t(x) = \frac{\int_{\Omega} \alpha(x, \xi) \epsilon_t(\xi) d\Omega}{\int_{\Omega} \alpha(x, \xi) d\Omega} \quad (4.14)$$

where $\alpha(x, \xi)$ is an arbitrary weight function, here considered to be the Gaussian function:

$$\alpha(x, \xi) = e^{-\left(\frac{2\|x - \xi\|}{l_r}\right)^2} \quad (4.15)$$

where l_r is the characteristic material length.

In a stress-based nonlocal formulation, the influence of the neighboring elements stress state is introduced in the description of the nonlocal interactions by updating the interaction length between the Gauss point x and its neighbors ξ , $l_r = l_{x\xi}$ in eq. 4.15, as follows:

$$l_{x\xi} = \rho(x, \xi) l_r \quad (4.16)$$

with

$$\rho^2(x, \xi) = \frac{1}{(f_t^{dyn})^2 \left(\frac{\sin^2 \varphi \cos^2 \theta}{\langle \sigma_1 \rangle^2} + \frac{\sin^2 \varphi \sin^2 \theta}{\langle \sigma_2 \rangle^2} + \frac{\cos^2 \varphi}{\langle \sigma_3 \rangle^2} \right)} \quad (4.17)$$

where φ and θ are the angles between the eigenvectors of the principal stress tensor σ_I , with $I = 1, 2$ and 3 , at point ξ defined in conventional spherical coordinates system. Considering that $\langle \cdot \rangle$ are the Macaulay brackets, the expression between parentheses is the projection of the positive part of σ_I over the vector $x\xi$, $\langle \sigma_{x\xi} \rangle$. So, $\rho(x, \xi)$ is the ratio between $\langle \sigma_{x\xi} \rangle$ and f_t , which has a value between zero and one for tensile stresses and is equal to zero otherwise. A non zero interaction length must be used to prevent localization to occur in a zone smaller than the finite element, which is impossible and would lead to mesh dependency again. So, the interaction length between two points is allowed to vary between l_r and a minimum length l_{min} . For more information about this model and the computation scheme used for this research, the reader is referred to the works by Girya et al. [30, 49] and Pereira et al. [33, 34].

4.3 SINGLE-EDGE NOTCHED TENSION TEST

In this section, a classical benchmark problem is simulated to assess the numerical performance of the proposed model in predicting crack branching in brittle materials. In the absence of analytical solutions for this problem and poor documentation of the experimental research in literature, a simplified version of a single-edge notched tension test is considered, as recurrently found in literature [128, 129, 135, 144, 148–152]. This example consists of a pre-notched rectangular plate dynamically loaded under tension as represented in fig. 4.4. The traction load ($\sigma = 1.0$ MPa) is suddenly ($\Delta t = 1 \mu s$) applied to the upper and lower boundaries of the sample and held constant throughout the simulation. The problem was modeled under a plane-strain assumption, considering the initial crack as a discrete discontinuity in the geometry.

The material elastic properties considered, $\rho = 2.450$ kg/m³, $E = 32$ GPa and $\nu = 0.2$, are consistent with the properties of glass used in many reference studies, such as: Belytschko et al. [148] (XFEM model); Borden et al. [151] (phase-field model); Moreau et al. [144] (thick-level set model); and Song et al. [128] which did a comparative study including, among others, results of the element deletion method proposed by Ortiz and

Pandolfi [137]. The considered elastic properties lead to longitudinal and Rayleigh wave speeds of $C_p = 3809$ m/s and $C_R = 2119$ m/s, respectively. The remaining parameters of the damage law and nonlocal lengths (see tab. 4.1) were calibrated such that a single branch is observed in the base line example. A brittle material with a tensile strength of $f_t = 6$ MPa is represented. For consistency with the aforementioned studies, rate effects are ignored in this example.

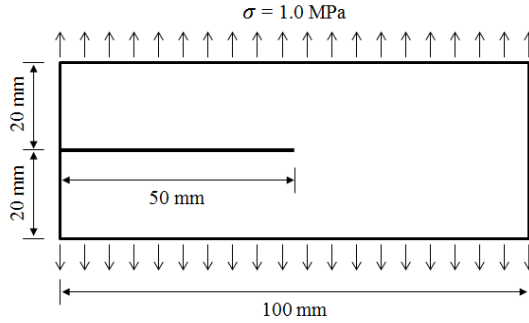


Figure 4.4: Geometry and boundary conditions for the crack branching example.

Table 4.1: Constitutive law parameters

Symbol	Parameter	Symbol	Parameter	Symbol	Parameter
E	32 GPa	Y_{t0}	1.88×10^{-4}	Y_{c0}	8.80×10^{-3}
ρ	2450 kg/m ³	A_c	1.20	A_t	1.0
ν	0.20	B_c	40	B_t	15×10^3
α	0.1	l_r	5 mm	l_{min}	1 mm

The damage profile at the end of the simulation ($t = 50 \mu s$) for different structured meshes of quadrilateral elements with side length between 1.0 mm and 0.4 mm are shown in fig. 4.5. As it can be seen, the expected crack branching phenomenon is qualitatively well captured and the solutions converge upon mesh refinement. It is clear that the meshes of 1 mm and 0.8 mm are too coarse to adequately resolve the nonlocal interactions at the crack tip for the characteristic lengths used in this example, $l_r = 5$ mm and $l_{min} = 1$ mm. Furthermore, as it is typically observed in nonlocal models, too coarse meshes limit the crack tip velocity, which also contributes to the differences in the shape and extension of the damage profile, as it will be shown later. For the remaining of this section only the 0.5 mm mesh is considered because the results do not improve significantly with further mesh refinement from this point forwards and the computation effort is acceptable.

Consistently with experimental observation [84, 110, 116, 123, 153, 154], and the reference numerical studies in literature, the crack grows from the notch to the right and branching occurs at a given position in time and space. However, the reasoning for

this is not completely clear. It is recurrently stated that a crack splits into two or more branches when it travels at a specific, material dependent, critical velocity. However, experimental observations reveal that branching often occurs at different velocities depending on the geometry of the problem [122] and load intensity [155]. So, other reasons than only crack velocity must be behind this phenomenon. As proposed by Ravi-Chandar [84] and as will be shown in the following, crack dynamics is governed by the evolution of the principal stresses around the crack tip. Branching and rotation of cracks are a consequence of instabilities created in the stress fields by stress waves reflected at the distant boundaries or physical discontinuities in front of the crack.

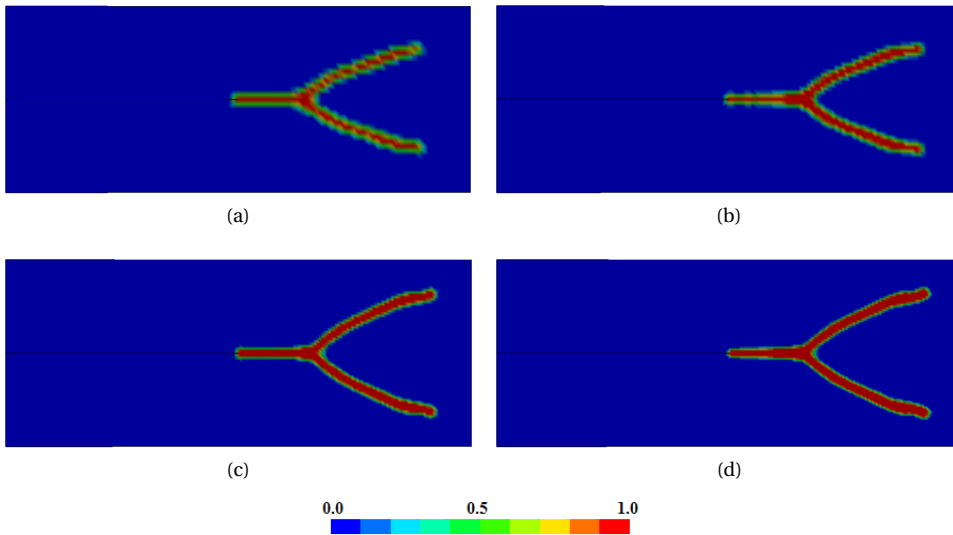


Figure 4.5: Mesh sensitivity analysis. Damage profiles at $t = 50 \mu\text{s}$ for structured meshes of: (a) 1.0 mm; (b) 0.8 mm; (c) 0.5 mm and (d) 0.4 mm

Fig. 4.6 shows some snapshots of the principal stresses at different times, correlated to different positions of the crack tip over the last damage profile at $t = 50 \mu\text{s}$. The results reveal that damage initiation takes place at $t_{crack} \approx 12 \mu\text{s}$, soon after the two initial wave fronts superimpose in the middle of the plate for the first time, at $t \approx 5.2 \mu\text{s}$, when stresses at the notch tip reach the material strength. While the crack accelerates, the principal stress field progressively evolves from a peanut to a clover-like shape, i.e. evolves from pure mode I to mixed-mode (see stress profile at $t = 20 \mu\text{s}$). During the third encounter of the stress waves reflecting at the upper and bottom boundaries, the stress field at the crack tip expands leading to a broadening of damage zone ($t_{branch} = 27 \mu\text{s}$), which ultimately splits into two independent cracks at $t \approx 30 \mu\text{s}$. After branching, the crack path is not straight because the waves reflected at the horizontal and vertical boundaries interact with it in a non-orthogonal way. This leads to asymmetric deformations of the principal stress field which forces the crack to rotate, as it can be seen by the stress distribution in the plate at $t = 45 \mu\text{s}$ (fig. 4.6).

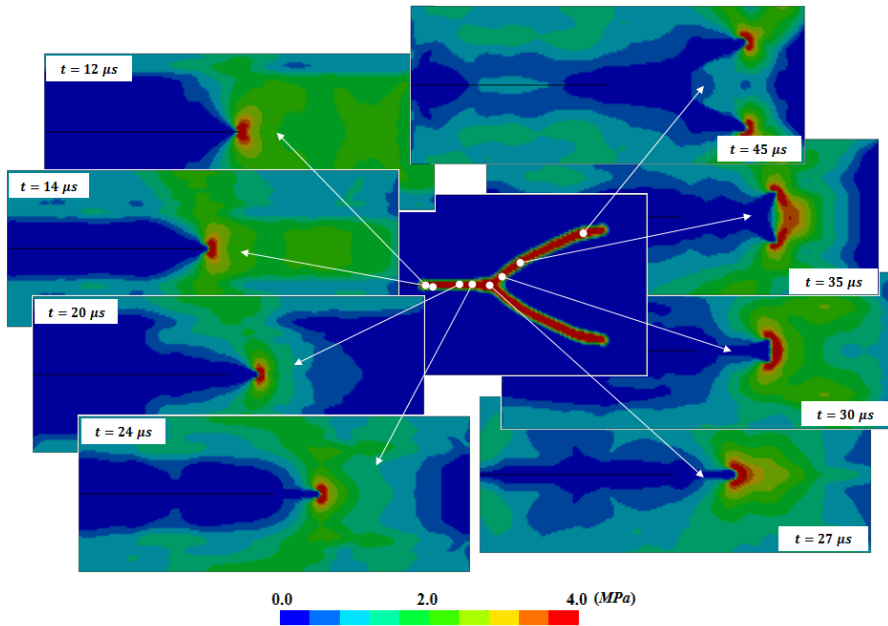


Figure 4.6: Evolution of principal stress and *crack* propagation velocity (damage profile at $t = 50 \mu s$): $t = 12 \mu s$ (immediately after damage initiation); $t = 14 \mu s$; $t = 20 \mu s$; $t = 24 \mu s$; $t = 27 \mu s$ (branching); $t = 30 \mu s$; $t = 35 \mu s$ and $t = 45 \mu s$ (*crack* rotation).

As it can be seen in fig. 4.7, immediately before branching, the principal stress field at the crack tip changes shape and expands considerably when it interacts with the stress waves reflected at the top and bottom boundaries for the third time. Similar distortion occurs when the reflected waves interact with the crack tip for the second time at $t \approx 17 \mu s$. However, the instability created at that time is not strong enough to enforce the bifurcation of damage zones, i.e. to force crack branching.

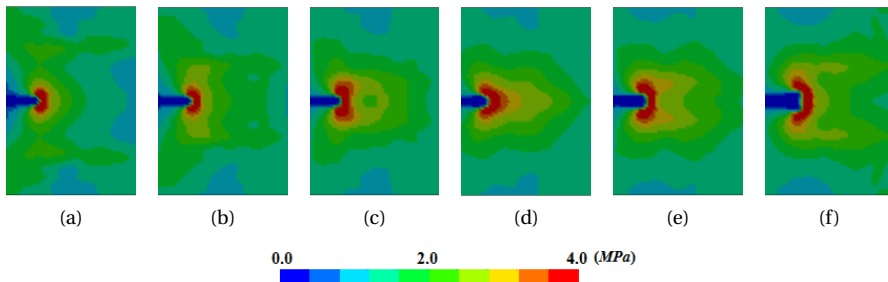


Figure 4.7: Evolution of principal stress during *crack* bifurcation:
 (a) $t = 24 \mu s$; (b) $t = 25 \mu s$; (c) $t = 26 \mu s$; (d) $t = 27 \mu s$; (e) $t = 28 \mu s$; (f) $t = 29 \mu s$.

These results suggest that, with continuous crack growth/acceleration, the principal stress field at the crack tip deforms progressively to a point at which a single crack becomes intrinsically unstable. Only when this condition is met, the interference created by the reflected waves causes the necessary instability that triggers crack branching. Similar observations have recently been made by different authors based on both experimental [120, 154, 156] and theoretical [157] researches. Although they attribute the branching condition to a critical velocity ($v_c \approx 0.3 \sim 0.4$), as it is discussed next, the crack velocity and the stress distribution at the crack tip are interdependent phenomena.

4.3.1 SENSITIVITY ANALYSIS

Motivated by these results and pursuing a realistic representation of crack dynamics, a sensitivity study was conducted to evaluate how the crack path (branching and rotation) and velocity change in time and space considering different geometries, loading histories and material properties.

GEOMETRY

Figs. 4.8 and 4.9 show the final profiles and crack tip velocities at different moments considering different plate widths h_{plate} and notch lengths (l_{notch}), respectively. The simulated crack velocities depicted in each figure were computed by determining the time difference, Δt , needed for two consecutive elements (gauss-points), at a distance ds , along the center line of the damage profile to reach a specific damage threshold ($\omega = 0.5$)².

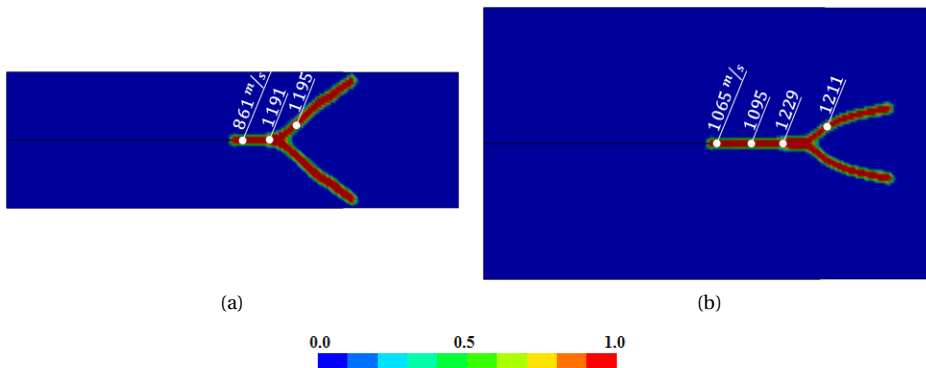


Figure 4.8: Damage profiles considering different plate widths:
(a) $h_{plate} = 30$ mm at $t = 40 \mu s$, and (b) $h_{plate} = 60$ mm at $t = 50 \mu s$.

As it can be seen, the evolution of the *crack* velocity is not significantly affected by the changes in the geometry. Only the moment of branching and the post branching profiles somewhat differ. The change of notch length has little to no effect on the moment of

²It was observed that, for the examples in this section, the computed are virtually the same independently of the chosen damage threshold between 0.3 and 0.7

branching ($t \approx 27 \mu\text{s}$). The time until branching is only affected by the plate width, with the bifurcation of damage occurring at $t \approx 22 \mu\text{s}$ for $h_{plate} = 30 \text{ mm}$ and $t \approx 32 \mu\text{s}$ for $h_{plate} = 60 \text{ mm}$. As it has been explained before in fig. 4.6, the principal stress field at the crack tip tends to twist, expand and/or contract every time it interacts with the waves reflected at the free boundaries, shaping in its wake the evolution of damage. So, when the plate width is reduced, the waves reflected at the top and bottom edges interact more frequently with the *cracks* tip, triggering branching sooner. The influence of the right hand side boundary only becomes relevant after branching, when *cracks* move at an angle. Now the wave reflected at the free edges distort the stress field at the *crack* tips forcing them to rotate.

4

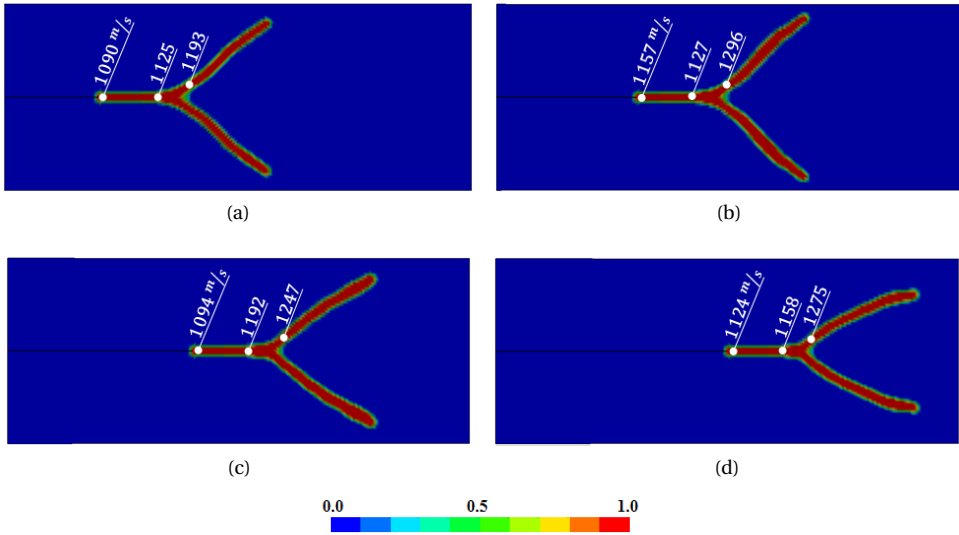


Figure 4.9: Damage profiles at $t = 50 \mu\text{s}$ considering different notch lengths: (a) $l_{notch} = 20 \text{ mm}$, (b) $l_{notch} = 30 \text{ mm}$; (c) $l_{notch} = 40 \text{ mm}$ and (d) $l_{notch} = 50 \text{ mm}$.

LOAD INTENSITY

The effects of considering different load intensities are depicted in fig. 4.10. Consistent with experimental observations (see for example fig. 1 in Bowden et al. [155]), with increasing load intensity, the final crack pattern evolves from a single crack to a river-delta like profile with the first branching occurring earlier in time and space. It is observed that, by reducing the applied load to $\sigma = 0.5 \text{ MPa}$, the crack initiation and branching occur considerably later than before, $T_{crack} \approx 27 \mu\text{s}$ and $t_{branch} = 49 \mu\text{s}$, and the post branching cracks are nearly straight (compare fig. 4.10(a) with fig. 4.9(d)). This relatively weak loading leads to a significant slower damage evolution manifested by the observed decrease of the average and maximum crack speeds before branching. Consequently, the stress field at the *crack* tip does not expand as much as before and it takes longer to evolve to a *critical* mixed-mode state, thus leading to later branching.

Another consequence of this decrease of the loading intensity is a weaker stress wave bouncing back and forth in the specimen, resulting in relatively small stress instabilities when interacting with the crack tip, hardly affecting the crack trajectory.

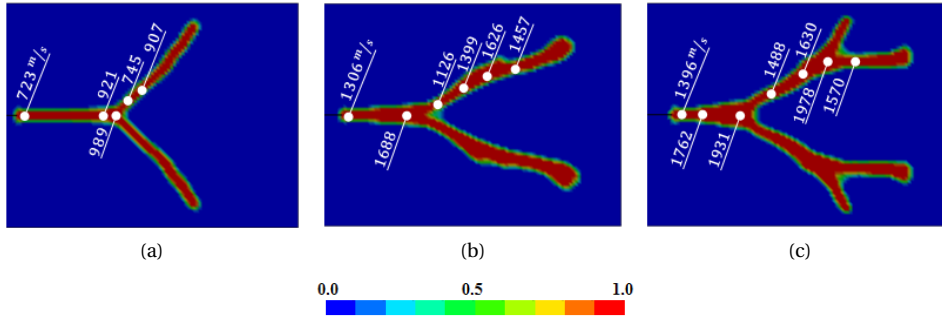


Figure 4.10: Influence of load intensity in the crack dynamics ($l_{notch} = 50$ mm), considering: (a) $\sigma = 0.5$ MPa (at $t = 80 \mu\text{s}$); (b) $\sigma = 1.5$ MPa (at $t = 40 \mu\text{s}$) and (c) $\sigma = 2.0$ MPa (at $t = 35 \mu\text{s}$).

The consequences of increasing the load intensity, as it can be seen in fig. 4.10(b) for $\sigma = 1.5$ MPa and fig. 4.10(c) for $\sigma = 2.0$ MPa, are an overall acceleration of the cracking process. Opposite to the previous case, the stress field at the *crack* tip evolves faster to a *critical* mixed-mode state and the stress wave bouncing in the specimen is intensified. This results in stronger instabilities which ultimately generates multiple branching (fig. 4.10(c)) instead of crack rotation, as it is observed in the reference example (fig. 4.5). In the intermediate loading case, presented in fig. 4.10(b), although the branching process starts, it is blocked because the stress instability is not strong enough. This is marked by a *crack* speed drop after a broadening of the damage profile and a slight rotation of the crack. The general broadening of the damage profile, particularly visible before branching, is a direct consequence of the expansion of the principal stress field at the crack tip. This may be related to the experimentally observed enlargement of the FPZ, as proposed by Bobaru and Zhang [129]. For example, the experimental results reported by Ramulu and Kobayashi (fig. 1) [116] and Fineberg and Marden [123] show that the crack surface roughens prior to branching while micro-branches sprout from the crack tip and the crack progressively evolves from a single macro-crack to an assemblage of micro-cracks. It has also been observed that the size and number of micro-branches tend to increase with the crack velocity [110] leading to an overall enlargement of the FPZ and increase of the dissipated fracture energy.

It is worth noticing that the average and maximum *crack* velocities tend to increase proportionally to the loading intensity. Although an increase is expected, the simulated results are only realistic for the lower intensity loading conditions, in fig. 4.10(a). In the other cases, in figs. 4.10(b) and (c), both the acceleration and top velocities of the crack are high compared to what is commonly observed in quasi-brittle materials like glass. Experimental results suggest that the crack acceleration decreases above a certain critical crack speed ($v_c = 0.3 \sim 0.4C_R = 636 \sim 848$ m/s) [124]. Furthermore, after

branching, the new cracks should have an initial velocity 10 ~ 20% lower than the original one and accelerate thereafter until the branching processes eventually repeat itself. As it is explored next, these discrepancies between simulation and experiments can be minimized by updating the constitutive relations (material model properties) as a function of the loading scenario.

DAMAGE LAW

In all the reference studies mentioned above, the authors focused their attention on showing how their numerical techniques improve with respect to others in representing the dynamic propagation of cracks. Little to no attention is paid to how the underlying constitutive relations influence the overall response of the model. Nevertheless, it is crucial to explore the applicability of a new numerical technique and assess how it can be used to simulate different materials under different loading conditions. To this end, the influence of using different damage laws and nonlocal criteria were investigated. In appendix A are also presented results obtained considering two damage models widely used in literature: the modified von Mises and the original Mazars' model [24].

The effect of the damage law on the model response was first evaluated by only changing B_t in eq. 4.9 (see fig. 4.11). This alters the post peak (softening) response and the effective strain energy (area under the stress-strain curve) of the model. By making the model more ductile, i.e. using a small B_t , the evolution of damage slows down which leads to a decrease of the crack propagation speed and a slight spreading of the damage profile. Although the evolution of the principal stresses at the crack tip is also affected by this alteration of the damage law, branching starts approximately at the same time in all cases ($t \approx 27 \mu s$). Since the cracks propagate at different speeds, the waves reflected at the specimen boundaries interact with their tips at different positions in space (and time). This leads to considerable changes in the overall crack path, regarding the position, the angle and the extension of the branching process zone. The rotation of the branching cracks is also affected for the same reasons.

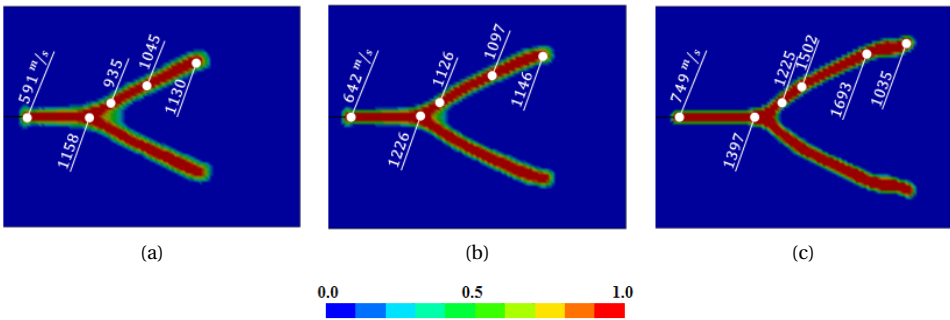


Figure 4.11: Influence of damage evolution law in the crack dynamics considering variable B_t eq. 4.9 ($t = 50 \mu s$): (a) $B_t = 8 \times 10^3$ ('ductile'); (b) $B_t = 10 \times 10^3$ and (c) $B_t = 20 \times 10^3$ ('brittle').

The consequences of considering different nonlocal definitions with the same constitutive law are shown in fig. 4.12. The increase of l_{min} in the stress-based nonlocal

formulation has a direct impact on the width of the damage band. The ‘fracture energy’, i.e. the energy consumed per unit crack length, increases with the expansion of the nonlocal interaction domain. Like in the previous example (fig. 4.11), this leads to a decrease of the average *crack* velocity which consequently alters the crack evolution. It was also observed that the instantaneous *crack* speed fluctuates every time a wave reflected by the specimen boundaries interacts with the stress field at the *crack* tip. The rapid acceleration and deceleration of the moving crack is a direct consequence of the extension and contraction of the principal stresses at the crack tip, as depicted in fig. 4.7. These effects are enhanced by using larger overall interaction domains, as it is observed in the standard nonlocal model presented in fig. 4.12(c).

From these results, it is possible to conclude that crack path and speed evolutions are controlled by the evolution of damage at the crack tip, which in this particular case is governed by both the damage law (eq. 4.9) and the nonlocal criteria. So, in order to minimize the discrepancies between simulation and experiments registered in the previous subsection (sec. 4.3.1), one has to increase the model fracture energy proportionally to the load intensity. As it will be shown later in sec. 4.4, this can be achieved by considering a strain rate-dependent formulation.

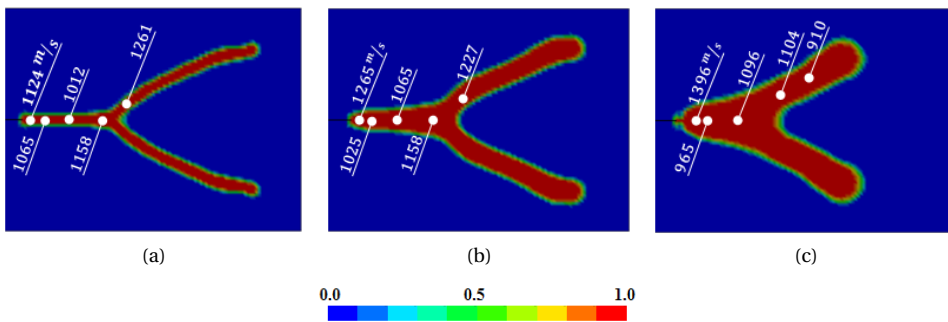


Figure 4.12: Influence of nonlocal definition in the *crack* dynamics ($t = 50 \mu s$). SBNL model considering $l_r = 5 \text{ mm}$ and variable l_{min} : (a) $l_r = 1 \text{ mm}$; (b) $l_r = 3 \text{ mm}$ and (c) $l_r = 5 \text{ mm}$ (standard nonlocal).

4.3.2 RESULTS ANALYSIS – WHAT MAKES CRACKS ROTATE AND BRANCH?

Although the model used in this study is a phenomenological model, it helps us to shed some light on why a straight crack tends to rotate and branch. The results corroborate Ravi-Chandar’s [84] observations stating that, under dynamic loading conditions, the evolution and bifurcation of cracks is influenced by both the load history and the geometry of the problem (boundary conditions). It was established that the development of a single crack and its branching is determined by the dynamic evolution of the fracture process zone (FPZ) and the evolution of the principal stress field at the crack tip, as schematically represented in fig. 4.13.

As it is well known, stress evolution in time and space are controlled by waves, and waves cannot propagate infinitely fast. Upon damage evolution, the material

impedance decreases, so does the wave velocity. Consequently, waves in the fracture process zone and the surrounding elastic material propagate at different speeds which leads to the distortion of the stress field around the crack tip [158]. So, with increasing crack propagation speed, stresses start to 'pile up' in front of the crack tip and the principal stress distribution evolves from a pure mode-I stress state (peanut-like shape), as depicted in fig. 4.13(a), to a mixed-mode stress state (fig. 4.13(b)). If the crack continues to accelerate, the principal stress field at the crack tip deforms further and evolves into a clover-like shape (fig. 4.13(c)), until it reaches a critical state which favors damage development away from (parallel to) the forward cracking direction.

A single crack is no longer stable and crack branching occurs whenever the stress field at the crack tip is destabilized by a sufficiently strong instability (fig. 4.13(c)), created by the interference of a bouncing stress wave or a physical discontinuity [119, 120, 154]. The rate at which the principal stresses evolve can be directly related to the crack tip velocity, which by its turn is governed by the loading intensity (rate of straining) and the material properties. Furthermore, the expansion of the FPZ and change of the fracturing processes, registered experimentally when a crack travels above a critical speed, is here represented by the broadening of the damage profile, which is observed whenever the critical stress state is reached.

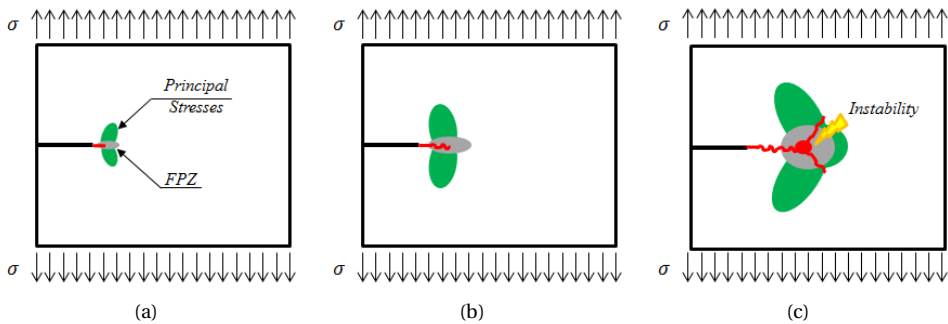


Figure 4.13: Schematic evolution of stress field and FPZ at the crack tip of a brittle material considering uniform tensile stressing (σ): (a) $v < v_c$; (b) $v \approx v_c$ and (c) $v > v_c$.

It was established that the model used until now can qualitatively well represent the dynamics of cracks in (rate independent) brittle materials. The results presented are in good agreement with others in literature. However, even though this is an academic example, the predicted crack velocities seem to be high for a glass like material. This is because, in this and the other studies, strain-rate effects which are characteristic for quasi-brittle materials, are not included. In the next section, a set of experiments conducted with concrete is simulated with an *effective rate-dependent* version of the proposed model. This formulation describes the increase of fracture energy, strength and micro-inertia effects, associated with the change of the fracturing process with increasing crack velocities (strain-rates), as described in the introduction.

4.4 COMPACT TENSION TEST IN CONCRETE

Although studies on dynamic cracking (fracture) are abundant in literature, only a few are dedicated to study this phenomenon in quasi-brittle heterogeneous materials such as concrete. Recently, Ozbolt and coworkers conducted two sets of studies, both numerical and experimental, specially designed to study crack branching in plain concrete [112, 113, 115, 145]. The influence of loading rate on the response of compact tension (CT) specimens and L-specimens of normal strength concrete was investigated. The test results of the CT tests [113] are used as a reference in this study (see fig. 4.14).

Plain concrete ($f_c = 53 \text{ MPa}$) CT specimens ($200 \times 200 \times 25 \text{ mm}$) were tested at different loading rates ranging from 0.06 to 4.3 m/s. The displacement controlled loads were applied at the surface of the right edge of the notch, while the left edge was fixed (see fig. 4.14). In the experimental study several sensors were used to accurately record, besides the final crack patterns, the crack propagation velocities, reaction forces and displacement at the notch.

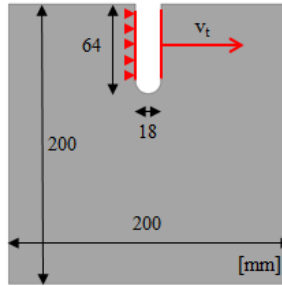


Figure 4.14: Schematic representation of CT test.

4.4.1 MODEL DESCRIPTION AND CALIBRATION

The experiments were simulated with the LS-DYNA finite element code, using a Lagrangian explicit algorithm. Two structured meshes of plane-strain quadrilateral elements with 2 mm (M2) and 1 mm (M1) characteristic element size were used to model the specimens. Displacement controlled loads, similar to the experimentally measured deformation rates, were applied to one edge of the specimen's notch, while the other edge was fixed. No information is given in the experimental paper [113] about the actual load history. So, in our simulations an acceleration step of $100 \mu\text{s}$ was considered before reaching the constant deformation rate, in order to have a realistic loading. The quasi-static properties determined during the experimental campaign [113] were used for the basic calibration of the model (tab. 4.2).

Since there is no direct relation between fracture energy (G_F) and strain energy in nonlocal damage mechanics, the shape of the softening law (eq. 4.9) was calibrated considering the average behavior of plain concrete. The parameters in the rate dependent law (ζ , η and δ) were calibrated to fit the modified dynamic increase factor (DIF) law proposed by Malvar and Ross [80]. The maximum nonlocal intrinsic lengths were set as $l_r = 12 \text{ mm}$ and l_{min} equal to the minimum mesh size. The calibration of

these parameters is not a trivial task and therefore not discussed in this chapter. Nevertheless, it is worth noticing that these parameters ensure the desirable numerical stability of the model [49]; and lead to an effective fracture process zone width of approximately three to five times the maximum aggregate size, with a 'localized' profile around the most damage areas, which is in good agreement the experimental observations [139]. Finally, since an explicit computation scheme is used, a sensitivity study was conducted to determine the minimum computation time-step needed to ensure numerical stability. It was determined that a step size which is 30% (used in this study) or less of the critical time-step is necessary.

Table 4.2: Constitutive law parameters

Symbol	Parameter	Symbol	Parameter	Symbol	Parameter
E	36 GPa	Y_{t0}	1.06×10^{-4}	ζ_t	0.80
ρ	2400 kg/m ³	A_t / B_t	1.0 / 1.0×10^4	η_t	0.30
ν	0.18	Y_{0c}	8.0×10^{-4}	δ_t	0.045
α	0.1	A_c / B_c	1.65 / 430	λ	1.0 ms

4.4.2 RESULTS AND DISCUSSION

In fig. 4.15 the simulated damage profiles considering the 2 mm and 1 mm structured meshes, M2 and M1 respectively, are given together with the experimentally observed crack patterns. The maximum reaction forces, registered at the fixed edge of the compact tension specimen's notch, are summarized in table 4.3. The crack propagation velocities, determined for $\omega = 0.4$ (left) and $\omega = 0.6$ (right), in the 4.3 m/s example are presented in fig. 4.16 together with to the respective damage profiles.

Table 4.3: Summary of reaction force for different loading velocities

Load (m/s)	Max reaction(kN)		
	Test	M2	M1
0.5	4.05	4.20	4.20
1.4	4.64 - 5.76	4.42	4.28
3.3	4.59 - 6.88	5.64	5.62
4.3	5.66	5.80	5.66

Overall, the simulations are objective and agree very well with the experimental results. The dominant dynamic fracture phenomena in concrete are well represented by the proposed damage model. Consistent with the experimental data, the predicted crack patterns and reaction forces change with loading rate. For loading with a relatively low displacement rate (0.5 m/s) damage develops almost perpendicular to the loading direction at relative low propagation speeds. With increasing deformation rates, the damage process accelerates (i.e. crack speed increases) and starts to develop under an inclined angle. In both, simulations and experiments, crack branching is first

observed at a displacement rate of 3.3 m/s. Branching occurs in a region where the damage (*crack*) propagation speed is the highest. During branching, the *crack* speed drops approximate 20% and the damage zone thickens slightly. As suggested by different authors (see for example [32, 150]) and mentioned in the previous section (sec. 4.3), these phenomena may be correlated to the experimentally observed expansion of the FPZ and roughening of the crack before branching associated with a significant change of the fracturing process when a critical stress state is formed at the crack tip.

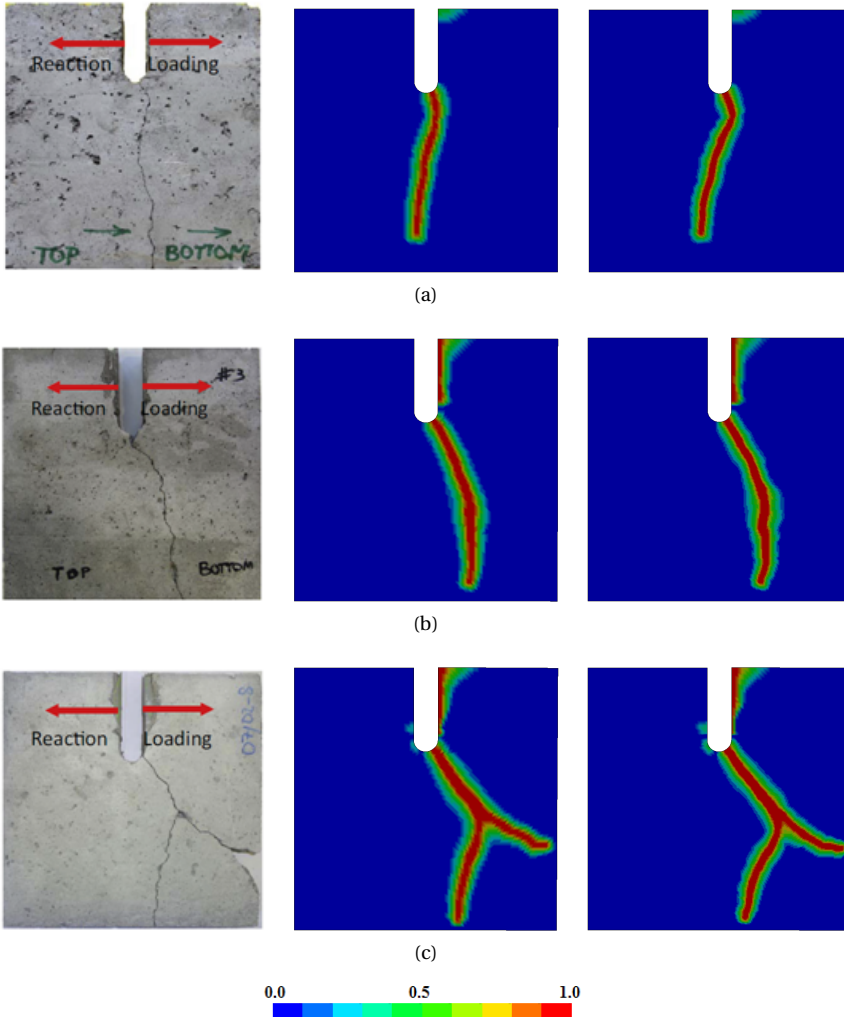


Figure 4.15: Comparison between experimentally observed crack patterns (left) and final damage profiles (M2 – center and M1 – right) for different loads: (a) 0.5 m/s; (b) 1.4 m/s and (c) 3.3 m/s.

Although the maximum predicted crack speed is higher than the experimentally observed speed before branching, the predictions at the initial stages of cracking are identical (see fig. 4.16). It is worth noticing that, according to a recent study by Forquin [111], most experimental methods are not accurate enough and tend to underestimate crack propagation speeds in concrete. Thus, caution is advised on using the crack speed for validation. Crack patterns could be better used instead.

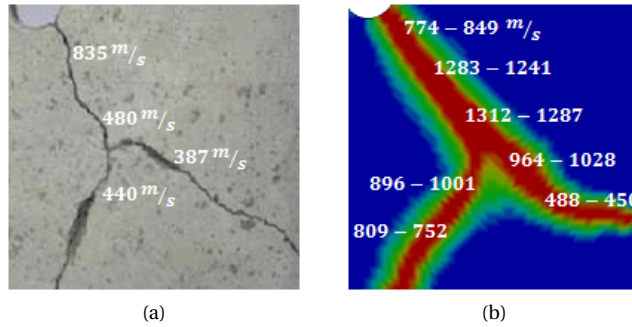


Figure 4.16: Crack speed and final damage profile for 4.3 m/s load.

Fig. 4.17 shows the evolution of the principal stresses for different loads, $\nu = 1.4$ m/s (fig. 4.17(a)) and $\nu = 3.3$ m/s (fig. 4.17(b)). As in the previous section, the principal stress field evolve in time from a peanut-like shape (mode-I), in the beginning of the failure process, to a clover-like shape (mixed-mode) at crack branching (fig. 4.17(b)). In the lower loading rate example (fig. 4.17(a)), the distortion of the stress field at the crack is not severe enough to force the crack to split when it is destabilized by the stress waves reflected at the boundaries of the specimen. In either case, the curvature of the cracks is a consequence of the asymmetric evolution of the stress field at the crack tip due to the specimen's geometry (boundary conditions). It is worth noticing that the evolution of the crack velocity is directly related to the rate of change of the stress distribution and intensity at the crack tip. This is governed by the evolution of damage ahead of the crack tip and the stress waves bouncing back and forward between the crack and the boundaries of the specimen, which is consistent with the observations made in sec. 4.3.

4.4.3 EFFECT OF RATE ENHANCEMENT FORMULATION

Although rate enhancement of the constitutive relations is necessary for a realistic representation of concrete's dynamic behavior, it is not yet clear to what extent. In fig. 4.18, the final damage profiles for $\nu = 0.5$ m/s are shown considering different formulation to describe rate dependence. Three results are presented, representing the evolution stages of the formulation proposed in this chapter: (a) rate independent model; (b) classical strain-rate dependent model ($\lambda = 0$); and (c) *effective rate-dependent* model. As it can be seen in fig. 4.18(a), when rate effects are ignored, *crack* branching occurs even at the lowest loading velocity. Since strength and strain-energy are not updated with rate, the material model is weaker than in reality. Consequently, as explained in the previous section (sec. 4.3), cracks accelerate faster

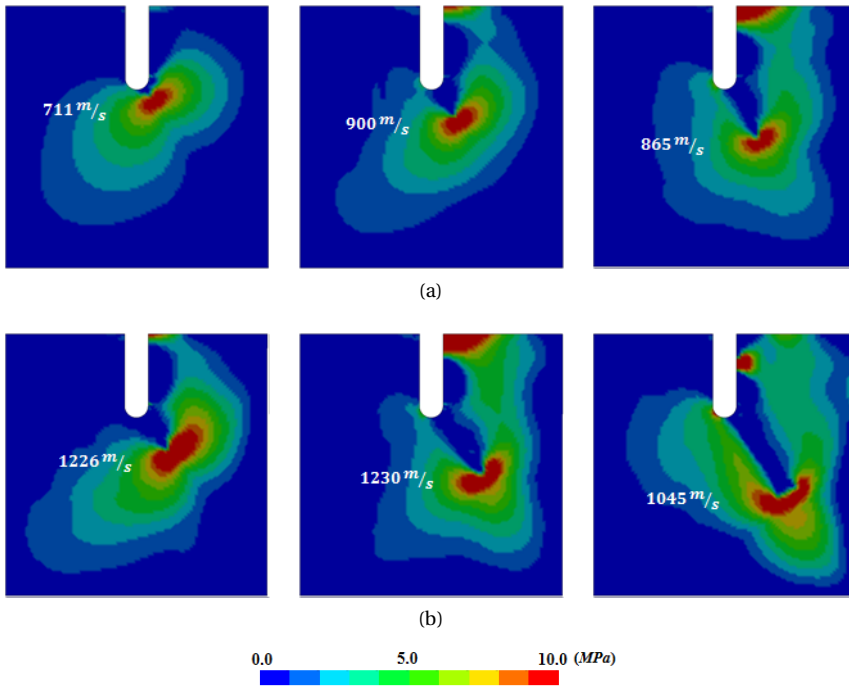


Figure 4.17: Evolution of principal stresses ($t = 80, 100$ and $120 \mu\text{s}$) and crack speeds computed for $\omega = 0.5$ for different loads: (a) $v = 1.4 \text{ m/s}$ and (b) $v = 3.3 \text{ m/s}$.

and the principal stresses at the crack tip reach their critical state sooner, leading to premature branching.

When the inertia effects at the material level, here represented by the *characteristic time* scale λ , are ignored, cracking is also misrepresented, as it can be seen in fig. 4.18(b). By ignoring the time that a material needs to adapt to a variation of straining (λ), the evolution of the material strength is not smooth, which leads to non realistic variations of the material strength at the crack tip. In this case, due to the material stiffness degradation after damage initiation, locally the strain rate ($\dot{\epsilon}$) increases abruptly. Since the constitutive relations are updated every time step as a function of this 'instantaneous' rate, the damaged material tends to become stiffer than its surroundings. This forces a strain rate to decrease and so the material stiffens. The result is a continuous variation of the material properties which leads to an excessive damage development and, although it is not shown here, mesh dependent results. As it can be seen in fig. 4.18(c) realistic results are obtained when the proposed *effective rate* concept is considered. Supported by these results it is hypothesized that a time scale must be included in the rate enhancement formulation, to account for the retardation of cracks due to micro-inertia effects and the inherent delayed response to straining variation of the bulk material, of quasi-brittle materials.

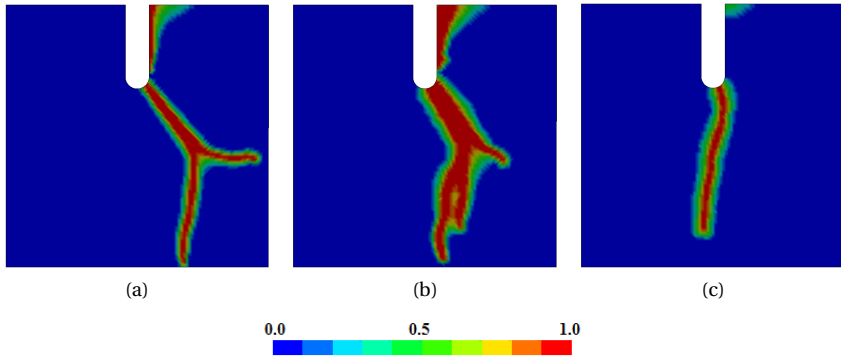


Figure 4.18: Final damage profiles for $\nu = 0.5$ m/s considering different definitions of rate: (a) Rate independent formulation; (b) Classical rate-dependent formulation ($\lambda = 0$) and (c) *Effective rate-dependent* formulation ($\lambda = 1.0$ ms).

4

4.5 CONCLUSIONS

In this chapter, a new *effective rate-dependent* damage model, enhanced by a stress-based nonlocal (SBNL) regularization scheme, was used to investigate the propagation and branching of cracks in quasi-brittle materials. Two examples were used for the numerical verification and validation of the model: (i) a single-edge notched tension test (academic example) and (ii) a *dynamic* compact tension test of concrete (experimental example). The proposed phenomenological model is mesh objective and reproduces the major phenomena associated with crack propagation and branching in quasi-brittle materials.

Based on the results of the single-edge notch test it is concluded that branching does not occur at a specific, material dependent, crack velocity. Under dynamic tensile loading conditions the evolution and bifurcation of cracks are material dependent phenomena influenced by both the load history and the geometry of the problem (boundary conditions). It was demonstrated that the evolution of the crack path and velocity are governed by the change of the principal stresses at the crack tip, which is controlled by the evolution of damage. With increasing crack speeds, the principal stresses at the crack tip tend to evolve from a mode-I to a mixed-mode state. Beyond a certain crack speed, the stress distribution around the crack tip reaches a critical state which favors damage development away from (parallel to) the forward cracking direction, and a single crack is no longer stable. When this condition is met, crack branching occurs whenever the stress field at the crack tip is destabilized by either a physical discontinuity or an interfering stress wave reflected at the specimen boundaries. Considering that a homogeneous material model is used, only the former effect could be investigated in this study.

It was discussed and demonstrated that a rate dependent formulation is needed to realistically represent the dynamics of cracks in quasi-brittle materials such as concrete. It was also shown that adjusting the material stiffness (strength) and energy with rate, as

it is usually done in classical rate-dependent formulation, is not enough. A time scale must be introduced in the formulation in order to account for the inherent micro and meso-scale structural inertia effects associated with cracking. In the present work, this is done with the recently proposed *effective rate* concept.

4.6 APPENDIX

While studying realistic models to simulate crack branching in brittle materials, different constitutive laws have been considered. In this appendix, results obtained considering two classical models widely used to characterize mode I and mixed mode failure of brittle and quasi-brittle materials are presented. These models have been implemented in LS-DYNA for the purpose of this study sharing the same damage law and different equivalent strain definitions: the modified von Mises model and the original Mazars' model [24]. Their biaxial failure (solid line) and yield (dashed line) envelopes are depicted in fig. 4.19 and compared with the model presented in this chapter.

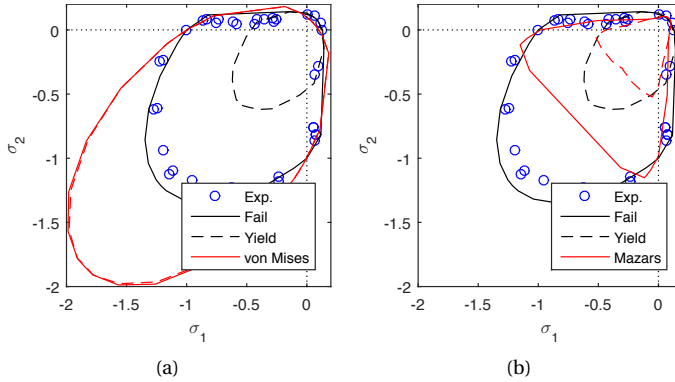


Figure 4.19: Comparison of the biaxial yield (dashed lines) and failure (solid lines) envelopes of the proposed model with: (a) modified von Mises and (b) Mazars' damage model [24].

The respective damage profiles and *crack* speeds obtained for the single-edge notched test from sec. 4.3 are depicted in fig. 4.20. These results show that both models can be used to describe response and failure of quasi-brittle materials. However, they should not be considered to represent the same material because the *crack* patters are different. Since the failure process is reflected in crack patterns after branching, these can be used as a complementary argument to characterize a quasi-brittle material.

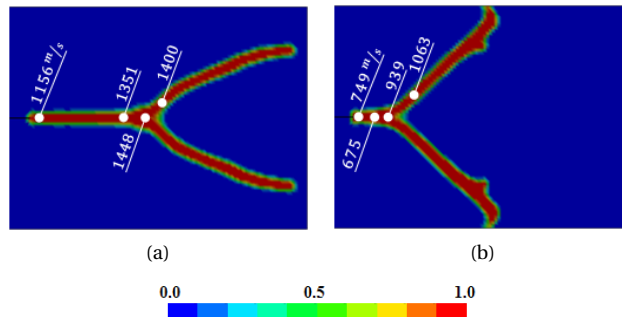


Figure 4.20: Influence of constitutive relations in the *crack* dynamics ($t = 50 \mu s$): (a) Modified von Mises and (b) Mazars' damage model [24].

5

SIMULATION OF BALLISTIC IMPACT ON CONCRETE TARGETS A NEW DAMAGE MODEL FOR CRUSHING AND COMPACTION

In this chapter, a hydrostatic damage is added to the formulation in order to take the damage of the material matrix observed while porosity reduces during compaction into account. Besides controlling the evolution of the nonlinear volumetric response of the material, this new damage variable contributes to the deterioration of the material stiffness upon confinement.

It is demonstrated that the description of the nonlinear volumetric response of concrete by an equation of state (EOS) as a plasticity phenomenon, as it is commonly done in hydrodynamic constitutive modeling, is unrealistic for concrete. Such formulations fail to represent the effect of the loss of cohesion observed during compaction on the deviatoric response of the material. By taking this phenomenon into consideration, the proposed model systematically predicts the relevant failure modes (cratering, tunneling, radial cracking and spalling) observed during ballistic impact on a concrete plate as a function of the projectile velocity and plate thickness.

This chapter is based on L. Pereira, J. Weerheijm, and L. Sluys. Simulation of compaction and crushing of concrete in ballistic impact with a new damage model. *Int. J. Impact Eng.*, 111:208-221, 2018.

5.1 INTRODUCTION

Extraordinary actions such as blast loadings and high velocity impact are rare, but usually have devastating effects. Thus, making critical infrastructures, such as military and governmental facilities, power-plants, dams, bridges, hospitals, etc., more resilient against these hazards is one of the best ways to protect ourselves and our societies. Since concrete is a very common construction material, the development of realistic numerical tools to efficiently simulate its failure behavior under extreme dynamic loading conditions is of paramount importance, but still a major challenge [5].

The capacity of a concrete structure to withstand these impulsive loads is mainly dictated by how it dissipates the incoming energy. For example, in the particular case of ballistic impact, a pressure wave is induced which expands radially through the structural element, leading to a complex process of interfering stress waves. Consequently, the material is exposed to rapidly changing multiaxial stress states and strain rate conditions. The material may fail locally *long before* the dominant structural response takes place. Experimental evidences with different quasi-brittle materials (see for example [12, 13]) suggest that the local evolution of failure in concrete during ballistic impact can be divided into five main stages (see fig. 5.1): (1) the formation of the Mescall zone due to crushing and compaction of the material in front of the impactor (strike face), associated with pore collapse and comminution (pulverization) of the material under pressure; (2) tunneling resulting from the flow of the comminuted (pulverized) material around the penetrator; (3) radial cracking in front and around the impactor, caused by hoop stresses raised in the wake of the initial pressure wave [9]; (4) spalling (tensile fracture) at the rear face, upon reflection of the pressure wave; and (5) formation/expansion of the crater due to spalling at the strike face [10]. Conical punching failure (Hertzian cone) may occur in some conditions, as an extension of preformed radial cracks, at the end of the projectile deceleration phase. In a later stage, structural oscillations at moderate strain rates become the leading loading condition and the main cause for further mechanical degradation [11], such as the formation of visible radial cracks at the front and back surfaces of the target. In a normal impact on a slender concrete plate, the extension or even the manifestation of the different failure modes depends on both the thickness of the concrete plate and the impact velocity. The dynamic failure observation of the target can vary from a small crater, for a relatively low impact velocity, to complete perforation, for a high velocity impact. The example depicted in fig. 5.1 represents an intermediate impact velocity where both cratering and spalling occurs.

Many aspects of the fracturing process of quasi-brittle and brittle materials, such as the propagation and branching of individual cracks and spalling, are now well understood and successfully simulated with various models (e.g. plasticity [17–23], damage [24–34], plastic-damage [8, 35–45] and fracture based approaches [6, 46, 47]). However, despite the vast literature on the topic, very few models used in dynamic FEM analysis are able to capture all relevant failure modes of concrete [47]. It is believed that the development of better models is being hampered by a poor description of material failure in front of the impactor, in the early stages of loading [8, 159]. Since the first failure mechanism governs how and how much energy is transmitted to the structure, a proper description of the initial phenomena responsible for the fragmentation (and

pulverization) of the material immediately after impact is critical for an adequate representation of the subsequent failure processes.

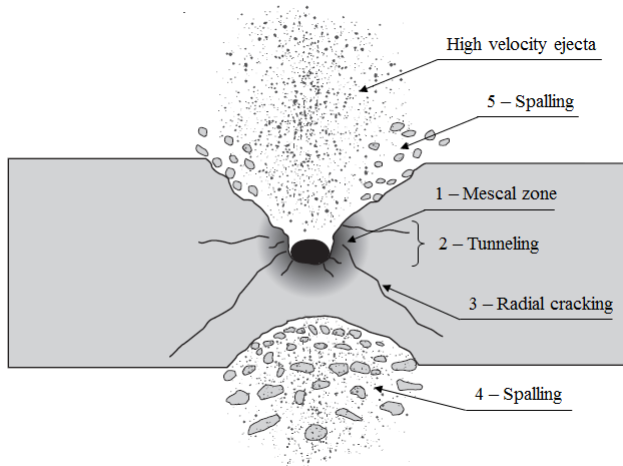


Figure 5.1: Failure mechanics in impact scenarios.

It is well known that concrete behavior is highly affected by both pressure and strain rate. But, considering the complexity and short duration of these events, it is technically impossible to separate the contributions of each to the fracturing processes and strength increase [114]. In reality, under dynamic loading conditions both pressure and rate increase simultaneously. It has been acknowledged that the raise of compressive strength observed at high strain rate loading tests is largely due to inertia-induced confinement, especially above a critical strain rate value, $\dot{\epsilon} > 10 \text{ s}^{-1}$. Many experimental, theoretical and numerical studies (e.g. [79, 92, 93, 95, 160–163]) support these observations and make it clear that the experimentally observed dynamic compressive strength increase with rate is not a constitutive property. For example, based on split Hopkinson pressure bar (SHPB) tests of concrete specimens cast in steel rings, Forquin et al. [164] recently proved that the strain rate effect on the material compressive strength is relatively small when structural inertia effects are minimized. Thus, experimentally derived dynamic increase functions (DIFs), like the one proposed in the CEB/*fib* model code [147], does not describe the dynamic increase of strength for modeling at constitutive level.

Experimental evidences suggest that, above a critical strain rate (10 s^{-1}), the dynamic compressive strength growth is followed by an increase in fragmentation. The experimental results of SHPB tests of concrete reveal that fragmentation evolves from a few large pieces at $\dot{\epsilon} \approx 30 \text{ s}^{-1}$, with fracture taking place almost exclusively through the mortar, to diffuse cracking at $\dot{\epsilon} \approx 300 \text{ s}^{-1}$, characterized by small fragments with fracture crossing both mortar and aggregates (see for example Al-Salloum et al. [162] and Zhang and Zhao [114]). This increase of fragmentation is usually interpreted as a consequence of additional crack initiation with rate, which leads to an increase of effective fracture surface (damage) and the ability to absorb energy [6, 90, 91]. The

increase of material strength observed in these experiments is mostly due to a raise of the inertia induced confinement. Only recently, in a series of triaxial and hydrostatic tests conducted at the university of Grenoble (France) [53, 165, 166], it was possible to evaluate the behavior of concrete at pressure levels similar to the ones observed in ballistic impact or after a blast, in controlled quasi-static conditions. It was shown that pressure alone is responsible for strength increase and the fragmentation process which leads to additional energy dissipation.

Fig. 5.2 schematically represents the different failure modes of concrete based on experimental observations of Gabet et al. [53] and Poinard et al. [166] of triaxial and hydrostatic quasi-static tests with confining pressures up to 650 MPa. These experimental results reveal that the failure mode/mechanism of concrete changes considerably with increasing pressure. This progressive alteration of the failure mode/mechanism is driven by the damage of the structure of the material while porosity decreases during compaction. At low confinement ($p < p_{el}$), the cement matrix is barely damaged and failure is characterized by a few localized cracks (zone b in fig. 5.2). But, with increasing pressures, the cement matrix is progressively crushed (damaged), leading to a triaxial diffuse damage mode characterized by numerous small cracks (zone c in fig. 5.2).

The hydrostatic tests in the same studies also help to explain the mechanisms behind the nonlinear volumetric behavior of concrete, and divide it in two stages. First, the strong volumetric deformation observed immediately after the elastic phase (zone c_i in fig. 5.2(b)) is the result of the collapse of the pores associated with significant damage (crushed) of the cement matrix, which leads to a reduction of the compressive/tangent stiffness of the material. Then, due to compaction and an increase of density, the compressive stiffness, of the material, which now behaves like a granular material, raises again until consolidation is reached, to K_{solid} (zone c_{ii} in fig. 5.2(b)). When confinement decreases and the stress state drifts away from the purely hydrostatic state, damage developed during compaction progressively manifests itself by a significant degradation of the elastic properties of the material and loss of tensile stiffness.

These results highlight the fact that it is not realistic to separate the hydrostatic and deviatoric response of the material, as it is commonly done in most models used for impact problems [12, 37, 167]. The nonlinear volumetric behavior of concrete is almost exclusively represented by an equation of state (EOS) characterizing pore compaction as a plasticity phenomenon, which is then combined with a damage (or plastic-damage) model describing the fracturing process associated with the deviatoric response. These approaches fail because they ignore the effect of loss of cohesion on the tensile strength and on the triaxial response as a function of the confinement level. The methodology followed in this paper takes this intrinsic property of geomaterials into consideration.

A new isotropic damage model is proposed to simulate the response of concrete under ballistic impact. Three damage variables are used to describe the evolution of failure as a function of the stress state of the material (see fig. 5.2) [8, 24]: (a) tensile (mode I) failure; (b) compressive-shear (mode II or mixed-mode) failure; and (c) hydrostatic damage (crushing) related to pore collapse and consolidation due to pressure. The proposed formulation is an enhanced version of the *effective*

rate-dependent nonlocal damage model [34], which includes the effect of the hydrostatic damage (crushing) of the material matrix under pressure on the material stiffness as a function of confinement. The proposed formulation has been developed and implemented as a *user defined material model* (UMAT) in LS-DYNA [48] following an explicit computation scheme.

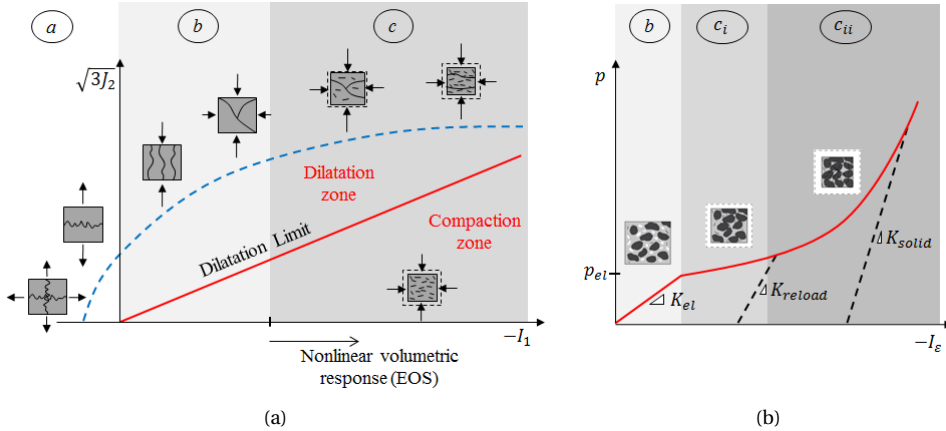


Figure 5.2: Schematic representation of failure modes of concrete alongside the (a) ultimate strength (failure) envelope in the deviatoric space and (b) nonlinear volumetric response (EOS) in the hydrostatic space. This graphical representation is based on the experimental observations in [53, 166]

After the description of the model in the following section (sec. 5.2), two sets of numerical studies are presented for validation. First (sec. 5.3), a series of single element analyses, representing the experiments conducted by Gabet et al. [53], is used to test the model under quasi-static triaxial-compression and hydrostatic loading conditions. Then (sec. 5.4), a set of tests reported in Beppu et al. [13] is simulated to evaluate how the increase of energy absorption provided by the added hydrostatic damage mode contributes to a more realistic representation of concrete's failure in ballistic impact situations.

5.2 CONSTITUTIVE LAW

The model presented here after is an extension of the recently proposed *effective rate-dependent* nonlocal damage model [34, 168], successfully used to simulate dynamic tensile failure (spalling) and the dynamic propagation and branching of cracks in concrete. The model is an evolution of the μ *damage model* proposed by Mazars et al. [31]. Two damage variables are considered to represent material failure under tension (ω_t) and compression-shear (ω_c) loading situations. Although the nonlinear response of the model is pressure dependent, as in the Drucker Prager model [169], the variation of strength or the deformation under compression cease to be realistic for high confining triaxial stress situations [52]. To overcome these limitations, a

hydrostatic damage variable (ω_h) is added to describe the damaging (crushing) of the cement/material matrix during compaction. The combined effect of the three damage variables (ω_t , ω_c and ω_h) is assembled in a single variable (ω) following an adapted version of the formulation proposed by Lee et. al [36]:

$$\omega = 1 - (1 - \omega_t)(1 - \omega_c)(1 - \omega_h^*) \quad (5.1)$$

where ω_h^* is the effective hydrostatic damage, actively contributing to the material stiffness degradation, as it is explained in sec. 5.2.3. Following a classical isotropic damage approach [102], the evolution of the material stiffness, and consequently the stress tensor, is simply described as follows:

$$\sigma = (1 - \omega)\tilde{\sigma} \quad \text{with} \quad \tilde{\sigma} = C : \varepsilon, \quad (5.2)$$

where ε is the strain tensor, C is the elastic stiffness tensor and $\tilde{\sigma}$ is the effective stress tensor.

In the following subsection (sec. 5.2.1) the damage model is described as in Pereira et al. [168]. In sec. 5.2.2, the volumetric response of the model is made nonlinear as a function of the hydrostatic damage (ω_h) and compaction (H_c). Then, in sec. 5.2.3 it is described how ω_h effectively contributes to the material stiffness degradation and the loss of tensile strength. Finally, in secs. 5.2.4 and 5.2.5, the rate enhancement and nonlocal regularization formulations are described, respectively.

5.2.1 TENSION AND COMPRESSION-SHEAR DAMAGE – CRACKING

The damage laws for tension (ω_t) and compression (ω_c) are defined as in the original Mazars model [24]:

$$\omega_i = 1 - (1 - A_i) \frac{Y_{i0}}{Y_i} - A_i e^{-B_i(Y_i - Y_{i0})} \quad (5.3)$$

where A_i and B_i are material parameters and Y_{0i} are the equivalent strain damage thresholds. The index i in this and the following equations should be interpreted as t for tension and c for compression. The evolution of damage in time (t) is derived from two monotonic thermodynamic variables Y_t and Y_c :

$$Y_i(t) = \max_{t \geq \tau} \left[Y_{i0}, r_i \varepsilon_i, Y_i(\tau) \right] \quad (5.4)$$

where ε_i are the equivalent strains and r_i the internal variables which provide information on the actual loading state [31, 36]. These variables were added to the formulation to weight the contribution of tension and compression to the nonlinear response of the material in mixed-mode stress conditions.

$$r = \frac{\sum_{I=1}^3 \langle \tilde{\sigma}_I \rangle}{\sum_{I=1}^3 |\tilde{\sigma}_I|}, \quad (5.5)$$

$$r_t = r^\alpha \quad \text{and} \quad r_c = (1 - r)^\alpha \quad \text{with} \quad \alpha \leq 0.1 \quad (5.6)$$

where $\langle \tilde{\sigma}_I \rangle$ and $|\tilde{\sigma}_I|$ are the positive and absolute values of the principal effective stresses, respectively.

The equivalent strains are scalar variables which characterize the local strain state in tension and compression, respectively:

$$\varepsilon_t = T_1 I_\varepsilon + T_2 \sqrt{3J_\varepsilon} \quad \text{with} \quad T_1 = \frac{0.5}{1-2\nu} \quad \text{and} \quad T_2 = \frac{0.5}{1+\nu} \quad (5.7)$$

$$\varepsilon_c = C_1 I_\varepsilon + C_2 \sqrt{3J_\varepsilon} - C_3 I_\varepsilon^2 \quad \text{with} \quad C_1 = \frac{0.2}{1-2\nu} \quad \text{and} \quad C_2 = \frac{1.2}{1+\nu} \quad (5.8)$$

where ν is the Poisson's ratio, and C_i and T_i are user-defined positive parameters which can be individually adjusted for calibration of the model. These quantities are defined in the deviatoric space, as a function of the first invariant of the strain tensor (I_ε) and the second invariant of the deviatoric strain tensor (J_ε):

$$I_\varepsilon = \varepsilon_1 + \varepsilon_2 + \varepsilon_3, \quad (5.9)$$

$$J_\varepsilon = \frac{1}{6} [(\varepsilon_1 - \varepsilon_2)^2 + (\varepsilon_2 - \varepsilon_3)^2 + (\varepsilon_3 - \varepsilon_1)^2]. \quad (5.10)$$

It is important to notice that, compared to the previous version of the model [168], and the original formulation by Mazars et al. [31], the compressive equivalent strain definition (ε_c) was updated with an extra dependency on the first invariant (I_ε^2). Although this change has a minor impact on the damage threshold of the model (see fig. 5.3), it leads to a retarded evolution of damage with pressure, considering that $C_3 \geq 0$. This change is in line with the model proposed by Comi and Perego [26], and aims to improve the description of the material behavior at low confinement levels [31].

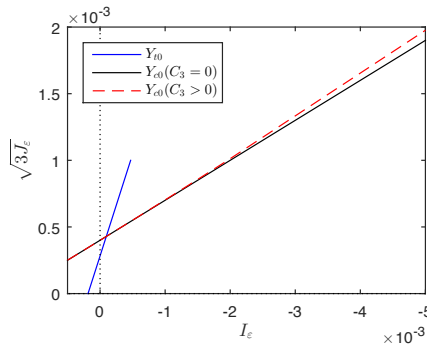


Figure 5.3: The effect of C_3 in the evolution of the Yield envelope under compression.

5.2.2 HYDROSTATIC DAMAGE (CRUSHING) AND COMPACTION

When concrete is subjected to high confining pressures, compaction occurs by reducing the voids (air) in the mixture and the physical connections between aggregates are ruptured irreversibly. These two combined mechanisms lead to the observed nonlinear volumetric deformation of material and the variation of the tangent stiffness (i.e. bulk modulus K) from K_{el} to K_{solid} during compaction (see fig. 5.2(b)). In the present study only the tangent stiffness is updated as a function of two volumetric

strain (ε_v) dependent variables: ω_h and H_c . The former variable describes the reduction of strength and stiffness associated with the loss of cohesion under pressure. The latter scalar variable (H_c) describes the increase of stiffness due to compaction of the material. The current effective bulk modulus is determined by weight averaging the two effects, as proposed by Desai [170].

$$K = \begin{cases} K_{new} = K_{el}(1 - \omega_h) + K_{solid}H_c & \text{if } \Delta\omega_h > 0 \\ K_{reload} = K_{el} + K_{solid}H_c & \text{if } \Delta\omega_h = 0 \end{cases} \quad (5.11)$$

where K_{new} is the updated effective bulk modulus in a compaction situation, i.e. when ω_h increases, and K_{reload} is the bulk modulus when there is no increase of ω_h .

In the absence of a full understanding of when these processes start and finish, for simplicity, both hydrostatic damage and compaction are described by identical power laws with the only difference being the exponent.

$$\omega_h = \left(\frac{\mu_h - \mu_0}{\mu_{gran} - \mu_0} \right)^{\gamma_\omega} \quad \text{with } \gamma_\omega < 0.5 \quad (5.12)$$

$$H_c = \left(\frac{\mu_h - \mu_0}{\mu_{gran} - \mu_0} \right)^{\gamma_c} \quad \text{with } \gamma_c = 1 \quad (5.13)$$

where

$$\mu_h(t) = \max_{t \geq \tau} [\mu_0, \mu, \mu_h(\tau)] \quad (5.14)$$

and

$$\mu = -\varepsilon_v = -\varepsilon_{11} - \varepsilon_{22} - \varepsilon_{33}.$$

The powers $\gamma_i \in [0, 1]$ are user defined parameters and μ_h is the volumetric equivalent strain. The parameters μ_0 and μ_{gran} are the volumetric strain at the onset of damage and at the fully damaged (compacted) state, respectively. For simplicity, linear compaction of the material is assumed ($\gamma_c = 1$). Please note that K is different in case of compaction or in a reloading situation, i.e. when ω_h increases or not. This feature is needed to capture the experimentally observed unload-reloading bulk modulus (K), which is almost not affected in the early stages of compaction. This correction also prevents unrealistic numerical negative volumetric straining of the material in case of unloading. Fig. 5.4(a) shows the variation of the bulk modulus (K) with volumetric deformation (ε_v), for both loading and reloading situations, for a model calibrated according to the properties defined in sec. 5.3 (see tab. 5.1). In fig. 5.4(b) the early stages of the nonlinear volumetric deformation with pressure (EOS) are plotted together with the evolution of hydrostatic damage (ω_h) and compaction (H_c). In this case, damage needs to grow fast in order to reproduce the pronounced decrease of the tangent stiffness, which, according to Gabet et al. [53], is related to a rapid loss of cohesion of the material observed in the early stages of compaction (see fig. 5.4(b)).

The implementation of this formulation takes advantage of the used explicit computation scheme to determine the evolution of the effective pressure (\bar{p}) with the variation of K and $\Delta\varepsilon_v$:

$$\bar{p} = \begin{cases} -K_{el} \varepsilon_v & \text{if } (\varepsilon_v \geq 0 \text{ or } \omega_h = 0) \\ \max[0, \bar{p}_{old} + \Delta\bar{p}] & \text{if } (\varepsilon_v < -\mu_0 \text{ or } \omega_h > 0) \end{cases} \quad (5.15)$$

with

$$\Delta \bar{p} = -K^* \Delta \varepsilon_v \quad (5.16)$$

where \bar{p}_{old} is the pressure in the previous time step, and $\Delta \bar{p}$ is the variation of the effective pressure determined as a function of the current bulk modulus K^* , which is respectively K_{new} or K_{reload} when ω_h is increasing or not. The final effective stress tensor is determined following the conventional decomposition in deviatoric (S_{ij}) and hydrostatic (p) stress tensor:

$$\tilde{\sigma}_{ij} = \tilde{S}_{ij} + \tilde{p} \delta_{ij} \quad (5.17)$$

with

$$\tilde{S}_{ij} = 2G e_{ij} \quad \text{with} \quad e_{ij} = \varepsilon_{ij} - \frac{1}{3} \varepsilon_v$$

where G is the elastic shear modulus and e_{ij} is the deviatoric strain tensor.

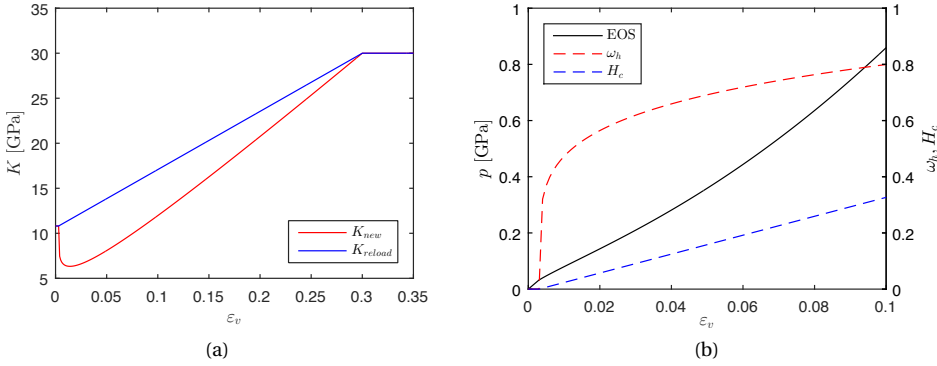


Figure 5.4: Variables evolution with volumetric strain (ε_v): a) Bulk Modulus (K) and b) compaction (H_c) and hydrostatic damage (ω_h).

5.2.3 EFFECTIVE HYDROSTATIC DAMAGE (ω_h^*)

As described before, when a concrete-like material is subjected to pure hydrostatic loading, crushing and compaction may occur (see figs. 5.2). Even though the material skeleton is irreversibly damaged (crushed) in the early stages of compaction and concrete degenerates from a cohesive material into a granular material, it appears to become stronger during this process. Like in a soil, this is because the material is kept confined. But, when confinement decreases, the damage developed during compaction progressively influences the global response of the material. In this study, the effective contribution of crushing to the degradation of the material stiffness, i.e. contribution of ω_h to the global damage ω , is governed by the effective hydrostatic damage ω_h^* (see eq. 5.1):

$$\omega_h^* = r_{conf} \omega_h \quad (5.18)$$

where r_{conf} is a confinement factor, considered to be inversely proportional to the effective triaxiality state (TF) of the material:

$$r_{conf} = \min \left[\max \left(0, \frac{3\sqrt{3}J_{\bar{\sigma}}}{-I_{\bar{\sigma}}} \right), 1 \right]. \quad (5.19)$$

As schematically represented in fig. 5.5(a), the confinement factor (r_{conf}) varies between 0 and 1. It is zero ($r_{conf} = 0$) in a purely hydrostatic stress state and progressively increases when $J_2 > 0$, until the stress state reaches the ‘confinement limit’. Please note that r_{conf} is defined as a function of the material invariants of the effective stress tensor in order to be consistent with the stress factor r (eq. 5.5), used to weight the contribution of tension and compression to the material nonlinear response.

The conceptual approach followed in this paper is schematically represented in fig. 5.5. It illustrates the fundamental parts of the model, in both deviatoric (fig. 5.5(a)) and volumetric (fig. 5.5(b)) spaces, explained in the previous subsection (secs. 5.2.1 to 5.2.3).

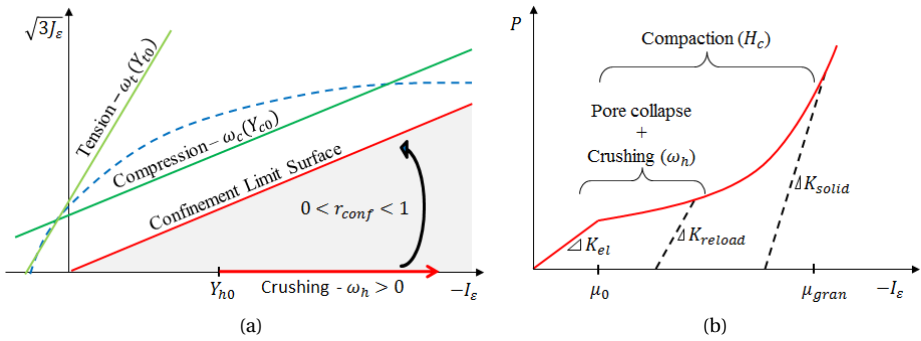


Figure 5.5: Schematic representation of the proposed damage model considering the (a) yield envelopes and confinement factor variation in the deviatoric space and (b) the nonlinear volumetric response governed by ω_h and H_c in the hydrostatic space.

5.2.4 RATE ENHANCEMENT

As it is well known, concrete is a highly rate-dependent material. The observed variation of strength and fracture energy with rate is mainly caused by three phenomena: (i) change of fracturing process, associated with an increase of micro-cracking activation and consequently an increase of the effective fracture surface, with rate [86, 87]; (ii) viscous properties of the bulk material between cracks which lead to the retardation of cracking due to inertia (i.e. time-dependency of damage) [35, 64, 85]; and (iii) structural inertia forces [79, 93, 171, 172]. Only the latter phenomenon is naturally captured in continuum finite element modeling. The former two must be considered as inherent dynamic properties of the material and therefore, explicitly included in the constitutive relations.

From the three damage modes described by the model proposed above, only ω_t and ω_c describe mechanisms involving the propagation of cracks (i.e. cracking). Therefore,

only these failure modes are considered to be rate dependent. Following common practice, crushing (ω_h) and compaction (H_c) are considered rate independent phenomena. This is a simplification rather than physically objective, since experimental results suggest that the EOS is also rate dependent [37]. As in a typical rate-dependent damage formulation, the variation of the material strength and strain-energy associated with cracking are dynamically updated as a function of rate. This is done by updating the damage threshold Y_{i0} and the parameter B_i in the damage evolution law (eq. 5.3):

$$Y_{i0}^{dyn} = Y_{i0}(1 + \zeta_i R_i^{\eta_i}), \quad (5.20)$$

$$B_i^{dyn} = B_i \left[1 - \delta_i \ln \left(\frac{R_i}{\dot{Y}_0} \right) \right], \quad (5.21)$$

where ζ_i , η_i and δ_i are material constants, defined respectively for tension and compression. The parameter \dot{Y}_0 , represents the rate after which the loading is classified as dynamic. Consistently with the *fib* recommendation [147], $\dot{Y}_0 = 10^{-6} \text{s}^{-1}$ is assumed.

Unlike what is commonly done in *hydro-dynamic* modeling, in this formulation, the material strength and energy are updated as a function of an *effective rate* (R) instead of the *instantaneous* strain rate ($\dot{\epsilon}$). The *effective rate* is a time dependent quantity conditioned by the immediately preceding strain history which accounts for the time-dependency of cracking [34]. In this model it is assumed that the effect of a variation of the strain rate takes some time (λ) to be experienced by the material and becomes effective. This is done by restricting the evolution of rate in case of a negative (R_{down}) or a positive (R_{up}) variation of the equivalent-strain rate ($\dot{\epsilon}_i$), according to the following equations:

$$R_{down} = \max \left[\dot{\epsilon}_i(\tau) e^{-\frac{t-\tau}{\lambda}}, \dot{\epsilon}_i(t) \right] \quad \text{for all } t \geq \tau \quad (5.22)$$

$$R_{up} = \min \left[\dot{\epsilon}_i(\tau) e^{\frac{t-\tau}{\lambda}}, \dot{\epsilon}_i(t) \right] \quad \text{for all } t \geq \tau \quad \text{and } \omega > 0 \quad (5.23)$$

where λ is a user defined *characteristic time* of the material, t is the current time and τ is the last time that *strain rate* ($\dot{\epsilon}_i$) was constant. In the current formulation, the *effective rate* is independently defined for tension and compression as the variation in time of the respective equivalent strains, i.e. $R_t(\dot{\epsilon}_t)$ and $R_c(\dot{\epsilon}_c)$. For more information about this model, the reader is referred to the work by Pereira et al. [34, 168].

5.2.5 REGULARIZATION MODEL – STRESS BASED NONLOCAL

To overcome spurious mesh sensitivity, typical for standard ‘local’ damage models, a regularization scheme is needed. In this study, only the equivalent strains for tension and compression are regularized. These quantities are independently weight averaged considering the same interaction domain, determined according to an updated version of the stress-based nonlocal regularization scheme presented by Giry et al. [49]. No regularization is needed for the volumetric strain (μ_h) because, alongside to the hydrostatic damage (ω_h), it develops in a confined state and leads to hardening effect. Furthermore, considering the example of high velocity impact, the material that fails under pressure is most often pulverized making it impossible to define a suitable length.

As in any other nonlocal formulation of integral type, the stress response at a material Gauss point (x) has been made dependent on its neighbors (ξ) by weight averaging a certain internal variable Z with the interaction domain Ω following eq. 5.24. The nonlocal update of the damage model is simply attained by replacing variable Z by its nonlocal counterpart (\bar{Z}).

$$\bar{Z}(x) = \frac{\int_{\Omega} \alpha(x, \xi) Z(\xi) d\Omega}{\int_{\Omega} \alpha(x, \xi) d\Omega} \quad (5.24)$$

where $\alpha(x, \xi)$ is an arbitrary weight function, here considered to be the Gaussian function:

$$\alpha(x, \xi) = e^{-\left(\frac{2\|x - \xi\|}{l_r}\right)^2} \quad (5.25)$$

where l_r is the characteristic material length.

In a stress-based nonlocal formulation, the influence of the neighboring elements stress state is introduced in the description of the nonlocal interactions by updating the interaction length between the Gauss point x and its neighbors ξ , $l_{x\xi} = l_{x\xi}$ in eq. 5.25, as follows:

$$l_{x\xi} = \rho(x, \xi) l_r \quad (5.26)$$

with

$$\rho^2(x, \xi) = \frac{1}{(f_t^{dyn})^2 \left(\frac{\sin^2 \varphi \cos^2 \theta}{\langle \sigma_1 \rangle^2} + \frac{\sin^2 \varphi \sin^2 \theta}{\langle \sigma_2 \rangle^2} + \frac{\cos^2 \varphi}{\langle \sigma_3 \rangle^2} \right)} \quad (5.27)$$

where φ and θ are the angles between the eigenvectors of the principal stress tensor σ_I , with $I = 1, 2$ and 3 , at point ξ defined in a conventional spherical coordinates system. f_t^{dyn} is the dynamic tensile strength of the material updated as a function of Y_{t0}^{dyn} defined in eq. 5.20. Considering that $\langle \cdot \rangle$ are the Macaulay brackets, the expression between parentheses is the projection of the positive part of σ_I over the vector $x\xi$, $\langle \sigma_{x\xi} \rangle$. So, $\rho(x, \xi)$ is a coefficient that varies between zero and one for tensile stresses and is equal to zero otherwise. A non zero interaction length must be used to prevent localization to occur in a zone smaller than the finite element, which is impossible and would lead to mesh dependency again. So, the interaction length between two points is allowed to vary between l_r and a minimum length l_{min} . For more information about this model and the computation scheme used for this research, the reader is referred to the works by Girya et al. [30, 49] and Pereira et al. [33, 34, 168].

5.3 SINGLE ELEMENT STUDY - TRIAXIAL AND HYDROSTATIC TESTS

In this section, a series of single finite element analyses is used to evaluate whether the quasi-static triaxial-compression and hydrostatic response of concrete improves with the addition of the new damage mode, ω_h . The simulated loading conditions are identical to the ones in the test series of Gabet et al. [53]. As it can be seen in fig. 5.6(a), in case of a triaxial test, a two stage loading procedure was considered. First, a

hydrostatic pressure was applied to all surfaces. Then, the nodes on the top surface were displaced in the direction perpendicular to its plane. In the hydrostatic test (fig. 5.6(b)), a pressures of increasing magnitude, (400 and 650 MPa) are applied cyclically to the element.

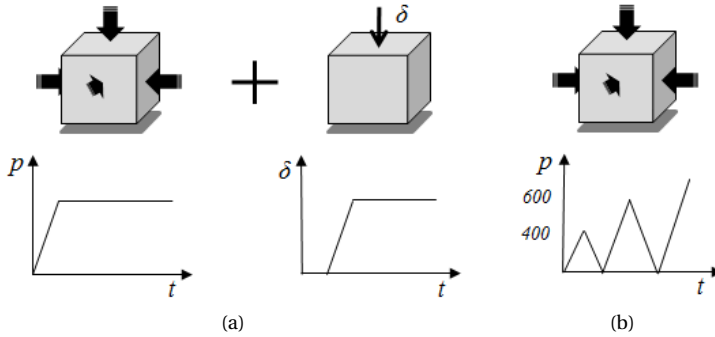


Figure 5.6: Single element loadings [53]: (a) triaxial-compression and (b) cyclic hydrostatic tests.

The material was calibrated with the information available in the original publication [173]. Considering that only the mean compressive strength ($f_c = 30$ MPa) and the density ($\rho = 2270$ kg/m³) of the material used in the experimental campaigns are provided, the remaining properties of the model were calibrated in order to meet Eurocode 2 [4] recommendations for uniaxial compression. The remaining properties were tuned to fit the triaxial results for the highest confining pressure ($\sigma_m = 650$ MPa). The complete parameter set is summarized in tab. 5.1.

Table 5.1: Constitutive law parameters – triaxial test

Symbol	Parameter	Symbol	Parameter	Symbol	Parameter
f_c	30 MPa	Y_{c0}	4.0×10^{-4}	μ_{h0}	0.003
E	24 GPa	A_c	1.30	μ_{gran}	0.3
ρ	2300 kg/m ³	B_c	460	K_{sol}	30 GPa
ν	0.13	C_3	0.0 / 2.5	γ_ω	0.2

In order to highlight the influence of each new aspect of the proposed formulation, the simulated triaxial response of the model is presented in three steps, in figs. 5.7, 5.8 and 5.9. The results for the axial ($\sigma_1 - \varepsilon_1 / \varepsilon_2$) and volumetric ($\sigma_m - \varepsilon_v$) response of the model are plotted (colored lines) together with the respective experimental results (gray lines) [173].

Figs. 5.7 shows the triaxial response of the original model ($C_3 = 0$) according to Pereira et al. [168] (Model 0). Although this model provides a realistic representation of the unconfined uniaxial compression behavior of concrete [31], it clearly misrepresents both the variation of strength and deformation with pressure.

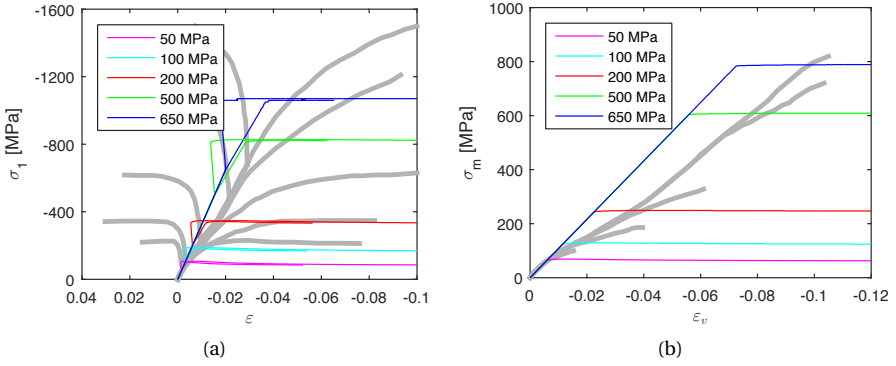


Figure 5.7: Simulated triaxial response of the original model ($C_3 = 0$) according to Pereira et al. [168] (colored lines) compared to experimental results (gray lines): a) stress-strain and b) volumetric behavior curves.

5

The results in fig. 5.8 correspond to the updated version of the original model which only considers the nonlinear volumetric response of the material under pressure (EOS) and ignores the influence of ω_h on the deviatoric response of the material (Model 1), i.e. the effective hydrostatic damage (ω_h^*) in eq. 5.1 is not considered, consequently:

$$\omega = 1 - (1 - \omega_t)(1 - \omega_c)$$

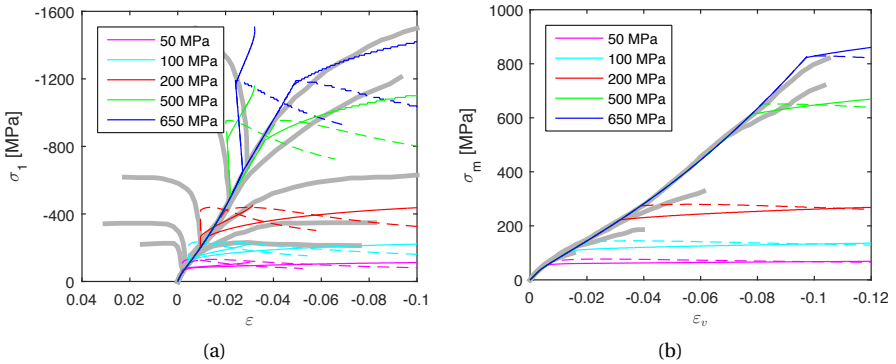


Figure 5.8: Simulated triaxial response considering $r_{conf}=0$ (colored lines) compared to experimental results (gray lines). a) Stress-strain and b) volumetric behavior curves, considering $C_3 = 0$ (dashed lines) and $C_3 = 2.5$ (solid lines).

With this modification, the results improve considerably in the first stage of loading, when stresses are kept in a pure hydrostatic state, but remain unsatisfactory in the later stage. As it can be seen in fig. 5.8, by comparing the simulated results in solid and dashed lines, the parameter C_3 controls the deviatoric response of the model with pressure. By controlling this parameter in eq. 5.8, it is possible to improve the model

response but only for a limited range of confining pressures. It is worth noting that these results are identical to the ones obtained with other models used for concrete based on plasticity or plastic-damage theories where the deviatoric and hydrostatic phases are treated separately. For example, see the simulated results of the same experiments in fig. 6 in Pontiroli et al. [174] and fig. 5.2 in Gabet [175] for a comparison with the PRM model [176].

Finally, figs. 5.9 and 5.10 show the triaxial and hydrostatic predictions of the complete version of the model developed in this study (Model 2), respectively. As it can be seen, the results are very realistic for all loads. Only the dilatation is still not well represented, especially for lower confining pressures (fig. 5.9(a)). However, to solve this using an isotropic damage model is very difficult, if not impossible. The possible solution is to consider a non-associative flow rule or an anisotropic damage approach where the shear and bulk properties of the model are treated separately.

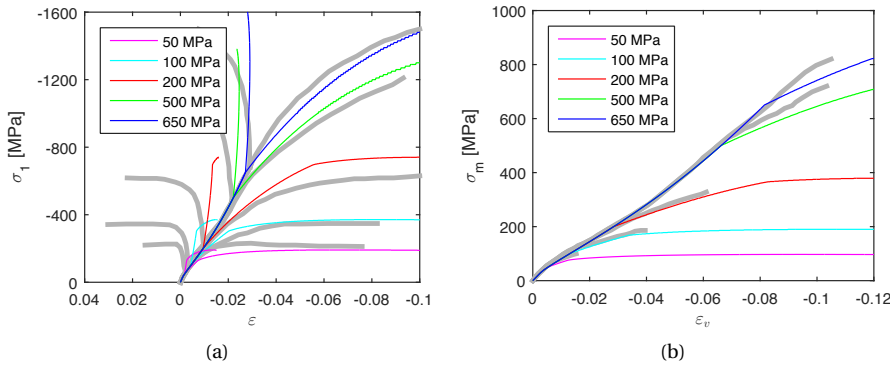


Figure 5.9: Simulated triaxial response of the proposed model considering $C_3 = 2.5$ (colored lines) compared to experimental results (gray lines): a) stress-strain and b) volumetric behavior curves.

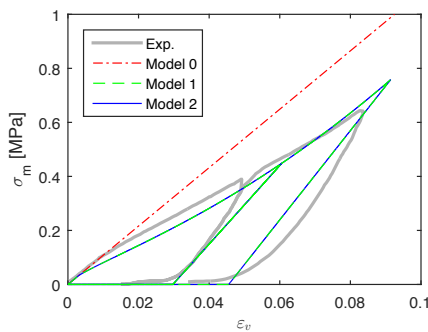


Figure 5.10: Comparison between cyclic hydrostatic experimental (gray line) and the simulated results for the different versions of the proposed model: dot-dashed red line – original model at [168] (Model 0 – cf. fig. 5.7); dashed green line – model ignoring ω_h^* in eq. 5.1 (Model 1 – cf. fig. 5.8); and solid blue line – final version of the model (Model 2 – cf. fig. 5.9)

It is important to notice that the response of the model in purely hydrostatic loading (see fig. 5.10) is the same. So, this is clearly independent of considering ω_h^* in eq. 5.1, as in the final version of the model (cf. fig. 5.9), or not (cf. fig. 5.8). So, in order to better understand the effect of ω_h on the global response of the model one needs to track the evolution of the different damage variables (ω , ω_c and ω_h^*) in multiple triaxial loading situations. As it can be seen in fig. 5.11, by considering the effect of ω_h^* on the global damage (ω) evolution, softening starts immediately after the axial deformation is applied. This has a significant impact on the deviatoric response of the model, slowing down the total damage rate and correcting the global volumetric deformation. As it can be seen in fig. 5.9, this leads to a response that becomes ‘dilating without reaching a peak stress’ with increasing confinement [166], consistent with experimental observations.

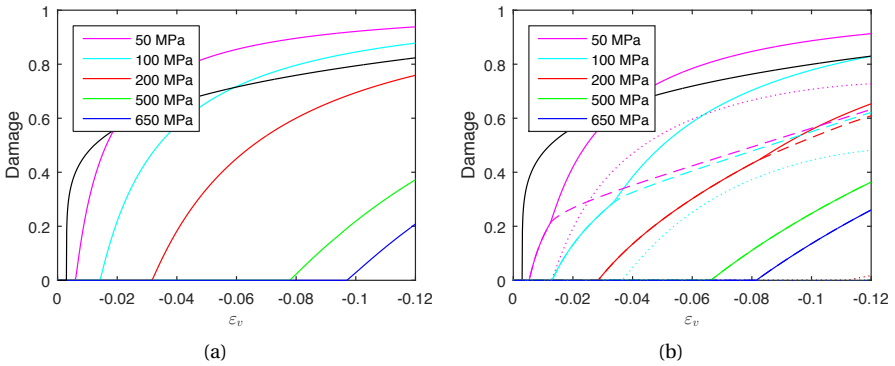


Figure 5.11: Evolution of different damage variables: (a) model ignoring ω_h^* in eq. 5.1 (Model 1 – cf. fig. 5.8) and (b) final version of the model (Model 2 – cf. fig. 5.9). Lines: solid – ω , dotted – ω_c , dashed – $\omega_h^* = r_{conf}\omega_h$. Note: ω_h is independent of the loading path (black lines).

These results also suggest that the failure mode under triaxial loading conditions changes considerably with confinement. It can be seen that, although the contribution of ω_c to the global stiffness degradation is high for low confinement, it disappears for pressures higher than 200 MPa. This is consistent with experimental evidences which indicate that, although the cement matrix is damaged under low confinement, failure of concrete is considerably localized. But, for high confinement conditions, failure is caused by diffuse damage (see fig. 5.2).

5.4 HIGH VELOCITY IMPACT

For obvious practical reasons, when studying ballistic impact, researchers focus primarily on the influences of the concrete grade/quality, target geometry and impact velocity on the penetration depth or residual velocity of the projectile. Very few studies are dedicated to the analysis of the initiation and evolution of the different failure modes taking place during such events [13, 177, 178]). The experimental work by Beppu et al. [13] can be taken as a reference in this matter because, in addition to the typical analysis of the post mortem specimens to determine the perforation depth and size of

crater and spalling area, high speed video cameras were used to record the evolution of cratering and spalling. These authors conducted a systematic study designed to investigate how the local failure process on plane concrete plates change with projectile velocity and target thickness, during ‘rigid’ impact. Single steel mushroom-like projectiles were fired against a series of $500 \times 500 \text{ mm}^2$ squared concrete plates with thicknesses ranging from 30 mm to 130 mm. Only impact normal to the plate surface was investigated, with velocities ranging between 200 m/s and 500 m/s. A set of the reported tests has been simulated for the numerical validation of the proposed model.

5.4.1 MODEL DESCRIPTION AND CALIBRATION

Although the targets are squared, the experiments were simulated with two dimensional axisymmetric models, as described in fig. 5.12. The problem was discretized with 2 mm quadrilateral linear finite elements, except for the mesh sensitivity analysis where different mesh sizes between 1 mm and 4 mm were considered for the target. The displacements of the nodes at top and bottom surfaces close to the edge of the plate (15 mm) were restricted vertically, in order to simulate the constraints of the supporting frame used in the experiment.

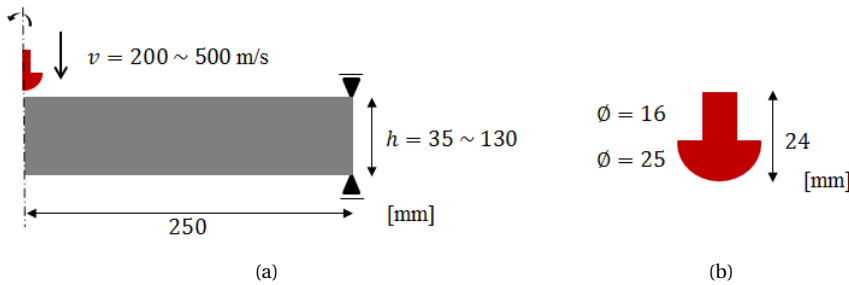


Figure 5.12: Schematic representation of experiment at Beppu et al. [13]. (a) Target and (b) projectile

Considering the limited information about the mechanical properties of both projectile and target, some assumptions had to be made in order to calibrate the models. The parameters used to simulate the concrete target are summarized in table 5.2. The considered elastic properties (E , ρ and ν) are the ones reported in the experimental paper [13]. The damage laws for tension and compression were calibrated in order to have a realistic quasi-static representation of a concrete with a compressive strength of $f_c = 25 \text{ MPa}$, as the one used in the experimental campaign. The hydrostatic damage and compaction laws were calibrated in order to have a nonlinear volumetric response under pure hydrostatic deformation (EOS) similar to reference models in literature [18, 179, 180] (see fig. 5.13(a)). The parameters in the rate dependent law for tension (ζ_t , η_t and δ_t) were calibrated to fit the modified dynamic increase factor (DIF) law proposed by Malvar and Ross [80], as it has been considered by the authors [34, 168] in previous studies. For compression, the DIF function proposed by the CEB/*fib* model code [147] was used as a reference ignoring the overstress/enhancement registered at rates above 1 s^{-1} , i.e. basically extending the initial DIF law for the entire deformation

rate range (see fig. 5.13(b)).

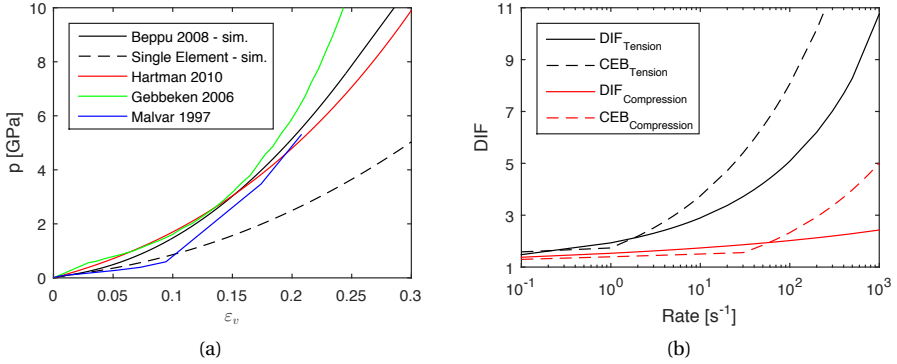


Figure 5.13: Material (a) hydrostatic and (b) dynamic behavior determined in single element simulations with monotonic loadings.

5

The calibration of the nonlocal model is not a trivial task and therefore not discussed in this paper. For consistency with the authors previous work [34, 168], the intrinsic lengths were set as $l_r = 12$ mm and $l_{min} = 2$ mm (the reference mesh size in this study). It is worth noting that, in tensile and mixed-mode loading conditions, this choice leads to an effective fracture process zone width of $10 \sim 20$ mm, with a ‘localized’ damage profile, which is in good agreement with experimental observations [139]. The maximum time step used in this study was 30% of the critical time step which, as it has been shown in previous work [33], ensures numerical stability.

Table 5.2: Constitutive law parameters – high velocity impact

Symbol	Parameter	Symbol	Parameter	Symbol	Parameter
E	25.5 GPa	ρ	2315 kg/m ³	ν	0.15
Y_{t0}	9.8×10^{-5}	A_t	1.0	B_t	10 000
Y_{c0}	6.0×10^{-4}	A_c	1.0	B_c	580
α	0.10	C_3	2.0	γ_ω	0.15
μ_0	0.003	μ_{gran}	0.25	K_{solid}	60 GPa
η_t	0.80	ζ_t	0.35	δ_t	0.045
η_c	0.30	ζ_c	0.20	δ_c	0.030
λ_t	1.0 ms	λ_c	1.0 ms	$l_r(l_{min})$	12(2) mm

The projectile was simulated with two different material models: a rigid model (*MAT020*) and a bilinear elastoplastic model (*MAT003* with $E_1 = 210$ GPa, $E_2 = 2.1$ GPa and $\sigma_{yield} = 225$ MPa). The first approach is consistent with the one followed by Beppu

et al. [13] assuming that the damage and deformation observed in the projectiles during impact are negligible. The second approach gives a more realistic representation of steel, the projectile material. Both approaches are considered in order to evaluate how the deformation of the impactor influences the dynamic evolution of damage on the target. In all analyses presented hereafter, the simulated results for the different impactors are presented together, with the results of a rigid impactor on the left and the ones of an elastoplastic impactor on the right, in a mirror configuration.

The interaction between impactor and target was modeled by a penalty-based contact algorithm with a coefficient of friction $\mu_c = 0.5$. Numerical erosion had to be taken into account, in order to avoid premature termination of the numerical analysis due to a negative Jacobian and to reduce the computation time, by removing the highly distorted elements. The volumetric strain (ε_v) and damage (ω) were used to define the numerical erosion criteria. The deletion of an element was triggered when $\omega > 0.99$ and ε_v exceeding a predefined threshold. After a sensitivity study, this threshold was set to $\varepsilon_v = 2.0$. This is the lowest value above which the effects on the damage evolution is negligible in the case of a $v = 420$ m/s impact in a $h = 90$ mm thick plate, therefore used in all simulations.

Fig. 5.14 depicts the damage profile at a $h = 90$ mm thick plate impacted at $v = 420$ m/s with an elastoplastic projectile projected on the mid section of the corresponding experimental test. As it can be seen, the damage profile agrees very well with the fracture patterns. Except for the penetration depth which is slightly overestimated, both the extension and shape of the crater and spalling are identical to the experiments. The predicted angle and extension of the conical crack is also very close to the visible crack.

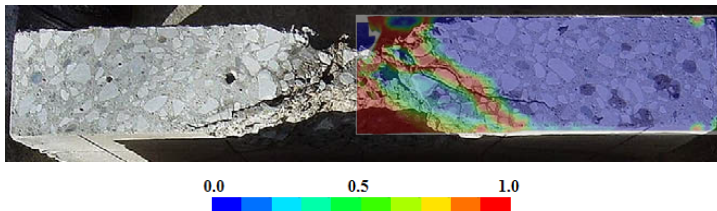


Figure 5.14: Comparison between experimental fracture patterns (mid section) and the final damage profile ($t = 1.0$ ms) of a $h = 90$ mm thick plate impacted at $v = 420$ m/s.

5.4.2 MESH SENSITIVITY

From the mesh sensitivity analysis shown in fig. 5.15 it is concluded that the results tend to become objective upon mesh refinement. The same erosion criteria were considered for all depicted results. However, it was observed that an increase of the erosion threshold with mesh refinement results in better convergence but, this choice has a significant impact on the computation time which becomes prohibitive for the finer mesh.

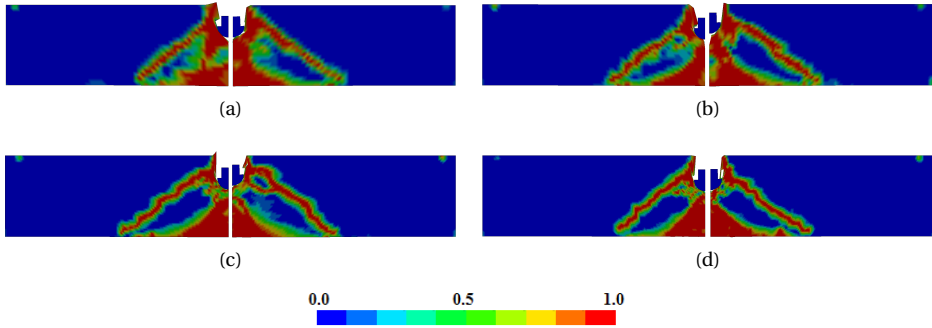


Figure 5.15: Mesh sensitivity analyses ($l_r = 12$ mm and $l_{min} = 2$ mm). Damage profiles at $t = 0.25$ ms of a $h = 90$ mm thick plate impacted at $v = 420$ m/s by a rigid (left) and elastoplastic (right) projectiles: (a) 4 mm, (b) 3 mm, (c) 2 mm and (d) 1 mm.

5

5.4.3 EVOLUTION OF DAMAGE

Fig. 5.16 shows snapshots of the damage profiles of a $h = 90$ mm thick plate impacted at $v = 420$ m/s by a rigid (left) and elastoplastic (right) projectile.

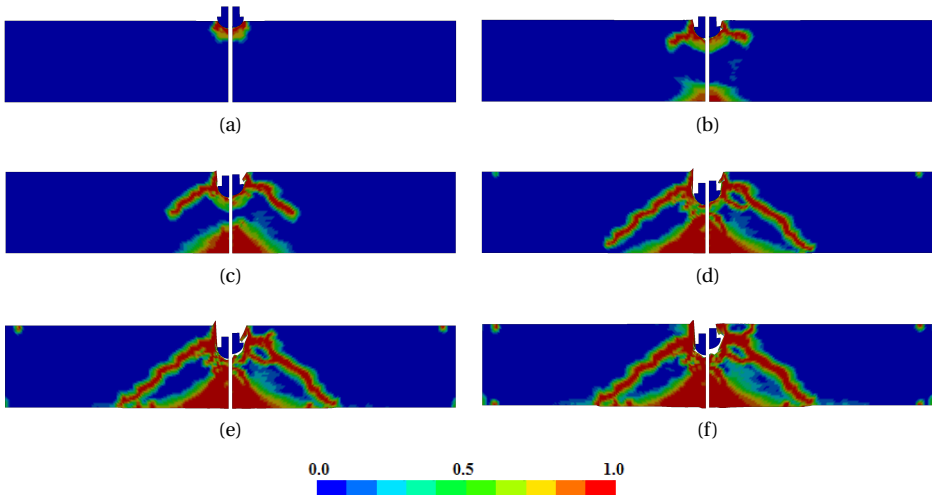


Figure 5.16: Evolution of damage in a $h = 90$ mm thick plate impacted at $v = 420$ m/s by a rigid (left) and elastoplastic (right) projectiles: (a) $t = 0.02$ ms, (b) $t = 0.06$ ms, (c) $t = 0.10$ ms, (d) $t = 0.20$ ms, (e) $t = 0.50$ ms and (f) $t = 1.0$ ms.

This sequence of events is consistent with the reported experimental observations. The high speed videos footage revealed that the sequence of events in this case is: (1) penetration followed by ejection of a fine powder; (2) spalling at the rear face with the material in the center being ejected first and at higher velocity; and (3) spalling at the

impacted face leading to enlargement of the crater. In addition to these observations, the simulated results also show that the conical crack due to punching starts growing when the impactor is close to being stopped.

These results show that a proper characterization of the impactor and the target are equally important. By comparing the final damage profiles of the rigid and elastoplastic projectiles, on the left and right of fig. 5.16(f), it becomes clear that the enlargement of the crater is partially due to the rebound of the projectile, which leads to the expansion of the crack formed in the early stages of the impact event. Furthermore, the penetration depth increases when the deformation of the impactor is ignored.

5.4.4 EFFECT OF IMPACT VELOCITY AND TARGET THICKNESS ON FRACTURING PROCESS

Figs. 5.17 compares the numerical results at $t = 0.25$ ms of $h = 80$ mm plates impacted at different velocities with the respective experimental results (images of impacted and back faces of the concrete plate).

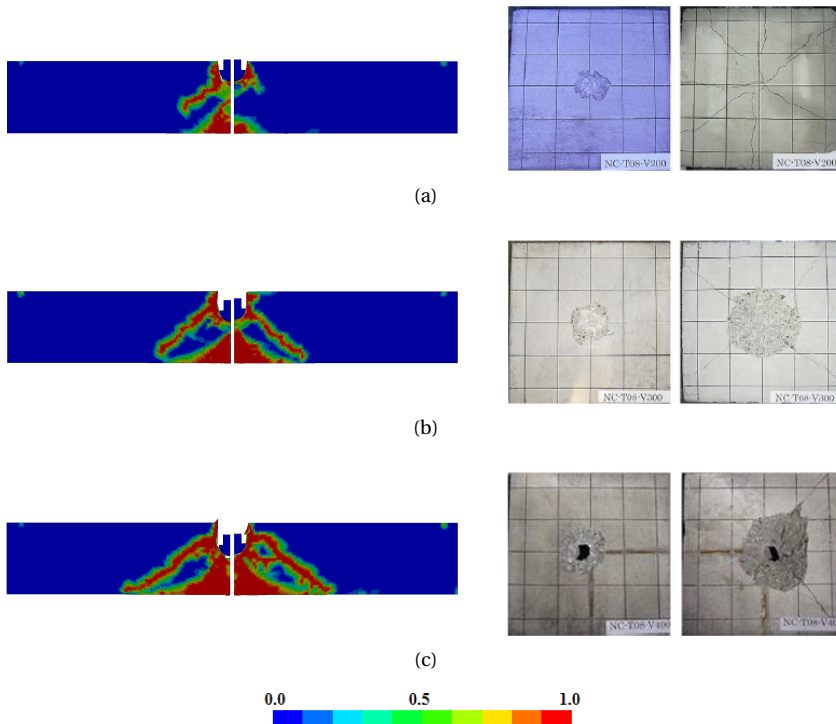


Figure 5.17: Comparison between the damage profile at $t = 0.25$ ms (left) and the respective experimental results (images of impacted and back faces) of a $h = 80$ mm plate impacted at different velocities: (a) $v = 210$ m/s, (b) $v = 310$ m/s and (c) $v = 415$ m/s.

The predictions show a good similarity with the experimental results. Only at the lower impact velocity the predicted damage seems to be more extensive than the

experimental data. This is particularly evident when a rigid projectile is used (figs. 5.17(a - left)). Although limited spalling is predicted at the back face when the projectile is simulated as elastoplastic, these results may be interpreted as realistic because, even though no spalling is observed in the experiments, it does not mean that the material at the back surface of the plate is not damaged. For the higher velocity examples, only the extension of the crater is slightly underestimated. In the last case ($v = 420$ m/s), although it is not evident from the damage state at $t = 0.25$ ms, perforation is predicted and the exit velocity is approximately 30 m/s.

Fig. 5.18 shows the damage profiles at $t = 0.25$ ms for all tests reported in the experimental paper [13]. In fig. 5.19, both the penetration depth and failure modes predictions for the elastoplastic impactor are summarized and compared with the experimental data and the modified NDRC formulas [181], which relate the impact velocity and plate thickness to the penetration depth (or perforation).

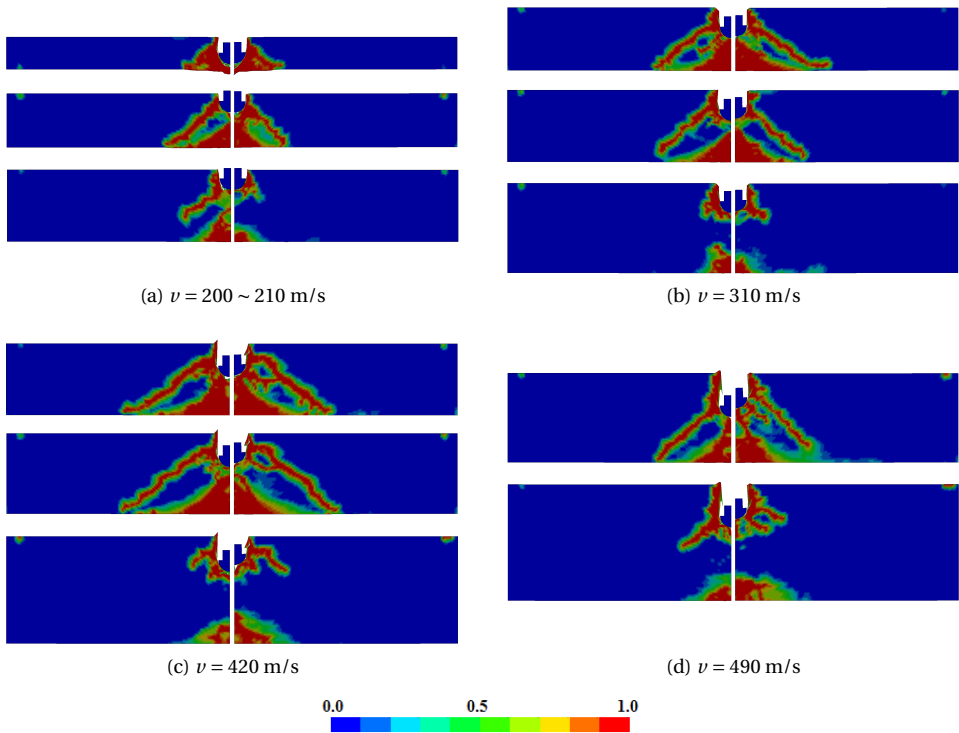


Figure 5.18: Slabs thickness effect. Damage profile at $t = 0.25$ ms considering different impact velocities ($v = 200 \sim 490$ m/s): (a) $h = 35, 60$ and 80 mm; (b) $h = 70, 80$ and 100 mm; (c) $h = 80, 90$ and 120 mm; (d) $h = 100$ and 130 mm.

In these plots, whenever the prediction of spalling at the back face is localized in a small area and does not expand with time, the failure mechanism is only classified as cratering. As it can be seen in fig. 5.19(a), the simulated failure mechanisms agree very

well with the experimental data. Only in case of the $h = 100$ mm thick plate impacted at $v = 490$ m/s a crater-spalling damage pattern is predicted while perforation was observed in the test. It is worth noting that, when a rigid impactor is considered, perforation is obtained.

In contrast to the good predictions of the failure modes, the model always overestimates the penetration depth (see fig. 5.19(b)). Besides the limitations of an underestimation of dilatation under pressure which leads to an underestimation of confinement (see fig. 9), also the use of numerical erosion is responsible for the increase of penetration depth. While in the model the damaged (crushed) material in front of the impactor is simply deleted, in reality this material flows around the impactor. This would cause an extra pressure in the surrounding material, which results in a local increase of confinement and consequently an increased resistance of the target.

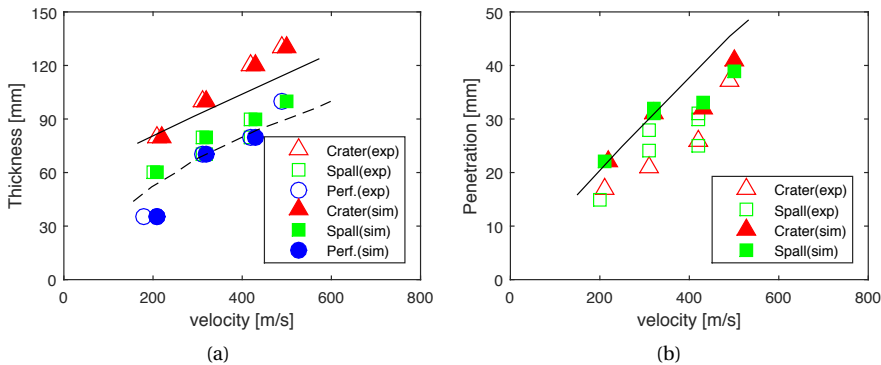


Figure 5.19: Comparison between experimental and numerical results for the elastoplastic impactor: (a) failure modes and (b) penetration depth. The solid and dashed lines are the limits, predicted by the modified NDRC formula [181], for crater-spalling and perforation, respectively. (The simulated velocities are off +10 m/s for better comparison.)

5.4.5 EFFECT OF ω_h ON FRACTURING PROCESS REPRESENTATION

Finally, as it was done in the single element triaxial study in sec. 5.3, the effect of the newly included damage mode (ω_h^*) to the global response of the model was evaluated. Fig. 5.20 shows the damage profile at two time steps for the same model as before, but ignoring the influence of ω_h on the deviatoric response of the material, i.e. ignoring the effective hydrostatic damage (ω_h^*) contribution in eq. 5.1 (cf. fig. 5.8 and the model 1 in fig. 5.11). As it can be seen, the failure mechanism is considerably different than reported before in fig. 5.16. In this case, since ω_h does not affect the global damage (ω), the material in front of the impactor, which is kept under high confinement levels, becomes stiffer and is hardly damaged. So, the material fails under shear. A cone is formed and pushed in front of the impactor cutting through the material with little resistance due to the relatively small compressive rate enhancement considered (see fig. 5.13).

These results (fig. 5.16) also show that the deformation of the impactor has a significant influence on the overall failure process. The high deformation of the elastoplastic projectile immediately after impact (see damage profiles at $t = 0.04$ ms), affects the way how the impact energy is transmitted to the target and reduces the magnitude of the peak pressure induced to the target. This leads to a smaller shear cone than in the rigid impactor case.

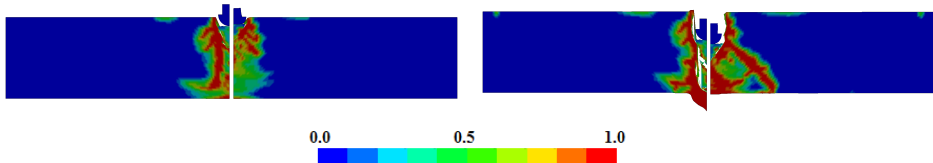


Figure 5.20: Damage profile at $t = 0.04$ ms (left) and $t = 0.20$ ms (right) in a $h = 90$ mm thick plate impacted at $v = 420$ m/s ignoring the contribution of ω_h to global damage (ω).

5

Fig. 5.21 shows the simulation results considering different damage (ω_h) growth rates with pressure obtained by changing power γ_ω in eq. 5.12 between 0.05 and 0.5. As it can be seen in fig. 5.22, this change has a minor impact on the volumetric response (EOS). But, it has major impact on the evolution of damage (see fig. 5.21). These results suggest that the amount of energy absorbed by ω_h dictates how and how much energy is transmitted to the structure, influencing the entire fracturing process. Furthermore, a closer look to the results of fig. 5.21(b) reveals that, when the target is tougher, the energy absorbed by the impactor due to deformation tends to increase, inducing less damage (compare left and right results on fig. 5.21(b)).

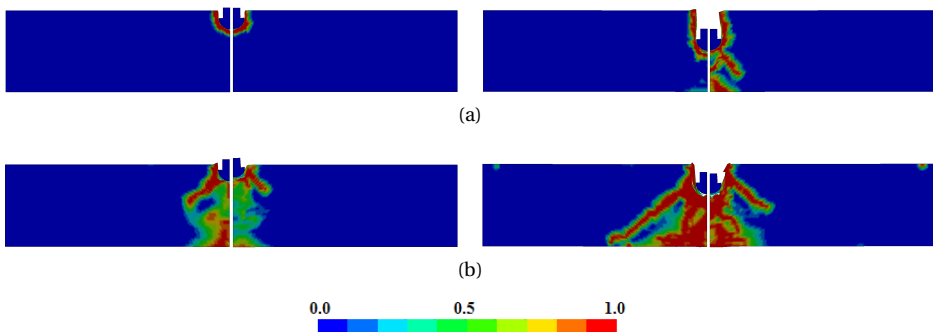


Figure 5.21: Damage profile at $t = 0.06$ ms (left) and $t = 0.20$ ms (right) in a $h = 90$ mm thick plate impacted at $v = 420$ m/s considering different evolutions of hydrostatic damage: (a) $\gamma_\omega = 0.05$ and (b) $\gamma_\omega = 0.50$.

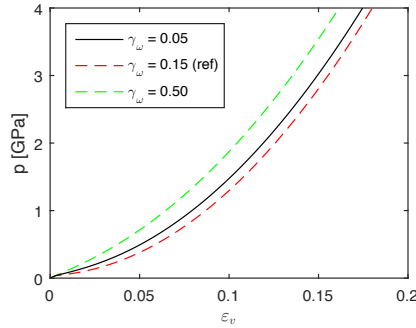


Figure 5.22: Volumetric response of the model considering different evolutions of hydrostatic damage (γ_ω) and a linear compaction ($\gamma_c = 1.0$).

5.5 CONCLUSIONS

In this contribution, a new isotropic damage model was used to investigate the dynamic response of concrete in ballistic impact situations. This formulation is an enhanced version of the *effective rate-dependent* nonlocal damage model proposed earlier by the authors. To the already considered tensile (ω_t) and compressive (ω_c) damage modes, a new hydrostatic damage mode (ω_h) was added to the formulation in order to take the damage (crushing) of the material matrix observed while porosity reduces during compaction into account. This new damage mode, together with a compaction criterion, governs the nonlinear volumetric response of the material (EOS) and contributes to the deterioration of the material stiffness when confinement is reduced.

Single element analyses of triaxial and hydrostatic tests, revealed that the description of the nonlinear volumetric response of concrete by an EOS as a plasticity phenomena disconnected from the deviatoric damage (or plastic-damage) formulation of the model, as it is commonly done in hydrodynamic constitutive modeling of concrete, is unrealistic. Such formulations fail to represent the effect of the loss of cohesion observed during compaction on the deviatoric response of the material. Although the deviatoric and hydrostatic parts of the model are treated separately in the proposed formulation, their interdependence is taken into account. This leads to a very realistic description of the triaxial and hydrostatic response of concrete.

In the second part of the paper, a set of impact test were used to evaluate how the added damage mode (ω_h) influences the model performance under ballistic impact situations. The proposed model can systematically predict the most significant failure modes (cratering, tunneling, spalling and radial cracking) observed during an impact on a concrete plate as a function of the projectile velocity and the plate thickness. It was demonstrated that it is not possible to correctly capture the different failure modes observed in the experiments without considering the effect of ω_h on the deviatoric response of the model. Furthermore, the rate at which ω_h grows with pressure has a significant impact on how and how much energy is absorbed in front of the impactor in the early stages of loading and, therefore controls the beginning and development of

the subsequent failure modes, namely spalling and radial cracking.

6

CONCLUSIONS

6.1 CONCLUSIONS

A new stress-based nonlocal (SBNL) *effective rate-dependent* damage model for concrete was proposed in this thesis. The isotropic damage formulation combines the effect of three damage modes, which were individually developed to describe the fundamental dynamic failure mechanisms of concrete: (i) tensile (mode I) failure, (ii) compressive-shear (mode II and mixed-mode) failure, and (iii) hydrostatic damage (crushing) of the cement matrix under compression. The update of the constitutive relations to describe the dynamic increase of strength and fracture energy in tension and compression is made a function of an *effective rate*, instead of the commonly used *instantaneous* strain rate. With this new concept, a *time* scale is introduced in the constitutive law which restrains the ‘evolution of strain-rate’, to properly represent the inherent dynamic properties of concrete. Mesh sensitivity is overcome with an enhanced version of the stress-based nonlocal regularization scheme, characterized by a variable *material length* which expands and contracts as a function of the stress state of neighboring elements. The proposed model was developed solely in the effective strain space, following an entirely explicit computation formulation. The model was implemented in LS-Dyna and successfully used to simulate different dynamic experiments with concrete, namely the modified split Hopkinson bar (spalling) tests, using both notched and un-notched specimens, dynamic compact tension tests and ballistic impact tests.

6

It was demonstrated that common phenomenological models which consider the Dynamic Increase Factor (DIF) depending on an assumed constant strain-rate history are not adequate to describe the dynamic behavior of concrete. From a macroscopic view point, the dynamic response of concrete is characterized by an apparent resistance to straining associated with a natural viscous behavior of the bulk material and by a dynamically delayed evolution of damage associated with the retarded crack opening process due to the *Stefan effect* and/or micro-inertia effects at the crack tip. So, the constitutive laws must include a *time* scale or viscosity to describe inherent dynamic properties of the material.

It was observed that the additional *time* scale in the constitutive relation, through an *effective rate*, has a weak regularization effect and acts as a localization limiter. However, mesh objectivity is only attained with the addition of a *material length* scale, here accomplished by an explicit stress-based nonlocal regularization scheme. This formulation uses a variable interaction domain defined as a function of the stress state of neighboring elements. A contraction of the internal length is induced in the direction of the smaller principal stresses, which leads to a desirable localization of the damage profiles and corrects the spurious dispersion of damage observed in standard nonlocal formulations.

The proposed nonlocal formulation provides an objective and realistic representations of crack initiation, propagation and branching. It effectively solves the problems with damage initiation and growth near discontinuities like free boundaries and notches. For example, in the modified split Hopkinson bar test with a notched specimen, damage initiation is properly predicted from the notch tip inwards, without any spurious damage spreading. It was also observed that, in the case of propagating cracks, the continuous deformation of the interaction domains induced by dynamic

evolution of the principal stresses at the 'crack' tip, leads to a realistic representations of crack dynamics. It captures the broadening of the fracture process zone observed during branching and promotes the rotation of cracks when the crack tip is hit by non-symmetric interfering stress waves reflected at the specimen boundaries.

Based on single-edge notch test results, it was concluded that branching does not occur at a specific material dependent crack velocity. The presented results suggest that, under dynamic tensile loading conditions, the evolution and bifurcation of cracks are material dependent phenomena influenced by both the load history and the geometry of the problem (boundary conditions). It was demonstrated that the evolution of the crack path and velocity are governed by the change of the principal stresses at the crack tip, which is controlled by the evolution of damage. With increasing crack speeds, the principal stresses at the crack tip tend to evolve from a mode-I to a mixed-mode state. Beyond a certain crack speed, the stress distribution around the crack tip reaches a critical state which favors damage development away from (parallel to) the forward cracking direction, and a single crack is no longer stable. When this condition is met, crack branching occurs whenever the stress field at the crack tip is destabilized by either a physical discontinuity or an interfering stress wave reflected at the specimen boundaries.

Finally, it was discussed and demonstrated that the description of the nonlinear volumetric response of concrete by an EOS as a plasticity phenomenon, as it is commonly done in hydrodynamic constitutive modeling, is unrealistic. Such formulations fail to represent the effect of the loss of cohesion observed during compaction on the deviatoric response of the material. This effect is taken into account in this study by the added hydrostatic damage which, besides controlling the evolution of the nonlinear volumetric response of the material, contributes to the deterioration of the material stiffness upon confinement. The contribution of hydrostatic damage to the deterioration of the material stiffness is controlled by a stress variable, which varies between zero, when confinement is maximum, and one, when confinement disappears. Although the deviatoric and hydrostatic parts of the model are treated separately in the proposed formulation, by taking their interdependency into account, it is possible to realistically simulate the triaxial and hydrostatic response of concrete.

The proposed computational model proved to be mesh objective and realistically simulates the fundamental damage mechanisms observed in ballistic impact situations, such as cratering, tunneling, spalling and radial cracking. It can systematically predict the different progressive failure modes (cratering, cratering and spalling or perforation) observed during impact on a concrete plate as a function of the projectile velocity and the plate thickness. It was demonstrated that it is not possible to correctly capture the different failure mechanisms observed in the experiments without considering the effect of the hydrostatic damage on the deviatoric response of the model. Furthermore, the rate at which the hydrostatic damage grows with pressure has a significant impact on how and how much energy is absorbed in front of the impactor in the early stages of loading and, therefore, controls the beginning and development of the subsequent failure modes, namely spalling and radial cracking. Based on the results presented in this thesis, it is concluded that a phenomenological computational model to simulate the failure of concrete in transient loading conditions should have three

fundamental properties: (i) a variable *material length* scale, (ii) a *time* scale and (iii) describe the loss of cohesion of the material under compression.

It is worth noting that the dynamic increase factors (DIF) considered in this study, both in tension and compression, are always smaller than the ones proposed by CEB/fib. So, caution is advised when using such recommendations for structural design because, for a given load, it over-predicts the true material response, which can lead to unsafe predictions of the real load-carrying capacity of structures.

6.2 SUGGESTIONS FOR FUTURE RESEARCH

Despite the promising results presented in this thesis, the proposed model was developed as an advanced tool to test new concepts. Before it can be used for engineering purposes, extensive validation for a wider range of dynamic loading conditions and more complex geometries is needed. Nevertheless, this research opens some questions about the failure mechanisms of concrete under impulsive loading and the numerical techniques used to model these, which motivates further experimental and numerical research. A list of recommendations for future research is presented in the following:

- The results in this thesis support the idea that the characteristic length (l_r) is not a fixed material property. It is suggested that, for mode I and mixed mode cracking, l_r expands due to stress concentration at the crack tip. When a crack expands (i.e. damage starts to grow), the material around it relaxes and l_r contracts. It is assumed that this expansion and contraction of l_r follows the activation and deactivation of the micro-cracks prior, during and after the development of the visible macro-crack. Since fracture in concrete is a highly rate dependent phenomenon, it is important to evaluate if and how l_r changes in dynamics and how it relates to experimentally observed crack distributions. Furthermore, it is important to evaluate how l_r changes when the dominant stress state evolves from tension to compression. In order to answer these and other questions related to the material length scale, multi-scale analyses and specially designed experimental research are recommended.
- The *time* scale (λ) introduced in this model is meant to accommodate different mechanisms that contribute to the dynamic viscous-like response of the material, such as: the *Stefan effect* due to water contained in the micro-pores, micro-inertia effects at the crack tip, delayed relaxation of the material around cracks, etc. It is important to understand how these mechanisms are affected by rate and their actual contribution to the global dynamic response of the material at the different rate levels and stress state conditions (tension, compression and 'compaction'). Only then it will be possible to develop better phenomenological laws to describe the dynamic behavior of concrete. Detailed multi-scale analyses, considering the different phases of the micro-structure of concrete (aggregates, cement past, interfacial transition zones, voids and water), are recommended to address this issue.
- Experimental data show that, both the evolution of volumetric damage and the

nonlinear volumetric deformation of concrete (i.e. the EOS) are pressure and volumetric strain rate dependent. With increasing impact velocity, harder constituents of the concrete mixture (e.g. aggregates) are crushed in front of the impactor and the fragments decrease in size. Furthermore, it has been observed that in extreme situations, such as intense contact detonations, the material at the impacted face may change phase. Although all these phenomena are temperature dependent, it is not clear if and how temperature influences the failure behavior of concrete during impact. Since it is basically impossible to track all these changes real-time in experiments, full thermo-mechanical (multi-scale and multi-physics) numerical analyses are needed to shed some light on the problem.

- Although numerical erosion is an essential tool in impact dynamics, the definition of the criteria that trigger the removal of elements from the simulation is always problem dependent. In some cases, a small change in the erosion criterion can have a considerable influence on the simulation outcome. It is important to develop new 'erosion' techniques with criteria that are not case sensitive and lead to mesh independent results.
- The aim of this thesis was limited to local failure of concrete during ballistic impact. In order to be able to simulate the complete structural response one needs to consider the effects of structural oscillations at moderate strain rates, which becomes the leading loading condition and the main cause for mechanical degradation in a later stage. Under these dynamic cyclic loading conditions, the partial recovery of strength due to crack closure effects is usually considered essential for a realistic representation of the behavior of concrete. However, it is not clear yet how the pre-damaged material behaves in a dynamic reloading situation. Consequently, in each loading cycle, the material has a different stress-strain relation, equation of state and rate dependency behavior, which needs to be understood.
- Efficiency of the finite element computations can be improved by adaptive time-stepping methods and by applying nonlocal computations only in relevant damage areas (e.g. by using domain decomposition techniques).

ACKNOWLEDGEMENTS

Sintra, 18th of October 2017

After years of intensive and dedicated work, it is a wonderful feeling to finally write these words. At the end of this unforgettable journey, I would like to thank everyone who directly or indirectly made this thesis possible.

First and foremost I would like to express my deepest gratitude to my supervisors (and friends), Prof. dr. ir. L.J. (Bert) Sluys and Dr. ir. J. Weerheijm, for their encouragement, guidance and fruitful discussions. I will always remember our meetings... Despite my natural tendency to complicate things, somehow you always managed to give sense to my ideas and push me back on the right track. Your complementary knowledge on the computational and the physical aspects of the problem at hand was the foundation of my success. Thank you.

This thesis would not have been possible without the support and inspiration of friends and family. My deepest appreciation goes to Luís Vilares, Bruno and Tânia, Bert and Jaap, Rafid Al-Khoury, João Caetano, Jure and Patricia, Noori Bni Lam, Mehdi, Marcello, Frans van der Meer, João Barbosa, Tiziano, Tiago Pereira, Luís Guerreiro, Jorge Alfaiate and, last but not least, Andreia and my family. I will forever be grateful to all these wonderful individuals that have always been there with a smile and kind words of support in moments of need, making me move forward. Thank you for your unconditional friendship.

I would like to show my gratitude to all my colleagues at TU Delft and the Portuguese Air Force Academy for their friendship, support and interesting discussions over the years. They have been an inspiration for me to grow both personally and professionally.

This entire project would have not been possible without the permission of the Portuguese Air Force and the financial support given by the Portuguese *Fundação para a Ciência e Tecnologia* with the grant SFRH/BD/79451/2011. Their contribution is gratefully acknowledged.

I owe my deepest gratitude to the Portuguese Air Force Academy commanders, General Serôdio Fernandes, General Joaquim Borrego and General Rafael Martins, for the opportunity to pursue my calling as a researcher. I would like to thank the Air Force Infrastructure Directors, General Camisa and General Veloso, for their support and vote of confidence in me. A warm appreciation to all my direct commanders for their unconditional support, guidance and wise motivational words, namely: Colonel Saúde, Colonel Santiago, Colonel Oliveira, Colonel Mateus, Colonel Bispo dos Santos, Lieutenant Colonel Vasconcelos and Major Rute Ramalho. Finally, I will be always be indebted to Colonel Costa and Lieutenant Colonel Madruga Matos because they encouraged me to pursue my dreams.

And, I did it...

Luís Pereira

BIBLIOGRAPHY

- [1] Y Hao and H Hao. Influence of the concrete DIF model on the numerical predictions of RC wall responses to blast loadings. *Engineering Structures*, 73:24–38, 2014.
- [2] Defense Special Weapons Agency (DSWA). Design and analysis of hardened structures to conventional weapon effects (UFC 3-340-01), 2002.
- [3] T Krauthammer. *Modern protective structures*. CRC Press, Boca Raton, FL, 2008.
- [4] *EN 1992-1:2004 (E): Design of concrete structures*. 2004.
- [5] P Forquin. Brittle materials at high-loading rates: an open area of research. *Philosophical Transactions of the Royal Society A*, 375(2085):1–12, dec 2017.
- [6] K Kirane, Y Su, and Z Bazant. Strain-rate-dependent microplane model for high-rate comminution of concrete under impact based on kinetic energy release theory. *Proceedings of the Royal Society of London A: Mathematical, Physical and Engineering Sciences*, 471(2182), 2015.
- [7] D Shockey, A Marchand, S Skaggs, G Cort, M Burkett, and R Parker. Failure phenomenology of confined ceramic targets and impacting rods. *International Journal of Impact Engineering*, 9(3):263–275, 1990.
- [8] J Mazars, F Dufour, C Giry, A Rouquand, and C Pontiroli. Concrete under various loadings, way to model in a same framework: damage, fracture and compaction. In N Bicanic, R de Borst, H Mang, and G Meschke, editors, *Computational Modelling of Concrete Structures*, pages 45–58. Autria, 2010.
- [9] P Forquin, A Arias, and R Zaera. Role of porosity in controlling the mechanical and impact behaviours of cement-based materials. *International Journal of Impact Engineering*, 35(3):133–146, 2008.
- [10] R Woodward, B Baxter, S Pattie, and P Mccarthy. Impact fragmentation of brittle materials. *Journal de Physique IV*, IV(C3):259 – 264, 1991.
- [11] J Weerheijm. *Understanding the tensile properties of concrete*. Woodhead Publishing Limited, 2013.
- [12] Q Li, S Reid, H Wen, and A Telford. Local impact effects of hard missiles on concrete targets. *International Journal of Impact Engineering*, 32:224–284, 2005.
- [13] M Beppu, K Miwa, M Itoh, M Katayama, and T Ohno. Damage evaluation of concrete plates by high-velocity impact. *International Journal of Impact Engineering*, 35(12):1419–1426, 2008.

- [14] J Mazars. A description of micro and macroscale damage of concrete structure. *Engineering Fracture Mechanics*, 25(5/6):729–737, 1986.
- [15] J Crawford, Y Wu, J Magallanes, and S Lan. Modeling of concrete materials under extreme loads. *Advances in protective structures research*, 1:1, 2012.
- [16] CEB. *CEB–FIB Model Code 1990. Design Code*. Thomas Telford Services Ltd., Lausanne, Switzerland, 1993.
- [17] T Holmquist, G Johnson, and W Cook. A computational constitutive model for concrete subjected to large strains, high strain rates, and high pressures. In *14th International Symposium on Ballistic*, pages 1–10, Quebec City, Canada, 1993.
- [18] L Malvar, J Crawford, J Wesevich, and D Simons. A plasticity concrete material model for DYNA3D. *international Journal for Impact Engineereng*, 19(9-10):847–873, 1997.
- [19] W Riedel, K Thoma, S Hiermaier, and E Schmolinske. Penetration of reinforced concrete by BETA-B-500. Numerical analysis using a new macroscopic concrete model for hydrocodes. In *9th International Symposium on the Interaction of the effects of munitions with structures (ISIEMS-9)*, Berlin-Strausberg, Germany, 1999.
- [20] L Schwer and Y Murray. Continuous surface cap model for geomaterial modeling: A new LS-DYNA material type. In *7th International LSDYNA Users Conference*, pages 35–50, 2002.
- [21] Y Murray. Theory and evaluation of concrete Material Model 159. In *8th International LS-DYNA users conference*, pages 6.25–6.36, Dearborn, Michigan, USA, 2004.
- [22] A Fossum and R Brannon. On a viscoplastic model for rocks with mechanism-dependent characteristic times. *Acta Geotechnica*, 1(2):89–106, jul 2006.
- [23] J Magallanes and Y Wu. Recent improvements to release III of the K&C concrete model. In *11th International LS-DYNA Users Conference*, pages 37–48, 2010.
- [24] J Mazars and G Pijaudier-Cabot. Continuum damage theory - application to concrete. *Journal of Engineering Mechanics*, 115(2):345–365, 1989.
- [25] J Dube, G Pijaudier-cabot, and C Borderie. Rate dependent damage model for concrete in dynamics. *ASCE Journal of Engineering Mechanics*, 122(10):939–947, 1996.
- [26] C Comi and U Perego. Fracture energy based bi-dissipative damage model for concrete. *International Journal of Solids and Structures*, 38:6427–6454, 2001.
- [27] M Jirasek. Nonlocal damage mechanics with application to concrete. *Revue Française de Génie Civil*, 8(5-6):683–707, 2004.
- [28] R Faria, J Oliver, and M Cervera. Modeling material failure in concrete structures under cyclic actions. *Journal of Structural Engineering*, 130(12):1997–2005, 2004.

- [29] F Gatuingt, R Desmorat, M Chambart, D Combescure, and D Guilbaud. Anisotropic 3D delay-damage model to simulate concrete structures. *European Journal of Computational Mechanics*, 17(5-7):749–760, oct 2008.
- [30] C Giry, C Oliver-Leblond, F Dufour, and F Ragueneau. Cracking analysis of reinforced concrete structures. *European Journal of Environmental and Civil Engineering*, 18(7):1–14, jan 2014.
- [31] J Mazars, F Hamon, and S Grange. A model to forecast the response of concrete under severe loadings the μ damage model. *Procedia Materials Science*, 3:979–984, 2014.
- [32] C Wolff, N Richart, and J Molinari. A non-local continuum damage approach to model dynamic crack branching. *International Journal for Numerical Methods in Engineering*, 101:933–949, 2015.
- [33] L Pereira, J Weerheijm, and L Sluys. A new rate-dependent stress-based nonlocal damage model to simulate dynamic tensile failure of quasi-brittle materials. *International Journal of Impact Engineering*, 94:83–95, 2016.
- [34] L Pereira, J Weerheijm, and L Sluys. A new effective rate dependent damage model for dynamic tensile failure of concrete. *Engineering Fracture Mechanics*, 176:281–299, 2017.
- [35] J Eibl and B Schmidt-Hurtienne. Strain-rate-sensitive constitutive law for concrete. *Journal of Engineering Mechanics*, 125(12):1411–1420, 1999.
- [36] J Lee and G Fenves. Plastic-damage model for cyclic loading of concrete structures. *Journal of Engineering Mechanics*, 124(8):892–900, aug 1998.
- [37] F Gatuingt and G Pijaudier-Cabot. Coupled damage and plasticity modelling in transient dynamic analysis of concrete. *International Journal for Numerical and Analytical Methods in Geomechanics*, 26(1):1–24, jan 2002.
- [38] N Gebbeken and S Greulich. A new material model for SFRC under high dynamic loadings. In *International Conference on Interaction of the Effects of Munitions with Structure (ISIEMS-2003)*, pages 1–16, Mannheim, Germany, 2003.
- [39] P Grassl and M Jirasek. Plastic model with non-local damage applied to concrete. *International Journal for Numerical and Analytical Methods in Geomechanics*, 30(1):71–90, jan 2006.
- [40] L Jason, A Huerta, G Pijaudier-Cabot, and S Ghavamian. An elastic plastic damage formulation for concrete: Application to elementary tests and comparison with an isotropic damage model. *Computer Methods in Applied Mechanics and Engineering*, 195(52):7077–7092, nov 2006.
- [41] R Pedersen, A Simone, and L Sluys. An analysis of dynamic fracture in concrete with a continuum visco-elastic visco-plastic damage model. *Engineering Fracture Mechanics*, 75:3782–3805, 2008.

- [42] F Zheng, Z Wu, C Gu, T Bao, and J Hu. A plastic damage model for concrete structure cracks with two damage variables. *Science China - Technological Sciences*, 55(11):2971–2980, aug 2012.
- [43] P Grassl, D Xenos, U Nystrom, R Rempling, and K Gylltoft. CDPM2: A damage-plasticity approach to modelling the failure of concrete. *International Journal of Solids and Structures*, 50(24):3805–3816, 2013.
- [44] G Voyiadjis. Coupled viscoplastic damage model for hypervelocity impact induced damage in metals and composites. In *Materials under Extreme Loadings: Application to Penetration and Impact*. 2013.
- [45] U Haussler-Combe and E Panteki. Modeling of strain rate effects for concrete with viscoelasticity and retarded damage. *International Journal of Solids and Structures*, 90:153–166, 2016.
- [46] Z Bazant, Y Xiang, and P Prat. Microplane model for concrete. I: Stress-strain boundaries and finite strain. *Journal of Engineering Mechanics*, (3):245–254, 1996.
- [47] Z Bazant and F Caner. Impact comminution of solids due to local kinetic energy of high shear strain rate: I. Continuum theory and turbulence analogy. *Journal of the Mechanics and Physics of Solids*, 64(1):223–235, 2014.
- [48] J Hallquist. *LS-DYNA Theory manual*. Livermore Software Technology Corporation, Livermore, California, 2006.
- [49] C Giry, F Dufour, and J Mazars. Stress-based nonlocal damage model. *International Journal of Solids and Structures*, 48(25-26):3431–3443, dec 2011.
- [50] J Cesar de Sa, F Andrade, and F Pires. Theoretical and numerical issues on ductile failure prediction - an overview. *Computer Methods in Materials Science*, 10(4):279–293, 2010.
- [51] F Andrade, M Vogler, J Cesar de Sa, and F Pires. User-defined nonlocal models in LS-DYNA. In *8th European LS-Dyna Users Conference*, Strasbourg, 2011.
- [52] J Mazars, F Hamon, and S Grange. A new 3D damage model for concrete under monotonic, cyclic and dynamic loadings. *Materials and Structures*, 48(11):3779–3793, 2015.
- [53] T Gabet, Y Malecot, and L Daudeville. Triaxial behaviour of concrete under high stresses: Influence of the loading path on compaction and limit states. *Cement and Concrete Research*, 38(3):403–412, 2008.
- [54] J Simo and J Ju. Strain and stress-based continuum damage model - I. Formulation. *International Journal of Solids and Structures*, 1987.
- [55] N Ottosen. Constitutive model for short time loading of concrete. *Journal of Engineering Mechanics (ASCE)*, 105:127–141, 1979.

- [56] P Menetrey and K Willam. Triaxial failure criterion for concrete and its generalization. *ACI Structural Journal*, 92:311–318, 1995.
- [57] P Grassl and M Jirasek. Damage-plastic model for concrete failure. *International Journal of Solids and Structures*, 48(6):7166–7196, mar 2006.
- [58] G Cusatis. Strain-rate effects on concrete behavior. *International Journal of Impact Engineering*, 38(4):162–170, 2011.
- [59] N Moes, J Dolbow, and T Belytschko. A finite element method for crack growth without remeshing. *International Journal for Numerical Methods in Engineering*, 46:131–150, 1999.
- [60] G Wells and L Sluys. A new method for modelling cohesive cracks using finite elements. *International Journal for Numerical Methods in Engineering*, 50(12):2667–2682, 2001.
- [61] Z Bazant, M Jirasek, and P Baz. Nonlocal integral formulations of plasticity and damage: survey of progress. *Journal of Engineering Mechanics*, (11):1119–1149, 2002.
- [62] A Simone, H Askes, and L Sluys. Incorrect initiation and propagation of failure in non-local and gradient-enhanced media. *Int. Journal of Solids and Structures*, 41:351–363, 2004.
- [63] G Pijaudier-Cabot, K Haidar, and J Dube. Non-local damage model with evolving internal length. *International Journal for Numerical and Analytical Methods in Geomechanics*, 28:633–652, jun 2004.
- [64] A Krayani, G Pijaudier-Cabot, and F Dufour. Boundary effect on weight function in nonlocal damage model. *Engineering Fracture Mechanics*, 76(14):2217–2231, sep 2009.
- [65] G Pijaudier-Cabot and F Dufour. Non local damage model - Boundary and evolving boundary effects. *European Journal of Environmental and Civil Engineering*, 14(6-7):729–749, 2010.
- [66] R Desmorat and F Gatuingt. Introduction of an internal time in nonlocal integral theories. In *Computational Modelling of Concrete Structures*, pages 121–128. CRC Press, 2010.
- [67] G Nguyen. A damage model with evolving nonlocal interactions. *International Journal of Solids and Structures*, 48:1544–1559, may 2011.
- [68] D Gregoire, L Rojas-Solano, and G Pijaudier-Cabot. A new integration-based nonlocal model to predict damage and failure in quasi-brittle materials, 2011.
- [69] D Gregoire, L Rojas-Solano, and G Pijaudier-Cabot. Continuum to discontinuum transition during failure in non-local damage models. *International Journal for Multiscale Computational Engineering*, 10(6):567–580, 2012.

- [70] S Saroikhani, R Vafadari, and A Simone. A simplified implementation of a gradient-enhanced damage model with transient length scale effects. *Computational Mechanics*, 51:899–909, 2013.
- [71] I Vegt, K van Breugel, and J Weerheijm. Failure mechanisms of concrete under impact loading. In *7th International Conference on Fracture Mechanics of Concrete and Concrete Structures (FraMCoS-7)*, Catania, Italy, 2007. Taylor & Francis.
- [72] M Jirasek. Modeling of localized inelastic deformation (Lecture Notes), 2010.
- [73] G Pijaudier-Cabot and P Bazant. Nonlocal damage theory. *Journal of Engineering Mechanics*, 113(10):1512–1533, 1987.
- [74] R Peerlings, R de Borst, W Brekelmans, and J Vree. Gradient enhanced damage for quasi-brittle materials. *International Journal for Numerical Methods in Engineering*, 39:3391–3403, 1996.
- [75] V Tvergaard and A Needleman. Effects of nonlocal damage in porous plastic solids. *International Journal of Solids and Structures*, 32(8-9):1063–1077, 1995.
- [76] M Jirasek. Nonlocal damage mechanics. *Revue Européenne de Génie Civil*, 11(7-8):993–1021, aug 2007.
- [77] M Jirasek. Nonlocal models for damage and fracture: comparison of approaches. *International Journal of Solids and Structures*, 35(31):4133–4145, 1998.
- [78] C Pontiroli, A Rouquand, and E Canton. Shock wave loading on reinforced concrete plates - experimental results and comparison with explicit damage model prediction. In *Fracture Mechanics of Concrete Structures (FraMCoS-2)*, pages 1219–1228, 1995.
- [79] P Bischoff and H Perry. Compressive behaviour of concrete at high strain rates. *Materials and Structures*, 24:425–450, 1991.
- [80] L Malvar and A Ross. Review of strain rate effects for concrete in tension. *ACI Materials Journal*, 95:735–739, 1998.
- [81] D Abrams. Effect of rate of application of load on the compressive strength of concrete. In *20th annual meeting*, pages 364–377, West Conshohocken, PA, USA, 1917. ASTM.
- [82] K Ravi-Chandar and W Knauss. An experimental investigation into dynamic fracture: I. Crack initiation and arrest. *International Journal of Fracture*, 25:247–262, 1984.
- [83] M Curbach and J Eibl. Crack velocity in concrete. *Engineering Fracture Mechanics*, 35(1-3):321–326, 1990.
- [84] K Ravi-Chandar. Dynamic fracture of nominally brittle materials. *International Journal of Fracture*, 90:83–102, 1998.

- [85] A Plotzitza, T Rabczuk, and J Eibl. Techniques for numerical simulations of concrete slabs for demolishing by blasting. *Journal of engineering mechanics*, 133:523–533, 2007.
- [86] J Weerheijm. *Concrete under impact tensile loading and lateral compression*. PhD thesis, Delft Univ. of Technology, Delft, 1992.
- [87] P Bischoff and H Perry. Impact behavior of plain concrete loaded in uniaxial compression. *Journal of Engineering Mechanics*, 121(6):685–693, 1995.
- [88] P Rossi. A physical phenomenon which can explain the mechanical behaviour of concrete under high strain rates. *Materials and Structures*, 24:422–424, 1991.
- [89] A Ross, D Jerome, J Tedesco, and M Hughes. Moisture and strain rate effects on concrete strength (93-M33). *ACI Materials Journal*, 93:293–298, 1996.
- [90] J Zielinski. *Fracture of concrete and mortar under uniaxial impact tensile loading*. PhD thesis, Delft, The Netherlands., 1982.
- [91] I Vegt and J Weerheijm. Influence of moisture on the fracture behaviour of concrete loaded in dynamic tension. In V. Saouma, J. Bolander, and E. Landis, editors, *9th International Conference on Fracture Mechanics of Concrete and Concrete Structures (FraMCoC-9)*, 2016.
- [92] Q Li and H Meng. About the dynamic strength enhancement of concrete-like materials in a split Hopkinson pressure bar test. *International Journal of Solids and Structures*, 40:343–360, 2003.
- [93] X Zhou and H Hao. Modelling of compressive behaviour of concrete-like materials at high strain rate. *International Journal of Solids and Structures*, 45(17):4648–4661, 2008.
- [94] Q Li, Y Lu, and H Meng. Further investigation on the dynamic compressive strength enhancement of concrete-like materials based on split Hopkinson pressure bar tests. Part II: Numerical simulations. *International Journal of Impact Engineering*, 36(12):1335–1345, dec 2009.
- [95] M Zhang, H Wu, Q Li, and F Huang. Further investigation on the dynamic compressive strength enhancement of concrete-like materials based on split Hopkinson pressure bar tests. Part I: Experiments. *International Journal of Impact Engineering*, 36:1327–1334, dec 2009.
- [96] Y Lu and Q Li. About the dynamic uniaxial tensile strength of concrete-like materials. *International Journal of Impact Engineering*, 38(4):171–180, 2011.
- [97] U Haussler-Combe and T Kuhn. Modeling of strain rate effects for concrete with viscoelasticity and retarded damage. *International Journal of Impact Engineering*, 50:17–28, dec 2012.

- [98] L Snozzi, A Caballero, and J Molinari. Influence of the meso-structure in dynamic fracture simulation of concrete under tensile loading. *Cement and Concrete Research*, 41:1130–1142, 2011.
- [99] M Cervera, J Oliver, and O Manzoli. A rate-dependent isotropic damage model for the seismic analysis of concrete dams. *Earthquake Eng & Struct Dynamics*, 25:987–1010, 1996.
- [100] N Gebbeken and M Ruppert. A new material model for concrete in high-dynamic hydrocode simulations. *Applied Mechanics and Materials*, 70:463–478, 2000.
- [101] H Schuler, C Mayrhofer, and K Thoma. Spall experiments for the measurement of the tensile strength and fracture energy of concrete at high strain rates. *International Journal of Impact Engineering*, 32:1635–1650, 2006.
- [102] J Lemaitre and J Chaboche. *Mechanics of solid materials*. Cambridge University Press, 1990.
- [103] R Lorefice, G Etse, and I Carol. Viscoplastic approach for rate-dependent failure analysis of concrete joints and interfaces. *International Journal of Solids and Structures*, 45(9):2686–2705, may 2008.
- [104] A Brara, F Camborde, J Klepaczko, and C Mariotti. Experimental and numerical study of concrete at high strain rates in tension. *Mechanics of Materials*, 33:33–45, 2001.
- [105] R Desmorat, M Chambart, F Gatuingt, and D Guilbaud. Delay-active damage versus non-local enhancement for anisotropic damage dynamics computations with alternated loading. *Engineering Fracture Mechanics*, 77(12):2294–2315, aug 2010.
- [106] B Erzar and P Forquin. Experiments and mesoscopic modelling of dynamic testing of concrete. *Mechanics of Materials*, 43(9):505–527, sep 2011.
- [107] W Wang, L Sluys, and R de Borst. Interaction between material length scale and imperfection size for localisation phenomena in viscoplastic media. *European Journal of Mechanics, A/Solids*, 15(3):447–464, 1996.
- [108] M Meyers. *Dynamic behavior of materials*. John Wiley & Sons, Inc., 1994.
- [109] B Cox, H Gao, D Gross, and D Rittel. Modern topics and challenges in dynamic fracture. *Journal of the Mechanics and Physics of Solids*, 53(3):565–596, 2005.
- [110] E Bouchbinder, J Fineberg, and M Marder. Dynamics of Simple Cracks. *Annual Review of Condensed Matter Physics*, 1:371, 2010.
- [111] P Forquin. An optical correlation technique for characterizing the crack velocity in concrete. *European Physical Journal: Special Topics*, 206:89–95, 2012.

- [112] J Ozbolt, A Sharma, and H Reinhardt. Dynamic fracture of concrete – compact tension specimen. *International Journal of Solids and Structures*, 48:1534–1543, 2011.
- [113] J Ozbolt, J Bosnjak, and E Sola. Dynamic fracture of concrete compact tension specimen: Experimental and numerical study. *International Journal of Solids and Structures*, 50(25–26):4270–4278, 2013.
- [114] Q Zhang and J Zhao. A review of dynamic experimental techniques and mechanical behaviour of rock materials. *Rock Mechanics and Rock Engineering*, 47:1411–1478, 2014.
- [115] J Ozbolt, N Bede, A Sharma, and U Mayer. Dynamic fracture of concrete L-specimen: Experimental and numerical study. *Engineering Fracture Mechanics*, 148:27–41, 2015.
- [116] M Ramulu and A Kobayashi. Mechanics of crack curving and branching - a dynamic fracture analysis. *International Journal of Fracture*, 27:187–201, 1985.
- [117] X Zhang, R Yu, G Ruiz, M Tarifa, and M Camara. Effect of loading rate on crack velocities in HSC. *International Journal of Impact Engineering*, 37:359–370, 2010.
- [118] M Buehler and Z Xu. Materials science: Mind the helical crack. *Nature materials*, 464(4):42–43, 2010.
- [119] C Tang and Y Yang. Crack branching mechanism of rock-like quasi-brittle materials under dynamic stress. *Journal of Central South University*, 19:3273–3284, 2012.
- [120] E Bouchbinder, T Goldman, and J Fineberg. The dynamics of rapid fracture: instabilities, nonlinearities and length scales. *Reports on progress in physics*, 77(4):046501, 2014.
- [121] K Ravi-Chandar and B Yang. On the role of microcracks in the dynamic fracture of brittle materials. *Journal of the Mechanics and Physics of Solids*, 45(4):535–563, 1997.
- [122] K Ravi-Chandar. *Dynamic fracture*. Elsevier Science, London, 2004.
- [123] J Fineberg and M Marder. Instability in dynamic fracture. *Physics Reports*, 313:1–108, 1999.
- [124] K Ravi-Chandar and W Knauss. An experimental investigation into dynamic fracture: III. On steady-state crack propagation and crack branching. *International Journal of Fracture*, 26:141–154, 1984.
- [125] J Fineberg, E Sharon, and G Cohen. Crack front waves in dynamic fracture. *International Journal of Fracture*, 121(1-2):55–69, 2003.

- [126] F Abraham. How fast can cracks move? A research adventure in materials failure using millions of atoms and big computers. *Advances in Physics*, 52(8):727–790, 2003.
- [127] J Fineberg and E Bouchbinder. Recent developments in dynamic fracture: some perspectives. *International Journal of Fracture*, 196(1-2):33–57, 2015.
- [128] J Song, H Wang, and T Belytschko. A comparative study on finite element methods for dynamic fracture. *Computational Mechanics, Springer-Verlag*, 42:239–250, 2008.
- [129] F Bobaru and G Zhang. Why do cracks branch? A peridynamic investigation of dynamic brittle fracture. *International Journal of Fracture*, 196(1):59–98, 2015.
- [130] M Buehler and H Gao. Dynamical fracture instabilities due to local hyperelasticity at crack tips. *Nature*, 439(19):307–310, 2006.
- [131] S Zhou, P Lomdahl, R Thomson, and B Holian. Dynamic crack processes via molecular dynamics. *Physical Review Letters*, 76(13):2318–2321, 1996.
- [132] C Qin and C Zhang. Numerical study of dynamic behavior of concrete by meso-scale particle element modeling. *International Journal of Impact Engineering*, 38:1011–1021, 2011.
- [133] T Nguyen, J Yvonnet, Q Zhu, M Bornert, and C Chateau. A phase field method to simulate crack nucleation and propagation in strongly heterogeneous materials from direct imaging of their microstructure. *Engineering Fracture Mechanics*, 139:18–39, 2015.
- [134] A Pandolfi and M Ortiz. An eigenerosion approach to brittle fracture. *International Journal for Numerical Methods in Engineering*, 92:694–714, 2012.
- [135] X Xu and A Needleman. Numerical Simulations of Fast Crack-Growth in Brittle Solids. *Journal of the Mechanics and Physics of Solids*, 42(9):1397–&, 1994.
- [136] G Camacho and M Ortiz. Computational modelling of impact damage in brittle materials. *International Journal of Solids and Structures*, 33(20-22):2899–2938, 1996.
- [137] M Ortiz and A Pandolfi. Finite-deformation irreversible cohesive elements for three-dimensional crack-propagation analysis. *International Journal for Numerical Methods in Engineering*, 44:1267–1282, 1999.
- [138] T Belytschko and T Black. Elastic crack growth in finite elements with minimal remeshing. *International Journal for Numerical Methods in Engineering*, 45:601–620, 1999.
- [139] Z Bazant and B Oh. Crack band theory for fracture of concrete. *Materials and Structures*, 16:155–177, 1983.

- [140] J VonNeumann and R Richtmyer. A method for the numerical calculation of hydrodynamic shocks. *Journal of Applied Physics*, 21:232–237, 1950.
- [141] Z Bazant. Nonlocal damage theory based on micromechanics of crack interactions. *Journal of Engineering Mechanics*, 120(3):593–617, 1994.
- [142] C Miehe, M Hofacker, and F Welschinger. A phase field model for rate-independent crack propagation: Robust algorithmic implementation based on operator splits. *Computer Methods in Applied Mechanics and Engineering*, 199(45-48):2765–2778, 2010.
- [143] N Moes and C Stolz. A level set based model for damage growth: the thick level set approach. *International Journal for Numerical Methods in Engineering*, 86:358–380, 2011.
- [144] K Moreau, N Moes, D Picart, and L Stainier. Explicit dynamics with a non-local model using the thick level set approach. *International Journal for Numerical Methods in Engineering*, (102):808–838, 2015.
- [145] J Ozbolt and A Sharma. Numerical simulation of dynamic fracture of concrete through uniaxial tension and L-specimen. *Engineering Fracture Mechanics*, 85:88–102, 2012.
- [146] H Kupfer, H Hilsdorf, and H Rusch. Behavior of concrete under biaxial stresses. *Journal Proceedings*, 66(8):656–666, 1969.
- [147] *fib Model Code for Concrete Structures 2010*. Ernst & Sohn, 2013.
- [148] T Belytschko, H Chen, J Xu, and G Zi. Dynamic crack propagation based on loss of hyperbolicity and a new discontinuous enrichment. *International Journal for Numerical Methods in Engineering*, 58:1873–1905, 2003.
- [149] C Linder and F Armero. Finite elements with embedded branching. *Finite Elements in Analysis and Design*, 45(4):280–293, 2009.
- [150] Y Ha and F Bobaru. Studies of dynamic crack propagation and crack branching with peridynamics. *International Journal of Fracture*, 162(1-2):229–244, 2010.
- [151] M Borden, C Verhoosel, M Scott, T Hughes, and C Landis. A phase-field description of dynamic brittle fracture. *Computer Methods in Applied Mechanics and Engineering*, 217-220:77–95, 2012.
- [152] X Zhou, Y Wang, and Q Qian. Numerical simulation of crack curving and branching in brittle materials under dynamic loads using the extended non-ordinary state-based peridynamics. *European Journal of Mechanics, A/Solids*, 60:277–299, 2016.
- [153] A Kobayashi, B Wade, W Bradley, and S Chiu. Crack branching in Homalite-100 sheets. *Engineering Fracture Mechanics*, 6:81–92, 1974.

- [154] T Boue, G Cohen, and J Fineberg. Origin of the microbranching instability in rapid cracks. *Physical Review Letters*, 114(5):1–5, 2015.
- [155] F Bowden, J Brunton, J Field, and A Heyes. Controlled fracture of brittle solids and interruption of electrical current. *Nature*, 216:38–42, 1967.
- [156] A Livne, O Ben-David, and J Fineberg. Oscillations in rapid fracture. *Physical Review Letters*, 98(124301):1–4, 2007.
- [157] E Katzav, M Adda-Bedia, and R Arias. Theory of dynamic crack branching in brittle materials. *International Journal of Fracture*, 143(3):245–271, 2007.
- [158] G Block, M Rubin, J Morris, and J Berryman. Simulations of dynamic crack propagation in brittle materials using nodal cohesive forces and continuum damage mechanics in the distinct element code LDEC. *International Journal of Fracture*, 144(3):131–147, 2007.
- [159] Z Bazant and F Caner. Comminution of solids caused by kinetic energy of high shear strain rate, with implications for impact, shock, and shale fracturing. *Proceedings of the National Academy of Sciences of the United States of America*, 110(48):19291–4, 2013.
- [160] W Chen and G Ravichandran. An experimental technique for imposing dynamic multiaxial-compression with mechanical confinement. *Experimental Mechanics*, 36(2):155–158, 1996.
- [161] D Grote, S Park, and M Zhou. Dynamic behavior of concrete at high strain rates and pressures: I. experimental characterization. *International Journal of Impact Engineering*, 25(9):869–886, 2001.
- [162] Y Al-Salloum, T Almusallam, S Ibrahim, H Abbas, and S Alsayed. Rate dependent behavior and modeling of concrete based on SHPB experiments. *Cement and Concrete Composites*, 55:34–44, 2015.
- [163] E Flores-Johnson and Q Li. Effect of structurally-induced lateral confinement on split Hopkinson pressure bar test specimens of concrete-like materials. In *EPJ Web of Conferences*, volume 94, 2015.
- [164] P Forquin, G Gary, and F Gatuingt. A testing technique for concrete under confinement at high rates of strain. *International Journal of Impact Engineering*, 35(6):425–446, 2008.
- [165] X Vu, Y Malecot, L Daudeville, and E Buzaud. Experimental analysis of concrete behavior under high confinement: Effect of the saturation ratio. *International Journal of Solids and Structures*, 46:1105–1120, 2009.
- [166] C Poinard, Y Malecot, and L Daudeville. Damage of concrete in a very high stress state: experimental investigation. *Materials and Structures*, 43:15–29, jan 2010.

- [167] N Burlion, F Gatuingt, G Pijaudier-Cabot, and L Daudeville. Compaction and tensile damage in concrete: constitutive modelling and application to dynamics. *Computer Methods in Applied Mechanics and Engineering*, 183:291–308, 2000.
- [168] L Pereira, J Weerheijm, and L Sluys. A numerical study on crack branching in quasi-brittle materials with a new effective rate-dependent nonlocal damage model. *Engineering Fracture Mechanics*, 182:689–707, 2017.
- [169] D Drucker and W Prager. Soil mechanics and plastic analysis for limit design. *Quarterly of Applied Mathematics*, 10(2):157–165, 1952.
- [170] C Desai. *Mechanics of materials and interfaces: The disturbed state concept*. CRC press, 2000.
- [171] Y Hao, H Hao, G Jiang, and Y Zhou. Experimental confirmation of some factors influencing dynamic concrete compressive strengths in high-speed impact tests. *Cement and Concrete Research*, 52:63–70, 2013.
- [172] S Zhang, Y Lu, X Chen, X Teng, and S Yu. Further investigation on the real rate effect of dynamic tensile strength for concrete-like materials. *Latin American Journal of Solids and Structures*, 13:201–223, 2016.
- [173] T Gabet and X Vu. A new experimental technique for the analysis of concrete under high triaxial loading. *Journal de Physique IV France*, 134:635–640, 2006.
- [174] C Pontiroli, A Rouquand, and J Mazars. Predicting concrete behaviour from quasi-static loading to hypervelocity impact. An overview of the PRM model. *European Journal of Environmental and Civil engineering*, 14(6-7):703–727, aug 2010.
- [175] T Gabet. *Comportement triaxial du béton sous fortes contraintes*:. PhD thesis, Université Joseph-Fourier, Grenoble, 2006.
- [176] A Rouquand, C Pontiroli, and J Mazars. Concrete structures under severe loading: a strategy to model the response for a large range of dynamic loads. In *International Conference on Fracture Mechanics of Concrete and Concrete Structures (FraMCoS-6)*, Catania, Italy, 2007.
- [177] L Agardh and L Laine. 3D FE-simulation of high-velocity fragment perforation of reinforced concrete slabs. *International Journal of Impact Engineering*, 22(9):911–922, 1999.
- [178] N Trivedi and R Singh. Prediction of impact induced failure modes in reinforced concrete slabs through nonlinear transient dynamic finite element simulation. *Annals of Nuclear Energy*, 56:109–121, 2013.
- [179] T Hartmann, A Pietzsch, and N Gebbeken. A Hydrocode Material Model for Concrete. *International Journal of Protective Structures*, 1(4):443–468, dec 2010.
- [180] N Gebbeken, S Greulich, and A Pietzsch. Hugoniot properties for concrete determined by full-scale detonation experiments and flyer-plate-impact tests. *International Journal of Impact Engineering*, 32(12):2017–2031, 2006.

- [181] R Kennedy. A review of procedures for the analysis and design of concrete structures to resist missile impact effects. *Nuclear Engineering and Design*, 37:183–203, 1976.

CURRICULUM VITÆ

Luís Filipe MAGALHÃES PEREIRA

03-04-1979 Born in Vigo, Spain.

EDUCATION

2012–2017 PhD, Computational Mechanics
Delft University of Technology, Delft, The Netherlands

2011 Planning and Design of Airports
ANA Portugal, Lisbon, Portugal

2010 Commanding Officer Course
Portuguese Air Force Academy, Sintra, Portugal

2003–2008 MSc, Aerodrome Engineering (Civil Engineering)
Portuguese Air Force Academy, Sintra, Portugal

1998–2003 Frequency of Air Force Piloting course (incomplete degree)
Portuguese Air Force Academy, Sintra, Portugal

PROFESSIONAL EXPERIENCE

2009–2012 Lecturer, academic coordinator and students advisor
Portuguese Air Force Academy, Sintra, Portugal

2008–2009 Quality manager in a soils and pavements laboratory
Portuguese Air Force, Alverca, Portugal

2008–2009 Project assistant (in accumulation)
PROFICO, Lisbon, Portugal

LIST OF PUBLICATIONS

JOURNAL PAPERS

4. L Pereira, J Weerheijm, and L Sluys. Simulation of compaction and crushing of concrete in ballistic impact with a new damage model. *Int. J. Impact Eng.*, 111:208-221, 2018.
3. L Pereira, J Weerheijm, and L Sluys. A numerical study on crack branching in quasi-brittle materials with a new effective rate-dependent nonlocal damage model. *Int. J. Fracture*, 182:689-707, 2017.
2. L Pereira, J Weerheijm, and L Sluys. A new effective rate dependent damage model for dynamic tensile failure of concrete. *Int. J. Fracture*, 176:281-299, 2017.
1. L Pereira, J Weerheijm, and L Sluys. A new rate-dependent stress-based nonlocal damage model to simulate dynamic tensile failure of quasi-brittle materials. *Int. J. Impact Eng.*, 94:83-95, 2016.

CONFERENCES

8. L Pereira, J Weerheijm, and L Sluys. A new approach towards the numerical modelling of ballistic impact on concrete targets. *ISIEMS - 17*, 16-20 October 2017, Bad Neuenahr, Germany.
7. L Pereira, J Weerheijm, and L Sluys. A numerical study on crack branching in quasi-brittle materials. *CFRAC - 5*, 14-16 June 2017, Nantes, France.
6. L Pereira, J Weerheijm, and L Sluys. Simulation of dynamic behavior of quasi-brittle materials with new rate dependent damage model. *ECCOMAS - 7*, 5 - 10 June 2016 Crete Island, Greece.
5. L Pereira, J Weerheijm, and L Sluys. Simulation of dynamic behavior of quasi-brittle materials with new rate dependent damage model. *FraMCoS - 9*, 29 May - 1 June 2016 Berkeley, California USA.
4. L Pereira, J Weerheijm, and L Sluys. Simulation of dynamic tensile failure of quasi-brittle materials with a rate dependent, stress-enhanced nonlocal damage model, *CFRAC - 4*, 3-5 June 2015 Cachan (Paris), France.
3. L Pereira, J Weerheijm, and L Sluys. Modelling dynamic tensile failure of quasi-brittle materials using stress-enhanced nonlocal models. *DAPS - 5*, 19-21 May 2015, Singapore.
2. L Pereira, J Weerheijm, and L Sluys. Damage prediction in a concrete bar due to a compression and tension pulse - A comparison of the K&C, the CSCM and the RHT material models in LS-DYNA. *ISIEMS - 15*, 16-20 September 2013 Potsdam, Germany. (*Prized with the best conference paper and presentation for young researcher*)
1. L Pereira, J Weerheijm, and L Sluys. Dynamic response of concrete - LS-Dyna concrete material models review. *CFRAC - 3*, 5-7 June 2013 Prague, Czech Republic.